MECHANICAL AND ELECTRICAL PROPERTIES OF GRAPHENE SHEETS

A Dissertation

Presented to the Faculty of the Graduate School

of Cornell University

In Partial Fulfillment of the Requirements for the Degree of

Doctor of Philosophy

by

Joseph Scott Bunch

May 2008

MECHANICAL AND ELECTRICAL PROPERTIES OF GRAPHENE SHEETS

Joseph Scott Bunch, Ph. D.

Cornell University 2008

This thesis examines the electrical and mechanical properties of graphene sheets. We perform low temperature electrical transport measurements on gated, quasi-2D graphite quantum dots. In devices with low contact resistances, we use longitudinal and Hall resistances to extract a carrier density of 2-6 x 10^{11} holes per sheet and a mobility of 200-1900 cm^2/V-s. In devices with high resistance contacts, we observe Coulomb blockade phenomena and infer the charging energies and capacitive couplings. These experiments demonstrate that electrons in mesoscopic graphite pieces are delocalized over nearly the whole graphite piece down to low temperatures.

We also fabricate nanoelectromechanical systems (NEMS) from ultra thin graphite and graphene by mechanically exfoliating thin sheets over trenches in SiO_2. Vibrations with fundamental resonant frequencies in the MHz range are actuated either optically or electrically and detected optically by interferometry. We demonstrate room temperature charge sensitivities down to $2x10^{-3}$ $e/Hz^{½}$. The thinnest resonator consists of a single suspended layer of atoms and represents the ultimate limit of a two dimensional NEMS.

In addition to work on doubly clamped beams and cantilevers, we also investigate the properties of resonating drumheads, which consist of graphene sealed microchambers containing a small volume of trapped gas. These experiments allow us to probe the membrane properties of single atomic layers of graphene. We show that

these membranes are impermeable and can support pressure differences larger than one atmosphere. We use such pressure differences to tune the mechanical resonance frequency by ~100 MHz. This allows us to measure the mass and elastic constants of graphene membranes. We demonstrate that atomic layers of graphene have stiffness similar to bulk graphite ($E \sim 1$ TPa). These results show that single atomic sheets can be integrated with microfabricated structures to create a new class of atomic scale membrane-based devices.

BIOGRAPHICAL SKETCH

Joseph Scott Bunch was born on November 8, 1978 in Miami, Florida. He attended elementary, middle, and high school in Miami. After high school, he remained in Miami and enrolled at Florida International University (FIU) where he received his B.S. degree in physics in 2000. While at FIU, he was introduced to nanoscience research through an undergraduate research opportunity studying electrodeposition of metallic nanowires in Professor Nongjian Tao's lab. He also spent one summer in a research program at the University of Tennessee, Knoxville working with a scanning tunneling microscope in Professor Ward Plummer's lab. After graduation from FIU, Scott was awarded a graduate fellowship from Lucent Technologies, Bell Laboratories to continue his education. He spent the summer of 2000 at Bell Laboratories in Murray Hill, N.J. working with Nikolai Zhitenev on the electrodeposition of scanning single electron transistor tips. In August 2000, he enrolled in the physics department at Cornell University where he joined Paul McEuen's group and continued nanoscience research. His research focused primarily on the electrical and mechanical properties of graphene. After finishing his Ph.D. in May 2008, Scott will do postdoctoral research on mass sensing with nanoelectromechanical systems in Professor Harold Craighead and Professor Jeevak Parpia's lab at Cornell University before heading off to Colorado in August 2008 to become an Assistant Professor of Mechanical Engineering at the University of Colorado at Boulder.

To my family

ACKNOWLEDGMENTS

When I first arrived at Cornell University and joined Paul McEuen's lab, it was a lonely and empty place. Paul and his lab were still at Berkeley so the labs at Cornell were just empty rooms. I sat at my desk staring at freshly painted white walls and began to ponder whether I would survive the long years of a Ph.D. in such a dreary setting. Fortunately, things soon changed with the arrival of equipment and people that was to transform the corridors of Clark Hall to a lively and exciting place to work. It was truly been a pleasure working alongside a great group of scientists and people.

The most important influence on the successful completion of this thesis was my advisor, Paul McEuen. He has had greatest professional influence on my development as a scientist. He is an amazing scientist and mentor. He pushed me to develop my weaknesses and exploit my strengths. His courage to tackle new and difficult problems and his patience to withstand the many failures that accompany such risks is admirable. As a soon to be advisor to students, I only hope that some of his wisdom has rubbed off on me so that I may share it with my new graduate students.

One of the many remarkable things about Paul is his ability to attract and fill his lab with a wonderful group of people. I had the opportunity to work and learn from great postdocs. I worked with Alex Yanson during my first years and shared with him the displeasure of unsuccessfully trying to reproduce many of Hendrik Schon's phenomenal papers on molecular crystals with him. We later learned that these results were part of one of the largest cases of scientific fraud in recent scientific memory. Jiyong Park taught me how to use scanning probe microscopes. Though we never got around to finishing a paper based on this work, I still learned a great deal. Yuval Yaish worked closely with me for the work discussed in Chapter 4 of this thesis and taught

me how to make low temperature electrical measurements. The postdocs I didn't get to work with directly but from which I learned a lot are Jun Zhu, Ken Bosnick, Patrycja Paruch, Zhaohui Zhong, Yaquiong Xu, and Shahal Ilani. Besides being mentors these postdocs were also all good friends. Discussions with Shahal and Zhaouhui were especially helpful in shaping research ideas and proposals.

One of the wonderful aspects of doing a Ph. D. is going through it together with other graduate students. I was lucky enough to work with a phenomenal batch in Paul's lab. The original batch included those that followed Paul from Berkeley: Jiwoong Park, Ethan Minot, and Michael Woodside. This was quickly followed by the first Cornell batch: Markus Brink, Sami Rosenblatt, and Vera Sazonova. Later they were joined by Luke Donev, Lisa Larrimore, Xinjian "Joe" Zhou, Arend van der Zande, Nathan Gabor, Samantha Roberts, and Jonathan Alden . Life outside of the lab was memorable with this group: disagreeing about politics with Markus and Sami, acting in skits with Markus, Vera, Luke, Ethan, and Sami, and attempts to make a Hollywood blockbuster with Joe. I will miss you all.

For the work in this thesis, I must give special thanks to collaborators. Markus Brink helped me with the experiments in Chapter 4. He taught me everything I know about ebeam lithography. Kirill Bolotin helped me with the low temperature experiments in Chapter 4 and taught me everything I know about dilution fridges. Arend van der Zande was instrumental in our success with the suspended graphene resonators presented in Chapter 5 and 6. He was with me on both projects from the very early beginnings, helped fabricate many of the devices we used, his analytical abilities helped us solve problems we encountered, and I find myself always wanting to discuss nanomechanics with him whenever a new problem comes to mind. I am also indebted to him for taking over the editing of the first paper while I was in Korea meeting my future in laws and for his impressive cartoon image of suspended

graphene that helped popularize our work. I must also thank Ian Frank and Professor David Tanenbaum for help during the summer of 2006 when most of the work of Chapter 5 was completed. Ian Frank fabricated our first single layer suspended graphene membrane. The work in Chapter 6 couldn't have been done without the help of Jonathan Alden. After spending only a very short time in Paul's lab he joined onto the graphene membrane project and made several critical contributions. Most importantly, he fabricated the first single atomic layer sealed membrane. He was also responsible for much of the theory behind that paper. His attention to detail and MatLab ability far exceed mine, and it was privilege to have the opportunity to work with him.

I want to thank Arend and Jonathan for reading my whole thesis and giving me a lot of valuable criticisms and suggestions. I couldn't incorporate all of their suggestions, so do not fault them if you find parts of this thesis disagreeable or in need of revision.

A crucial part of the success of many of the experiments in this thesis was the result of a fruitful collaboration with Harold Craighead and Jeevak Parpia's lab. This began when I headed over to the other side of Clark Hall, and Arend introduced me to Scott Verbridge. I asked him if we can load are recently fabricated suspended graphene devices into his NEMS Actuation/Detection setup and see if they resonated. He agreed and within a few minutes we had our first vibrating graphene resonators. I am thankful to the continued support of Professor Harold Craighead and Professor Jeevak Parpia. They were always supportive of all my NEMS endeavors, and I am excited to be joining their lab soon to spend 3 months as a postdoc and continue my NEMS education from these two masters. The data presented in Chapter 5 and 6 of this thesis resulted from our collaboration.

Professor Jiwoong Park and his graduate student Lihong Herman helped us

calibrate the spring constant of AFM tips for experiments presented in Chapter 6. I would like to thank my committee members, Veit Elser and Rob Thorne, for sitting through 3 exams with me and reading this thesis. I would also like to thank the great support staff at Cornell and the secretaries that take care of the paperwork and negotiate the grand bureaucracies of the academic world, Douglas Milton, Judy Wilson, Deb Hatfield, Kacey Bray, Larissa Vygran, and Debbie Sladdich. I'd also like to thank Stan Carpenter and the guys in the professional machine shop. I also want to thank Christopher "Kit" Umbach for all his help with Raman spectroscopy and Victor Yu-Juei Tzen for the cartoon image of the graphene membrane in Chapter 6.

I would like to thank my friends, especially the members of the F. B. I. – you know who you all are and so as not to incriminate too many people, I will leave you all nameless. I would like to thank my good friend and roommate for 5 years Sahak Petrosyan. Together we shared many wonderful memories and his friendship is something I will cherish a lifetime. I also want to thank Saswat Sarangi and Faisal Ahmad who were great friends and neighbors. I can write a whole other 100 page thesis which chronicles the adventures we had in Ithaca, from overnight attempts to reach Miami to far crazier adventures that are better left untold, at least until names can be changed to protect the innocent. The friendships I made while at Cornell I will cherish a lifetime.

I want to thank my family who I owe so much and to whom I dedicate this thesis. My brother and sister shaped my life while growing up and as we go through life they continue to be in my thoughts. I want to thank my parents. It is their love and support through the years that brought me to Cornell and their love for their family and each other continues to inspire me to this day.

The greatest thing about my time in Ithaca was meeting my wife, Heeyoun. I am blessed to have met her and consider her to be my greatest discovery while at

Cornell. She is a great source of inspiration to me, and I love her deeply. Finally, I would like to thank the newest addition to my family, my daughter, Daniella. I tried to complete this thesis before she was born, but she seemed more motivated than I was and beat me to it by coming 12 days before her due date.

The words and ideas that follow represent only a small share of everything that happened while completing this thesis. There were many failures mixed in with the occasional success. It is the success that you read in these pages, but it is the undocumented failures and minor successes that also make up this thesis. It is because of the group of people described above, that all of this was possible. During my time at Cornell, I made scientific and personal discoveries, published papers, performed in plays, made movies, traveled, developed lifelong friendships, got married, and became a father. There is a running joke with my friends that life can only go downhill from here. As I sit down to finish writing these acknowledgements in the hospital room where my one day old daughter, Daniella, and wife, Heeyoun, are lying next to each other sleeping, I am reminded that the completion of this thesis represents the closing of one memorable phase of my life, but a new and more rewarding phase awaits.

TABLE OF CONTENTS

LIST OF FIGURES

LIST OF TABLES

CHAPTER 1

INTRODUCTION

1.1 Introduction

The discovery of a new material brings with it some of the most exciting and fruitful periods of scientific and technological research. With a new material come new opportunities to reexamine old problems as well as pose new ones. The recent discovery of graphene- atomically thin layers of graphite- brought such a period (Novoselov, Geim et al. 2004). For the first time, it is possible to isolate single two-dimensional atomic layers of atoms. These are among the thinnest objects imaginable. The strongest bond in nature, the C-C bond covalently locks these atoms in place giving them remarkable mechanical properties (Bunch, van der Zande et al. 2007; Meyer, Geim et al. 2007; Bunch, Verbridge et al. 2008). A suspended single layer of graphene is one of the stiffest known materials characterized by a remarkably high Young's modulus of ~ 1 TPa. As an electronic material, graphene represents a new playground for electrons in 2, 1, and 0 dimensions where the rules are changed due to its linear band structure. Scattering is low in this material allowing for the observation of the Quantum Hall Effect (QHE), and the unique band structure of graphene gives this old effect a new twist (Novoselov, Geim et al. 2005; Zhang, Tan et al. 2005). Graphene research is still in its infancy and this thesis examines only the very beginnings of what will likely be an important material of the future.

1.2 Outline

This thesis presents some of the first experiments on the electrical and mechanical properties of graphene. Chapters 1-3 include an overview of the basic concepts relevant to the experimental results presented in Chapters 4-6. The

experimental section begins in Chapter 4 where we perform low temperature electrical transport measurements on gated, few-layer graphene quantum dots. We find that electrons in mesoscopic graphite pieces are delocalized over nearly the whole graphite piece down to low temperatures. A modified form of this chapter is published in *Nano Letters* **5**, 287 (2005). An experimental study of the mechanical properties of suspended graphene begins in Chapter 5 where we study doubly clamped beams and cantilevers fabricated from graphene sheets. We fabricate the world's thinnest mechanical resonator from a suspended single layer of atoms. A version of this chapter is published in *Science* **315**, 490 (2007). Chapter 6 extends this work on mechanical resonators from graphene sheets to graphene membranes which are clamped on all sides and seal a small volume of gas in a microchamber. In this work we demonstrate that a graphene membrane is impermeable to gases down to the ultimate limit in thickness of only one atomic layer. A version of this chapter has been submitted.

1.3 Electrical Properties of Materials

Physicists love forces. Forces are one of the basic means by which they characterize materials. When presented with a new material they immediately want to know two things: how the electrons in the material respond to electrical forces and how the atoms respond to mechanical forces. The first of these is summed up by Ohm's Law:

$$V = IR \tag{1.1}$$

where V is the voltage difference across the conductor, I is the current, and R is the resistance. A useful way to express this resistance is in terms of a resistivity ρ defined as:

$$R = \frac{\rho L}{A} \tag{1.2}$$

where L is the length of the material and A is the cross sectional area through which the current is flowing. The resistivity is of a material is independent of its geometry making it a useful quantity to compare different materials.

Ohm's law is a general formula applicable to 3D, 2D, and 1D conductors. In a typical conductor charges are moving and scattering at random with no net movement of charge across the sample. This situation changes when a voltage difference, V, is applied across the conductor. The voltage difference creates an electric field, E, which gives these randomly scattered electrons a net force in one direction. Some of the possible scattering mechanisms are phonons in the material, defects in the lattice, or charge inhomogeneities in the material. The velocity with which the charges move in the direction of the applied field is known as the drift velocity, v_d and is related to the current density J by:

$$J = nev_d \tag{1.3}$$

where n is the charge carrier density and e is the electron charge. When there is less scattering in a material, the charge carriers will travel farther with the same electric field. This ratio is defined as the mobility, $\mu = v_d/E$ and is an important quantity that is used to characterize scattering in conductors. One can then express the resistivity of a material in terms of its mobility by:

$$\rho = 1/(\text{ne } \mu). \tag{1.4}$$

Hall Effect:

Physicists aren't limited to applying electrical forces to a material but love to apply magnetic forces as well. In a magnetic field, a moving charge experiences a Lorentz force. Using the Drude model with an applied magnetic field *B*, the current density is defined as:

$$\vec{J} = \frac{1}{\rho_0}\left(\vec{E} - \frac{1}{ne}\vec{j} \times \vec{B}\right) \tag{1.5}$$

which can be rewritten as:

$$\vec{E} = \rho_0 \vec{j} + \frac{1}{ne}\vec{j} \times \vec{B} \tag{1.6}$$

We can then formulate this equation in matrix form using Cartesian coordinates and under the assumption that we have a 2D system with a B field in the z direction and current in the xy plane. Doing so we get:

$$\begin{pmatrix} E_x \\ E_y \end{pmatrix} = \begin{pmatrix} \rho_0 & \frac{B}{ne} \\ -\frac{B}{ne} & \rho_0 \end{pmatrix} \begin{pmatrix} j_x \\ j_y \end{pmatrix} \tag{1.7}$$

Referring to Fig. 1.1, we define the Hall resistance, R_H, as:

$$R_H \equiv \frac{V_h}{I} \tag{1.8}$$

where:

$$V_h = \int E_y \cdot d\ell \tag{1.9}$$

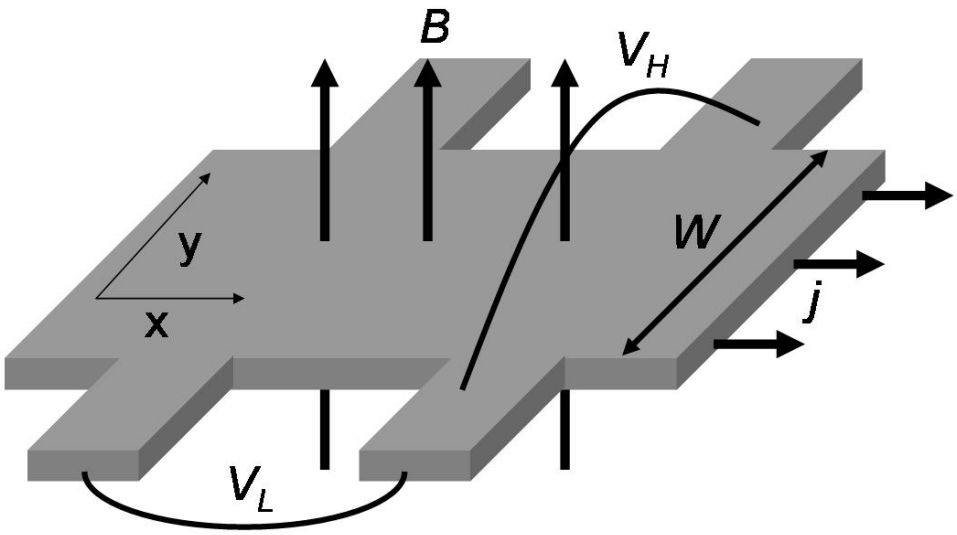

Figure 1.1 Hall Bar geometry.

With no current flow in the y direction (1.7) simplifies to:

$$E_y = -\frac{B}{ne} j_x \tag{1.10}$$

Plugging (1.10) into (1.9) we get:

$$V_h = \int \frac{B}{ne} j_x d\ell = \frac{B}{ne} j_x W \tag{1.11}$$

In 2 dimensions the current density is defined as:

$$j_x \equiv \frac{I}{W} \tag{1.12}$$

Using this fact along with the definition for the Hall voltage in (1.8) we have that:

$$R_H = \frac{B}{ne} \tag{1.13}$$

By sweeping a perpendicular magnetic field, B, and measuring R_H one can determine the carrier density, n. You can then use this density and the measured longitudinal resistivity ρ to measure the sample's mobility μ. This is a technique known as the Hall Effect and is commonly used to characterize conducting samples. We will use this in Chapter 4 to determine n, ρ, and μ for mesoscopic graphene pieces.

1.4 Two Dimensional Electron Systems

Up until this point, we concerned ourselves with 3 dimensional conductors. If the thickness of a conductor becomes smaller than the size of the electron wavelength than the conductor forms a two-dimensional electron gas (2DEG) and interesting

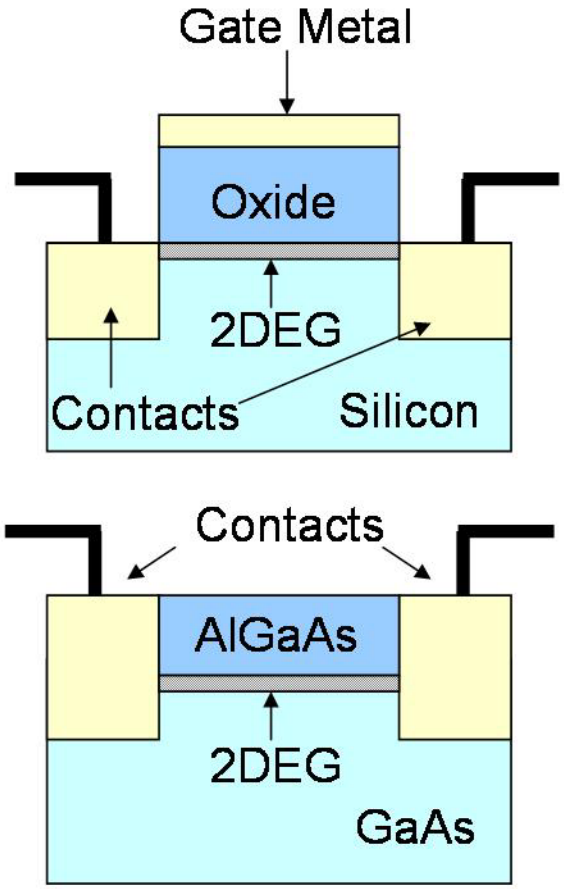

Figure 1.2. a) A silicon MOSFET where a metal gate is used to pull charges towards the Silicon/Silicon Oxide interface where the 2DEG is formed. b) A modulation doped GaAs/AlGaAs heterojunction. The 2DEG forms at the interface where charges introduced by silicon dopants are pulled to the interface by an electric field.

quantum effects arise. The first high mobility 2DEG was formed from a Si metal oxide semiconductor field effect transistor (MOSFET). Technologically, the Si MOSFET is the critical component behind the transistor and the modern computing revolution. A schematic of the MOSFET is shown in Fig. 1.2a. A SiO_2 insulating layer is grown on top of Si and an electrostatic force applied to the gate electrode is used to pull charges towards the Si/SiO_2 interface.

The high quality interface between a Si and SiO_2 can be fabricated into effective transistors and at low temperatures forms a relatively clean 2DEG which exhibits the QHE. The QHE in a silicon 2DEG was first demonstrated in 1980 by Klaus von Klitzing (Klitzing, Dorda et al. 1980). Despite the high quality of the Si/SiO_2 interface, there still remains sufficient scattering such that the mobilities have been limited to 8×10^4 $cm^2/V\text{-}s$ for the highest quality samples(Stormer 1999).

To circumvent the problem of scattering at a defective semiconductor-insulator boundary, researchers at Bell Labs invented a method called modulation doping which utilized Molecular Beam Epitaxy (MBE)(Dingle, Stormer et al. 1978). Using MBE, a technique developed in the 1960s by Albert Cho also of Bell Labs, semiconductors can be prepared layer by layer in a nearly perfect crystalline form and a clean interface between two semiconductors is prepared. Scientists at Bell Labs chose to use GaAs and AlGaAs due to their matching lattice constants. This allowed a crystalline interface between these 2 materials which was nearly perfect yet remained insulating due to a lack of charge carriers in these intrinsic semiconducting materials. To create a 2DEG, free charges must be generated. In the MOSFET situation, charges are introduced through an electrostatic gate above the oxide. For the case of the GaAs/AlGaAs heterojunction, researchers at Bell Labs had the clever idea of introducing impurity atoms far enough away from the interface such that they can donate their electrons but not contribute to scattering. In this case, called modulation

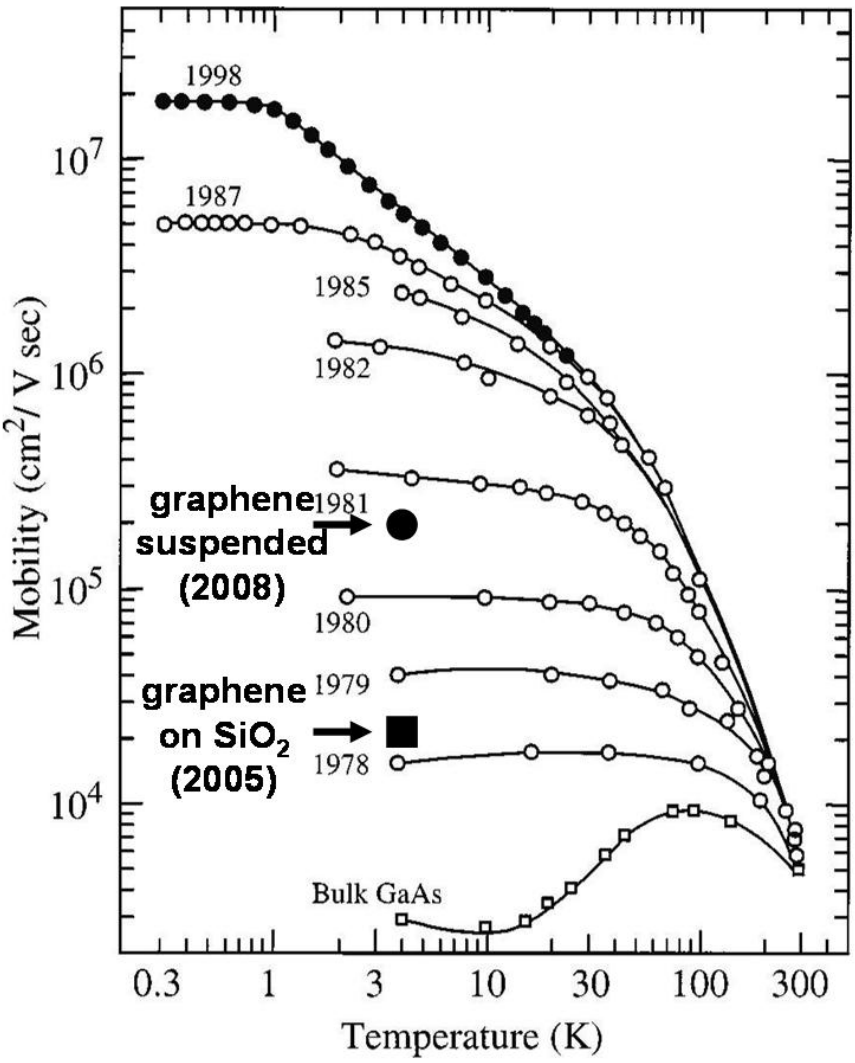

Figure 1.3 Progress made in improving the mobility of GaAs/AlGaAs heterojuntions. The solid black square (■) is the current mobility record for graphene on silicon oxide(Novoselov, Geim et al. 2005) (Zhang, Tan et al. 2005). The solid circle (●) is the current record for suspended graphene (Bolotin, Sikes et al. 2008). Figure adapted from (Stormer 1999)

doping, Si impurity atoms are introduced into the AlGaAs material during growth. When Si is substituted in for Ga in the lattice it releases its extra electron. Since the conduction band of GaAs is 0.19 eV below the conduction band of AlGaAs, negative charges fall toward the GaAs side but are attracted by the positive charges that remain on the AlGaAs side. This results in the bands bending and confining the charge at the "perfect" AlGaAs-GaAs interface thereby forming the 2DEG (Fig. 1.2b). Loren Pfeiffer and collaborators at Bell Labs have spent the last 2 decades perfecting their MBE system so as to make it as clean as possible. Progress in perfecting the quality of this interface is shown in Fig. 1.3 and mobilities larger than 10^7 have been achieved. These samples have a ballistic mean free path of about 120 μm for an electron confined to this interface and such high quality samples have allowed for the investigation of many exotic properties of electrons in 2 dimensions. These GaAs/AlGaAs samples are the current state of the art in terms of charge carrier mobility in solid state systems. As a comparison, the current record mobilities for graphene are also plotted.

1.5 Quantum Dots

If electrons in a conductor are confined in all 3 of their dimensions a 0 dimensional structure forms known as a quantum dot. Typically, quantum dots are conducting island connected to a reservoir of electrons by a tunnel barrier (Fig. 1.4a). They are most commonly patterned on AlGaAs 2DEGs due to the ease of fabrication and high quality electron gas in these structures (Fig. 1.4b). The electron gas is confined into small islands of charge using electrostatic gate. The electrostatic gates deplete the underlying gas thereby creating a confined geometry with entrance and exit channels to an electron reservoir. To properly localize a discrete number of electrons on the dot, a tunnel barrier with a resistance $R_t > h/2e^2$ is required. For

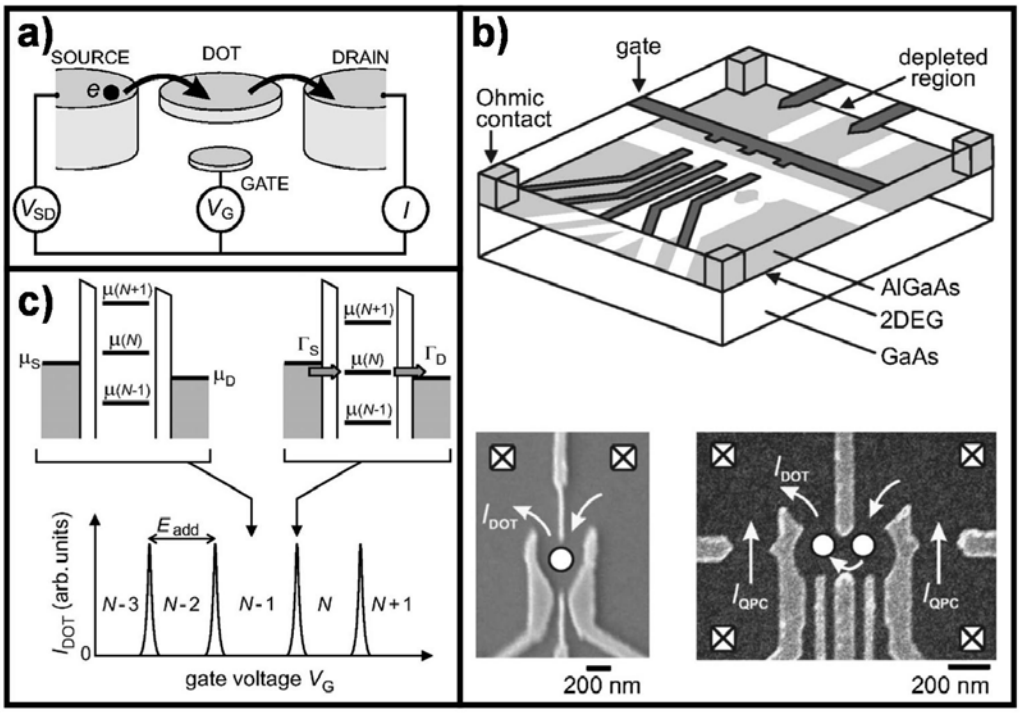

Figure 1.4 a) Schematic of a quantum dot connected to a source, drain, and gate electrode. b) (upper) Schematic of a quantum dot defined on an AlGaAs/GaAs heterostructure using gate defined depletion regions. (lower) Scanning electron microscope image of a single (left) and double (right) quantum dot. The white dot defines the region of electron confinement in the dot and the white arrows denote the conducting path of the electrons. The ohmic contacts to the dot are shown by black crosses. c) (upper) Energy levels in a quantum dot during coulomb blockade (left) and during conduction through the dot (right). (lower) Coulomb blockade oscillations. The spacing between the peaks is given by the energy to add an additional electron to the dot. Figure adapted from (Hanson, Kouwenhoven et al. 2007).

an electron to tunnel onto the dot, an energy cost must be paid given by e^2/C, where C is the total capacitance of the dot. This is known as the charging energy of the dot and having to pay this energy cost is known as Coulomb blockade. A small dot has a small capacitance and a large charging energy. When thermal fluctuations become smaller than this energy cost $e^2/C > kT$, single electron charging is observable.

This charging energy can be paid either with a voltage applied to a gate electrode or to the source or drain electrode. For a gate voltage, the addition of an electron onto the dot is simply:

$$\Delta V_g = e/C_g \tag{1.14}$$

where ΔV_g is the amount of voltage applied to the gate that shifts the charge on the dot by one electron and C_g is the gate-dot capacitance while for a source drain bias it is:

$$\Delta V_{sd} = e/C \tag{1.15}$$

where ΔV_{sd} is the amount of voltage applied to the source drain electrode and $C = C_s + C_d + C_g$. The ratio of these two voltages is defined by a constant α which is given by:

$$\alpha = \Delta V_{sd} / \Delta V_g = C_g / (C_s + C_d + C_g) \tag{1.16}$$

This constant defines the coupling of the dot to the gate and source drain electrodes.

By fixing the source drain bias and varying the gate voltage a series of oscillations in the current are observed (Fig. 1.4c). These are known as Coulomb oscillations and their spacing is given by ΔV_g. The current spikes result from the dot not knowing if it prefers N electrons or N+1 and so the dot alternates between these

two states. The requirement for this to occur is that an energy level on the dot is aligned with both the Fermi energy of the source and drain electrode (Fig. 1.4c).

It might be helpful to think of the current oscillations in a conducting quantum dot as a confused and frustrated system. When N electrons occupy the dot, it is happy and satisfied with the number of electrons residing in its humble little space. By changing the electrostatics of the system, the dot starts to think it can accommodate N+1 electrons instead of the N electrons which previously made it happy. During a Coulomb oscillation the dot's frustration is optimized and charges move across the dot as it shuttles electrons on and off. Eventually the electrostatics is such that the dot is no longer frustrated. Instead it is now happy to accommodate N+1 electrons. This situation repeats itself with N+1 and N+2 electrons.

In addition to the charging energy of the dot, there are additional quantum energy level spacings, ΔE. These excited states are a result of the higher order states of the electron wavefunction and are related to the density of states in the dot. For a two dimensional square dot with length L and charge carriers with a parabolic dispersion ΔE is given by:

$$\Delta E = \frac{\hbar^2}{\pi m L^2} \tag{1.17}$$

(Kouwenhoven, Marcus et al. 1997). A 100 nm 2D dot made from GaAs/AlGaAs, has $\Delta E \sim 30$ μeV which is 1000 times smaller than the corresponding charging energy $e^2/C \sim 30$ meV. A whole subfield of condensed matter physics grew out of the study of these frustrated little conducting islands. For a more extensive review of quantum dots discussing all of these situations please refer to (Kouwenhoven, Marcus et al. 1997).

1.6 Conclusion

This chapter reviews some of the interesting effects that arise when electrons in a conductor are confined to nanoscale dimensions. In Chapter 4 of this thesis, we will look at mescoscopic graphene electronic devices where electrons are confined in 2 and 0 dimensions in this unique material. In the next chapter, we will examine the mechanical properties of materials with a focus on characterizing nanoscale mechanical structures.

CHAPTER 2

NANOMECHANICS

2.1 Mechanical Properties of Materials

The mechanical equivalent to Ohm's law is Hooke's law. For a material in one dimension it is expressed as:

$$\sigma_x = E\varepsilon_x \tag{2.1}$$

where the stress σ is the force per unit area, E is the Young's modulus, and ε is strain. This assumes an isotropic system where there is no preferred crystal orientation. In many bulk solids, this is a valid assumption considering that single crystals tend to be separated into grains of random orientation. When taken as a whole the elastic constants average to some bulk value (Timoshenko 1934). Table 2.1 shows typical Young's modulus for various materials.

Most materials tend to contract in the direction perpendicular to the applied strain. The ratio of the strains in these 2 directions defines a quantity known as Poisson's ratio:

$$\upsilon \equiv -\frac{\varepsilon_y}{\varepsilon_x} \tag{2.2}$$

Typical Poisson's ratios are shown in Fig 2.1. Some materials like the cork of a wine bottle have $\upsilon \sim 0$ while others like rubber have $\upsilon \sim 0.5$. There is also exists a class of exotic materials with $\upsilon < 0$ (Fig. 2.1c).

Table 2.1 Approximate Young's modulus for various materials Adapted from Wikipedia: Young's Modulus.

Material	**Young's modulus (*E*) in GPa**
Rubber (small strain)	0.01-0.1
PTFE (Teflon)	0.5
Nylon	3-7
Oak wood (along grain)	11
High-strength concrete (under compression)	30
Aluminium alloy	69
Glass (see also diagram below table)	65-90
Titanium (Ti)	105-120
Copper (Cu)	110-130
Silicon (S)	150
Wrought iron and steel	190-210
Tungsten (W)	400-410
Silicon carbide (SiC)	450
Diamond (C)	1,050-1,200
Single walled carbon nanotube	1,000
Graphite/Graphene (within the plane)	1,000

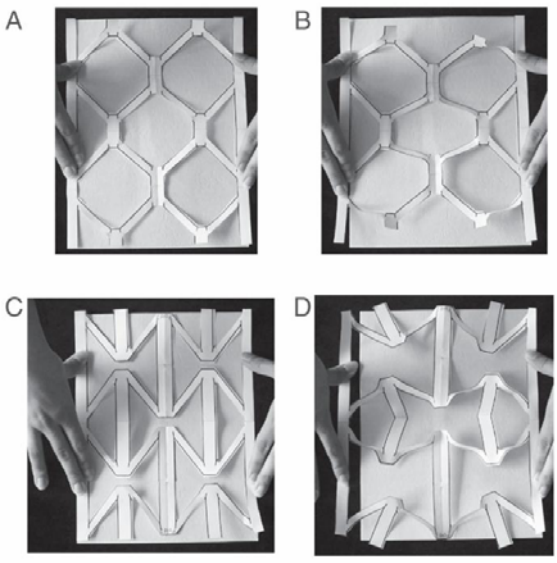

E

material	poisson's ratio
rubber	~ 0.50
titanium	0.34
copper	0.33
stainless steel	0.30-0.31
concrete	0.20
graphite	0.16-0.17
glass	0.18-0.3
cork	~ 0.00
auxetics	negative

Figure 2.1 A lattice with a positive Poisson's ratio: (A) unstretched and (B) stretched. Lattice with a negative Poisson ratio: (C) unstretched and (D) stretched. The sheet of paper behind each figure has the same dimensions. Figure from (Campbell and Querns 2002) (E) A table of Poisson's ratio for common materials. Adapted from Wikipedia-Poisson's ratio.

2.2 Anisotropic Materials

It is not always possible to assume a material is isotropic. This thesis is primarily concerned with single crystals and layered materials for which anisotropy is an important consideration. Stress and strain are second rank tensors and so relating stress to strain requires a fourth rank tensor which has 81 components. For real materials in equilibrium, there are no net forces and torques so the stress-strain relation is vastly simplified to the following 6 x 6 symmetric matrix (Senturia 2001):

$$\begin{pmatrix} \sigma_x \\ \sigma_y \\ \sigma_z \\ \tau_{yz} \\ \tau_{zx} \\ \tau_{xy} \end{pmatrix} = \begin{pmatrix} C_{11} & C_{12} & C_{13} & C_{14} & C_{15} & C_{16} \\ C_{12} & C_{22} & C_{23} & C_{24} & C_{25} & C_{26} \\ C_{13} & C_{23} & C_{33} & C_{34} & C_{35} & C_{36} \\ C_{14} & C_{24} & C_{34} & C_{44} & C_{45} & C_{46} \\ C_{15} & C_{25} & C_{35} & C_{45} & C_{55} & C_{56} \\ C_{16} & C_{26} & C_{36} & C_{46} & C_{56} & C_{66} \end{pmatrix} \begin{pmatrix} \varepsilon_x \\ \varepsilon_y \\ \varepsilon_z \\ \gamma_{yz} \\ \gamma_{zx} \\ \gamma_{xy} \end{pmatrix} \tag{2.3}$$

where τ is the shear stress and γ is the shear strain. For a cubic crystal such as silicon symmetry allows this equation to be further simplified to:

$$C_{ij} = \begin{pmatrix} C_{11} & C_{12} & C_{12} & 0 & 0 & 0 \\ C_{12} & C_{11} & C_{12} & 0 & 0 & 0 \\ C_{12} & C_{12} & C_{11} & 0 & 0 & 0 \\ 0 & 0 & 0 & C_{44} & 0 & 0 \\ 0 & 0 & 0 & 0 & C_{44} & 0 \\ 0 & 0 & 0 & 0 & 0 & C_{44} \end{pmatrix} \tag{2.4}$$

where the elastic constants for silicon are C_{11} = 166 GPa, C_{12} = 64 GPa, and C_{44} = 80 GPa (Senturia 2001). Graphite is a special case where the elastic constants along the plane are vastly different than those between the sheets. The various elastic constants

of graphite will be further examined in Chapter 3.

2.3 Biaxial Strain

Equations (2.1) and (2.2) can be combined to give the isotropic three dimensional version of Hooke's law which relates stress to strain as:

$$\varepsilon_{xx} = \frac{1}{E}\left(\sigma_{xx} - \nu\left(\sigma_{yy} + \sigma_{zz}\right)\right) \tag{2.5}$$

Biaxial strain is a common type of strain where both the x and z component of strain are equivalent: $\varepsilon_x = \varepsilon_z = \varepsilon$. An example is the surface of a spherical balloon where a pressure difference across the balloon applies an equal strain to both directions. For biaxial strain of an isotropic plate, the modified form of Hooke's law simplifies to:

$$\sigma = \left(\frac{E}{1-\upsilon}\right)\varepsilon . \tag{2.6}$$

It should be noted that cubic crystals are biaxially isotropic along the (111) and (100) planes.

2.4 Bulge Test

The bulge test is a method commonly used to measure the in-plane mechanical properties of thin films such as Young's modulus, residual stress, and Poisson's ratio (Vlassak and Nix 1992; Jay, Christian et al. 2003). The following discussion follows closely the lecture notes of Professor William Nix at Stanford University (Nix 2005). In the simplest implementation, a pressure difference is applied across a clamped circular film with a radius of curvature R and the maximum deflection, z, at the top of the film is measured. The pressure difference, Δp, applies a well defined and uniform

force across the membrane of thickness t, which is balanced by the induced biaxial stress, σ, in the membrane:

$$\Delta p \cdot \pi R^2 = \sigma \cdot 2\pi R t \tag{2.7}$$

$$\sigma = \frac{\Delta p R}{2t} \tag{2.8}$$

For the case of small deflection where (z<<a), the Pythagorean Theorem can be used to express the radius of curvature in terms of the radius of the base, a, as:

$$R \approx \frac{a^2}{2z} \tag{2.9}$$

We can then plug (2.9) into (2.8) to get:

$$\sigma = \frac{\Delta p a^2}{4tz} \tag{2.10}$$

or expressed as a surface tension $S = \sigma t$, this becomes:

$$S = \frac{\Delta p a^2}{4z} \tag{2.11}$$

The strain in the membrane is

$$\varepsilon = \frac{R\vartheta - a}{a} \approx \frac{a^2}{6R^2}. \tag{2.12}$$

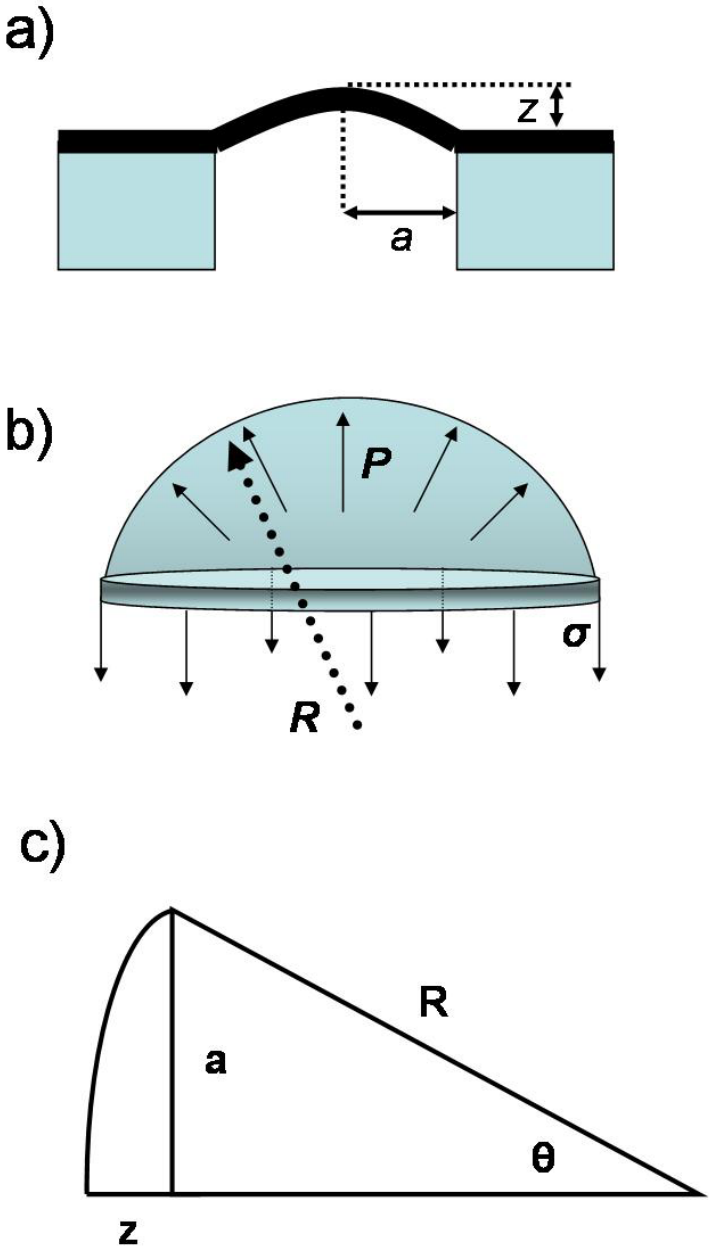

Figure 2.2 (a-c) Schematic of the Bulge test.

By plugging in (2.9) into this expression we get:

$$\varepsilon \approx \frac{2z^2}{3a^2} \tag{2.13}$$

Equation (2.6) is used to obtain the surface tension S due to biaxial elastic strain:

$$S = \frac{Et}{(1-\upsilon)}\varepsilon \tag{2.14}$$

This can be combined with (2.13) to express a pressure induced surface tension S_p:

$$S_p = \frac{2Etz^2}{3a^2(1-\upsilon)} \tag{2.15}$$

The total surface tension S can be written as the initial surface tension S_0 added to the pressure induced surface tension S_p. Setting this equal to (2.11) we get:

$$S = S_p + S_0 = \frac{2Etz^2}{3a^2(1-\upsilon)} + S_0 = \frac{\Delta p a^2}{4z} \tag{2.16}$$

Solving (2.16) for the pressure difference gives the "bulge equation" for a circular membrane:

$$\Delta p = \frac{4S_o z}{a^2} + \frac{8Etz^3}{3a^4(1-\upsilon)} \tag{2.17}$$

For the geometry of a square membrane, the equation is slightly modified to (Vlassak and Nix 1992):

$$\Delta p = \frac{4z}{W^2}\left(c_1 S_o + \frac{4c_2 Etz^2}{W^2(1-\upsilon)}\right) \tag{2.18}$$

where $c_1 = 3.393$ and $c_2 = (0.8+0.062\upsilon)^{-3}$ and for a rectangle this becomes (Nix 2005):

$$\Delta p = \frac{4z}{W^2}\left(2S_o + \frac{16Etz^2}{3W^2(1-\upsilon^2)}\right) \tag{2.19}$$

where W is the length along the short end of the rectangle.

Using equations (2.18) and (2.19) one can measure E and υ by a bulge test performed on the same material in a square and rectangular geometry. The 2 measured deflections will lead to 2 equations with 2 unknowns (E and υ). Chapter 6 of this thesis applies the bulge test for the first time to atomic scale membranes to extract the elastic constants of graphene. The experiments in this thesis only measured a combination of E and υ and not each independently since we studied only a square membrane.

2.5 Nanoindentation

A common alternative to the bulge test for measuring the elastic constant of free standing structures is nanoindentation. Commonly, an Atomic Force Microscope tip with a calibrated spring constant and well-known radius of curvature is used to push on a suspended structure and the deflection of the structure and tip is measured. From such a force-displacement curve it is possible to deduce the local spring constant of the free standing structure. Neglecting the bending rigidity, the tension can be obtained from the measured spring constant k, at the center of the membrane using $S \approx (k/2\pi)\ ln\ (R/r)$, where R is the radius of the membrane and r is the radius of the AFM tip (Tanizawa and Yamamoto 2004). A detailed theoretical review of this technique for indentation of thin films in the membrane regime can be found in (Begley and Mackin 2004).

This technique has been used by others to determine the mechanical properties of few layer graphene sheets (Frank, Tanenbaum et al. 2007; Poot and van der Zant 2008). In Chapter 6 of this thesis, we apply this technique to a single layer graphene membrane to determine the initial tension.

2.6 Harmonic Oscillator

The harmonic oscillator is a classic well-studied system which describes everything from grandfather clocks and guitars to atoms and dark energy. Historically, it has played a pivotal role in the development of both classical and quantum physics. A simple example is a pendulum which has an oscillation frequency proportional only to its length as first observed by Galileo in the early 17th century. Another common example is a mass on a spring. For small displacements, the spring follows Hooke's law, $F = kx$ where x is the displacement from equilibrium and k is the spring constant.

Real life situations involve damping terms which dissipate the vibrational energy of the system killing the vibration. We will denote this by a constant b. We typically also need to drive the oscillations so we include a periodic driving force with amplitude F and frequency ω. These two terms will modify our equation of motion to:

$$M\frac{d^2x}{dt^2} + c\frac{dx}{dt} + kx = F\cos(\omega t) \tag{2.21}$$

The steady state solution to this equation is given by the following:

$$x = A\cos(\omega t - \vartheta) \tag{2.22}$$

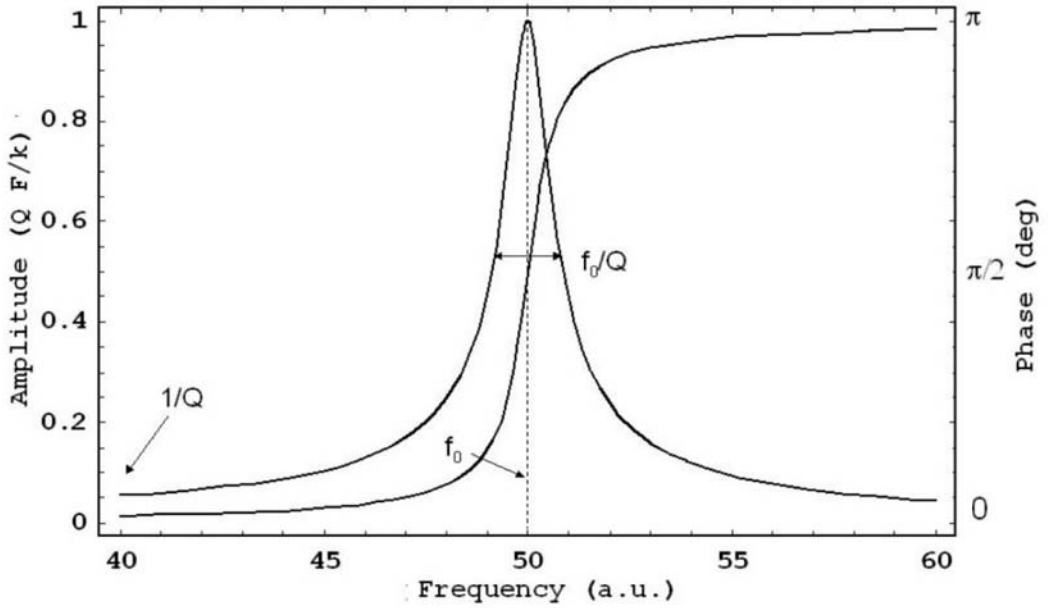

Figure 2.3 The amplitude and phase of a driven damped harmonic oscillator. Figure from (Sazonova 2006).

where

$$A = \frac{F}{k} \frac{Q}{\sqrt{Q^2\left(1-\frac{\omega^2}{\omega_0^2}\right)^2 + \left(\frac{\omega}{\omega_0}\right)^2}} \tag{2.23}$$

$$\vartheta = \tan^{-1}\left(\frac{\omega\omega_0}{Q\left(\omega_0{}^2 - \omega^2\right)}\right) \tag{2.24}$$

$$\omega_0 = \sqrt{\frac{k}{M}} \tag{2.25}$$

$$Q = \frac{m\omega_0}{c} \tag{2.26}$$

(Timoshenko, Young et al. 1974). The resonance frequency is given by $\omega_0 = 2\pi f_0$, the phase is θ, and Q is the quality factor. The damping term prevents the resonance amplitude from going to infinity at the drive amplitude. The maximum amplitude QF/k is at the resonance frequency and the full-width at half maximum of the resonant peak is f_0/Q (Fig. 2.3).

2.7 Doubly Clamped Beams and Cantilevers

The simple harmonic oscillator can be used to describe the dynamic properties of suspended elastic beams. The fundamental resonance frequency for a suspended beam with clamped fixed ends is given by:

$$f = f_0\sqrt{1 + \frac{SL^2}{3.4Et^3}} \tag{2.27}$$

where

$$f_0 = A\sqrt{\frac{E}{\rho}}\frac{t}{L^2} \tag{2.28}$$

and E is the Young's modulus, S is the tension per width, ρ is the mass density, t and L, are the thickness and length of the suspended graphene sheet, and A = 1.03 for doubly-clamped beams and 0.162 for cantilevers (Timoshenko, Young et al. 1974; Bokaian 1990)

2.8 Membrane Dynamics

The 2-dimensional version of a tense string is a stretched membrane. In the limit of a large uniform tension S, along the length of the boundary the bending rigidity can be neglected. This simplifies the potential energy of the displaced membrane, and one can solve for the vibration frequencies using the principle of virtual displacements(Timoshenko, Young et al. 1974). The vibration frequencies for a rectangular membrane are:

$$f_{i,j} = \frac{1}{2}\sqrt{\frac{S}{m}\left(\frac{i^2}{a^2}+\frac{j^2}{b^2}\right)} \tag{2.29}$$

where m is the mass per unit area, a and b are the lengths of each side (Timoshenko, Young et al. 1974). For the fundamental mode of a square membrane this simplifies to:

$$f_{1,1} = \sqrt{\frac{S}{2ma^2}} \tag{2.30}$$

A circular membrane of radius r, has the slightly modified form of the fundamental mode (Timoshenko, Young et al. 1974):

$$f_{1,1} = 2.404\sqrt{\frac{S}{mr^2}} \tag{2.31}$$

2.9 Plate Dynamics

When the tension in the membrane is small, the stiffness is dominated by the flexural rigidity, D:

$$D = \frac{Et^3}{12(1-\upsilon^2)}. \tag{2.32}$$

As the elastic sheet vibrates out of plane, the potential energy due to small displacements comes from this flexural rigidity instead of the tension. This structure is referred to as a plate. If one assumes simply supported edges, the vibration frequencies for a rectangular plate are:

$$f_{i,j} = \frac{\pi}{2}\sqrt{\frac{D}{\rho t}}\left(\frac{i^2}{a^2} + \frac{j^2}{b^2}\right) \tag{2.33}$$

This simplifies to the following for the fundamental mode of a square plate:

$$f_{1,1} = \frac{\pi}{a^2}\sqrt{\frac{D}{\rho t}} \tag{2.34}$$

The case of a rectangular plate with all edges free or clamped is significantly more difficult to solve. An approximate solution for a circular plate with a radius r, fixed at the boundary gives a fundamental frequency:

$$f_{1,1} = \frac{10.21}{r^2}\sqrt{\frac{D}{\rho t}} \tag{2.35}$$

2.10 Actuation

One of the most common methods to actuate vibrations in suspended beams is electrostatic drive. This uses an alternating electric field to drive the resonant motion of the beam. A capacitor is formed between the electrically contacted suspended beam and a nearby gate electrode. A voltage V_g, applied to this capacitor induces a charge $q = C_g V_g$ onto the beam where C_g is the capacitance of the beam to the gate electrode. The total electrostatic force on this beam is then given by:

$$F_{el} = \frac{1}{2}\frac{dC_g}{dz}V_g^2 \tag{2.36}$$

where z is the distance to the gate electrode. A small AC voltage is combined with a DC voltage to give:

$$V_g = V_g^{DC} + \delta V_g \tag{2.37}$$

Combining (2.36) with (2.37) we get:

$$F_{el} \approx \frac{1}{2}C_g'\left(V_g^{DC}\right)^2 + C_g' V_g^{DC}\delta V_g \tag{2.36}$$

where we have neglected the small term δV_g^2.

A useful technique to actuate out of plane vibrations in resonators without electrical contacts is an optical drive. This operates by locally modulating the temperature on or near a resonator using a focused laser. The thermal drive works

either by actuating the graphene itself through thermal contraction and expansion or the graphene/SiO_2 clamping point or through thermal stresses at this interface due to the different thermal expansion coefficients of SiO_2 and graphene (Ilic, Krylov et al. 2005). Both will result in a periodic driving force that causes resonant motion in the resonator.

If the resonant motion is due to thermal expansion and contraction of the suspended graphene itself, then the maximum attainable frequency can be estimated from the thermal properties of graphene. For a well clamped graphene resonator thermal expansion along the length of the graphene will lead to out of plane motion. For such an actuation scheme to work, the thermal time constant, $1/\lambda$ of the resonator must be smaller than the out of plane vibrations to allow for thermal equilibration. For a circular resonator of radius R, λ is given by:

$$\lambda = \frac{\kappa}{c\rho}\left(\frac{\mu}{R}\right)^2 \tag{2.37}$$

where c is the specific heat, ρ is the mass density, κ is the thermal conductivity, and $\mu = 2.4$ is a root of the Bessel function J_0 (Aubin 2005). Using typical values for the suspended graphene resonators in this thesis, this corresponds to a thermal time constant $1/\lambda$, = 0.2 ns which places an upper bound of the optical drive at ~ 5 GHz. This is considerably larger than the typical fundamental resonant frequencies we observe ~ 50 MHz.

2.11 Optical Detection

Just as electrical and optical means can be used to actuate resonant motion, they can also be used to detect motion. Optical techniques have the advantage of high sensitivity and the simplicity of not requiring any electrical contacts. All work in this

thesis used optical detection so I refer the reader to Vera Sazonova's thesis for an overview of electrical detection schemes (Sazonova 2006).

Beam Deflection:

Those of us who have ever used an Atomic Force Microscope (AFM) are familiar with optical detection to measure the resonance frequency of a cantilever. An AFM uses a beam deflection method where a laser beam is reflected off of the backside of a cantilever and onto a split-photodetector (Fig. 2.4a). The laser spot is positioned such that the light incident on the photodetector is divided evenly between the 2 regions of the photodector. As the cantilever vibrates, the relative intensity between these 2 regions changes and resonant motion is detected.

Interferometric Detection:

A more sensitive means of detecting motion optically is to utilize the interference effect resulting from two wave fronts of light. For a Michelson-Morley interferometer, a single beam of light is split into two beams one of which is incident on the sample and the other onto a reference mirror (Fig. 2.4b). The beams then recombine and an interference pattern results. In Fabry-Perot interferometry a single beam is incident on a partially reflecting reference mirror and a back mirror directly behind and parallel to the reference mirror (Fig. 2.4c). The light reflected from the reference mirror combines with that reflected off of the back mirror to form an interference pattern. It should be noted that for NEMS which reflect very little light one can neglect multiple reflections in the Fabry Perot cavity.

The advantage of Fabry-Perot detection for NEMs applications is that the 2 mirrors are typically parallel and close together making the setup less sensitive to mechanical vibrations. The disadvantage is that it is impossible to directly measure the displacements. In Michelson-Morley interferometry the reference mirror can be moved a calibrated distance and therefore absolute displacement detection is possible.

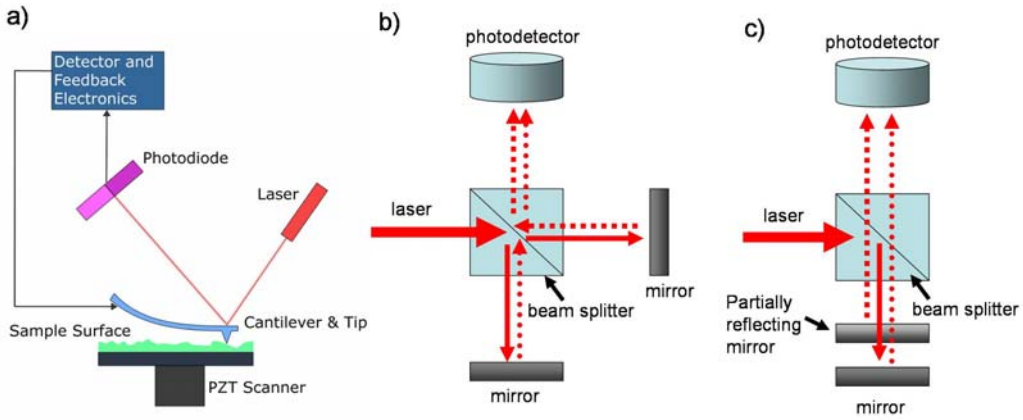

Figure 2.4 a) Schematic of an Atomic force microscope which uses the beam deflection method of detection. Figure taken from Wikipedia/Atomic Force Microscope b) Schematic of a Michelson-Morley detection scheme. c) Schematic of a Fabry-Perot detection scheme.

The disadvantage is the increased mechanical noise in such a setup. This is improved by utilizing a path stabilized variant(Karabacak 2008). For a detailed review of these interferometric detection techniques as applied to nanolectromechanicals systems I refer the reader to (Shagam 2006; Karabacak 2008). Chapter 5 and 6 of this thesis uses Fabry Perot interfermetry to detect the resonant motion of graphene NEMS.

2.12 MEMS and NEMS Applications

Microelectromechanical systems (MEMS) have established themselves as commercially viable components in a range of products from MEMS-based accelerometers found in air bag deployment systems and gyroscopes in car electronic stability control. The most dominant market for MEMS is in ink jet printer nozzles. One can even find MEMS in new video game systems such as Nintendo Wii where accelerometers are used to sense motion in the hand held game controller. The MEMS market in 2007 is $7.1 billion and expected to rise to $14 billion by 2012 (Fig. 2.5). Most of this growth is expected to take place in non-traditional areas of MEMS such as RF-MEMS which utilize MEMS for RF signal processing, microfluidic chips for drug delivery, silicon microphones, microfluidic chips for diagnostics, micro tips and probes, and micro-bolometers which can be used as infrared detectors for thermal imaging (Staff 2008)(Fig. 2.5b).

One of the more promising applications of NEMS which are the nano version of MEMS is in sensing. The advantage of NEMS is that smaller is usually better. Three opportunities for NEMS where there small size is particularly advantageous are in force, mass, and charge sensing. These are explored in Chapter 5 of this thesis.

2.13 Conclusions

This chapter reviewed some of the aspects relevant to the experimental

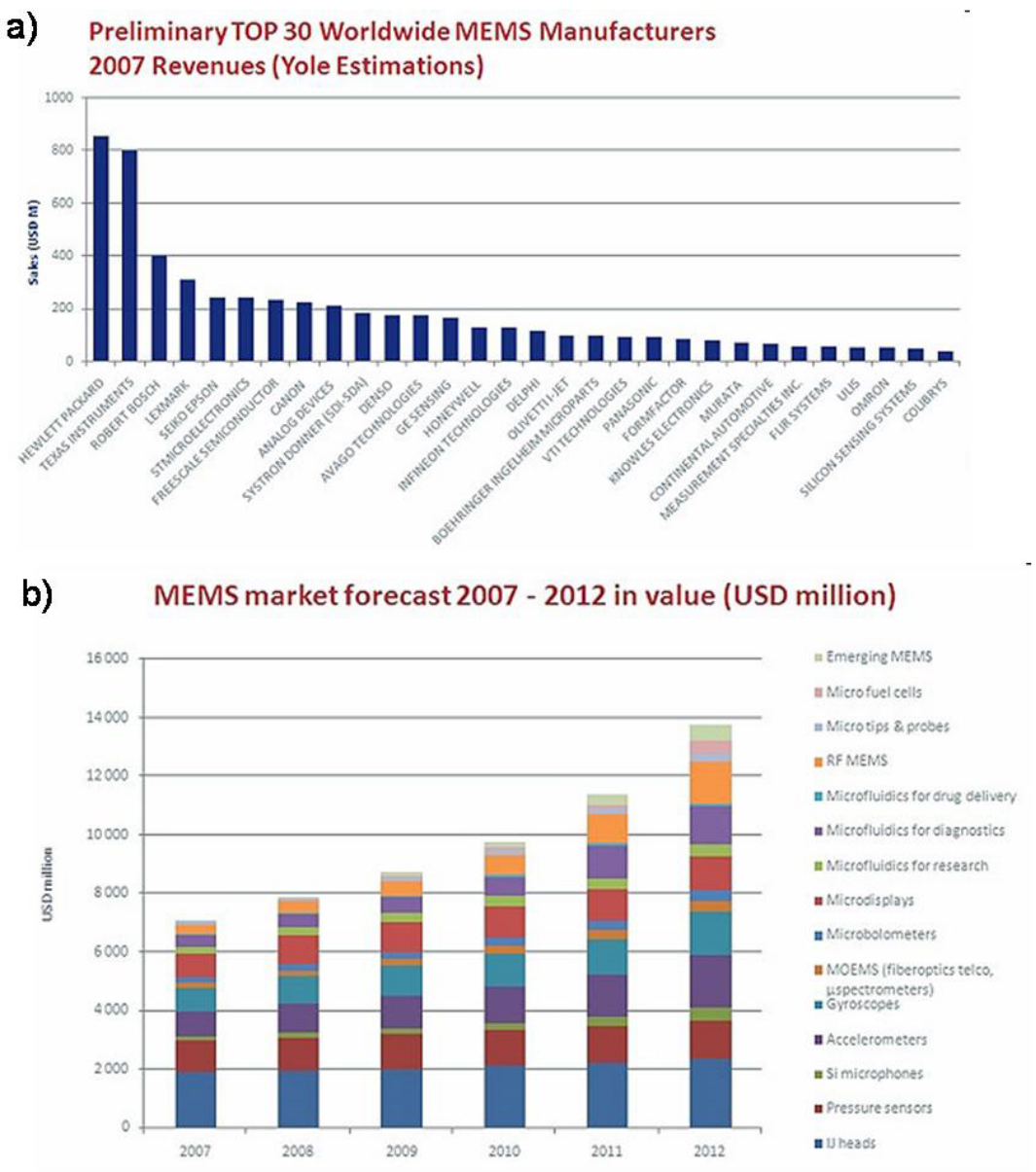

Figure 2.5 a) Top 30 MEMS manufacturers worldwide based on 2007 revenues according to Yole. b) MEMS market forecast 2007-2012. (Figures from (Staff 2008))

nanomechanics results presented in Chapter 5 and Chapter 6 of this thesis. In the next chapter, we will review the properties of graphene - the material of focus of this thesis.

CHAPTER 3

GRAPHENE

3.1 Carbon vs. Silicon

We currently live in the age of silicon nanotechnology. Silicon based transistors drive the modern computing revolution. The size of transistors has consistently been decreasing allowing more transistors to be packed onto a single chip thereby increasing computer power. This rate approximately follows Moore's law which states that the number of transistors on a chip is doubling approximately once every 2 years. The economic reason for such a phenomenal rate is the ~ $1 trillion computer market is driven by a worldwide demand for faster and more affordable computers. The physical reason behind the growth rate is the ability of engineers and scientists to fashion silicon into smaller and more efficient computer circuitry. The most recent Intel processor has a transistor with a channel length of 45 nm – a true nanotechnology (Fig. 3.1a and 3.1b)

More recently this ability to control silicon fabrication has extended into the mechanical realm where interest in silicon as a mechanical material has driven MEMS technology (Petersen 1982)(Fig. 3.1c and 3.1d). As previously discussed in Chapter 2.12, silicon MEMS are finding applications in a wide array of products. Silicon fabrication processes and equipment are readily available due to the microelectronics boom making silicon a natural choice for MEMS. But is silicon the best choice? A potential alternative to silicon is carbon which forms several distinct structures that have superior electrical, mechanical, and thermal properties to silicon.

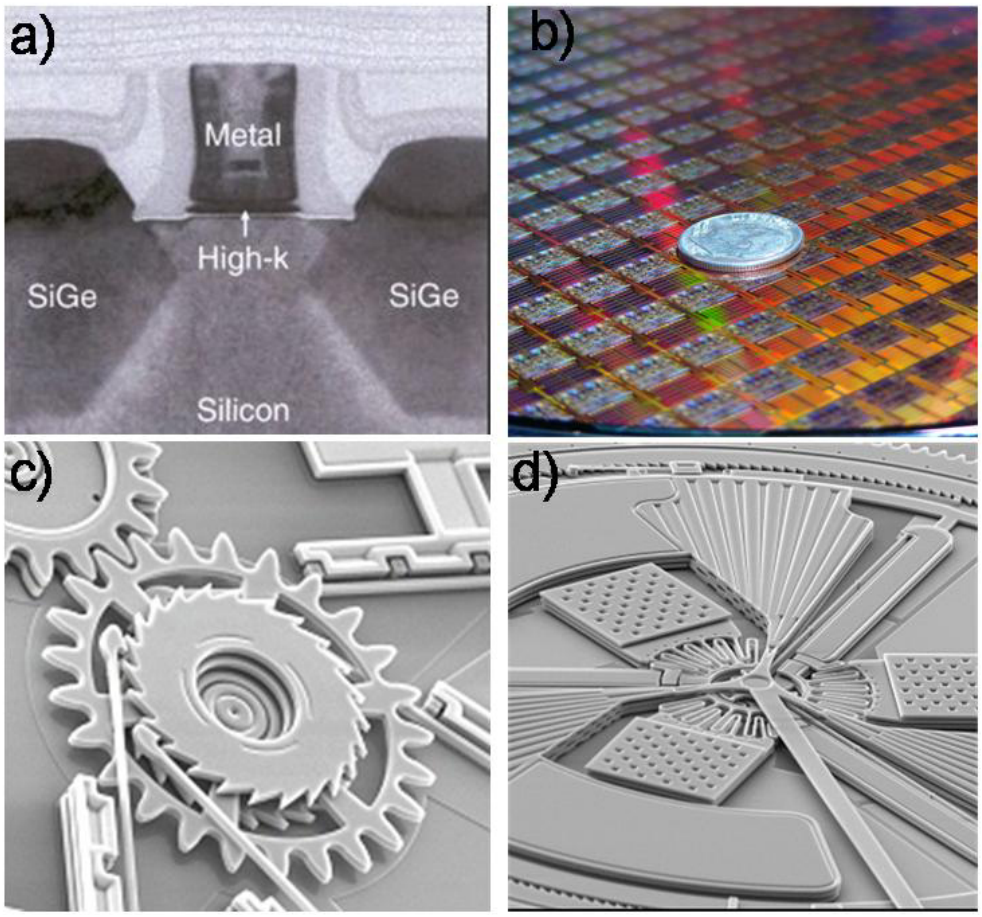

Figure 3.1 (a) Intel's 45 nm transistor which uses a Hafniun based dielectric. (b) A wafer of the 45 nm transistors photographed with a dime. The processors incorporate 410 million transistors for each dual core chip, and 820 million for each quad core chip. Figures taken from http://www.intel.com/pressroom/kits/45nm/photos.htm. (c-d) Images of MEMS from Sandia Labs. Images taken from Sandia MEMS webpage.

3.2 Forms of Carbon

Carbon sits directly above silicon on the periodic table and therefore both have 4 valence electrons. However, unlike silicon, carbon's 4 valence electrons have very similar energies, so their wavefunctions mix easily facilitating hybridization. In carbon, these valence electrons give rise to 2s, $2p_x$, $2p_y$, and $2p_z$ orbitals while the 2 inner shell electrons belong to a spherically symmetric 1s orbital that is tightly bound and has an energy far from the Fermi energy of carbon. For this reason, only the electrons in the 2s and 2p orbitals contribute to the solid-state properties of graphite. This unique ability to hybridize sets carbon apart from other elements and allows carbon to form 0D, 1D, 2D, and 3D structures (Fig. 3.2) (Saito, Dresselhaus et al. 1998).

Diamond:

The three dimensional form of carbon is diamond. It is sp3 bonded forming 4 covalent bonds with the neighboring carbon atoms into a face-centered cubic atomic structure (Fig. 3.2a). Because the carbon-carbon covalent bond is one of the strongest in nature, diamond has a remarkably high Young's modulus and high thermal conductivity. Undoped diamond has no free electrons and is a wide band gap (~5.5 eV) insulator (Singh 1993).

The exceptional physical properties and clever advertising such as "Diamonds are forever" contribute to its appeal as a sought after gem. When properly cut and polished, it is set to make beautiful pieces of jewelry. One of the most famous of these is the Hope Diamond shown in Fig. 3.2b. For many of the large, high quality crystals used to make jewelry, diamond must be mined. The smaller defective crystals are used as reinforcement in tool bits which utilize its superior hardness for cutting applications. The supply of diamonds is well controlled at the few diamond mines scattered around the world stabilizing the high price and maintaining the demand for

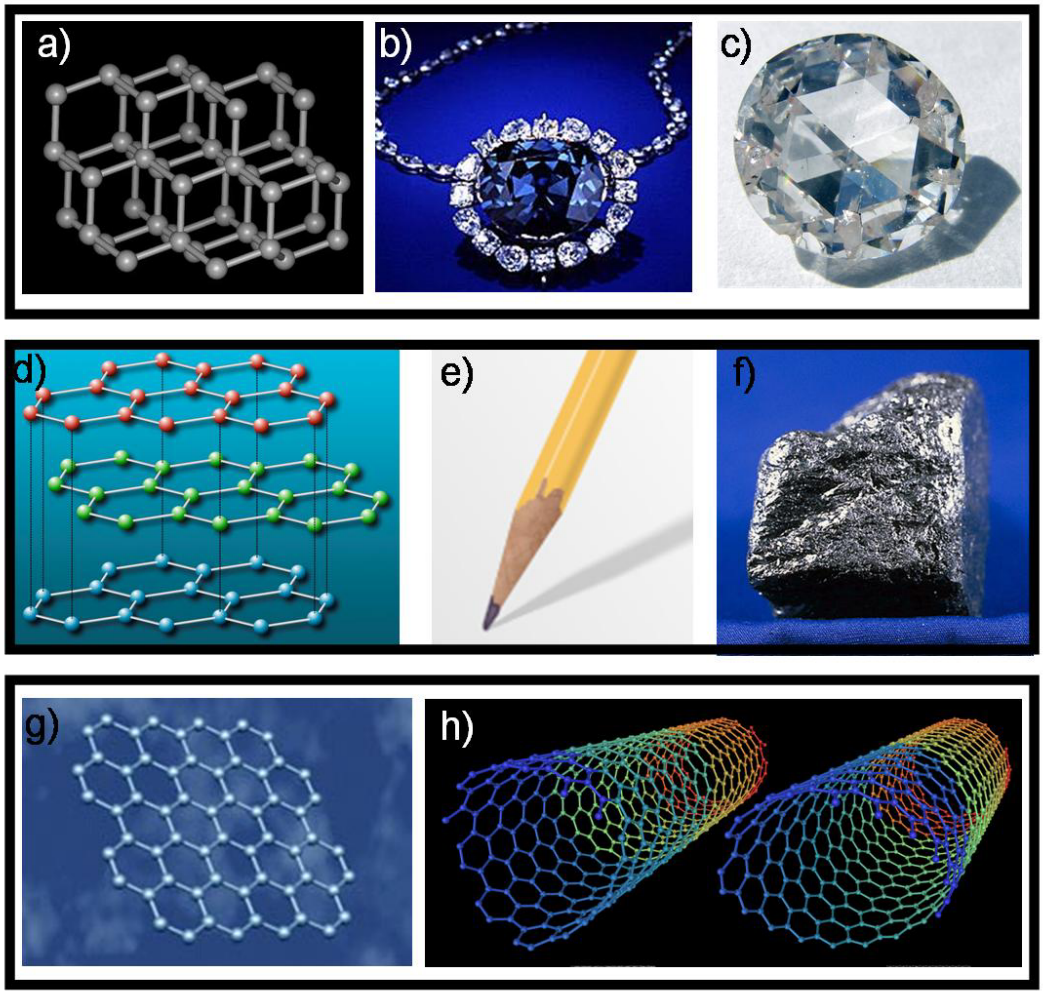

Figure 3.2 a) Diamond lattice. Picture taken from http://mrsec.wisc.edu b) Hope Diamond. Image from Smithsonian. c) Lab grown diamond. Image from Apollo diamond, Inc. d) Graphite lattice. Image from. http://www.scifun.ed.ac.uk/ e) Pencil. Image from www.xara.com. f) Graphite. Image from U.S. Geological Survey. g) single layer of graphene. Image from http://ewels.info.com. h) Single walled carbon nanotubes. Image created by Michael Ströck from Wikipedia.

this prized gemstone.

The high thermal conductivity of diamond makes it a potentially useful material for microelectronics where heat dissipation is currently a major problem. However, diamond's scarcity makes this unappealing. To this end, scientists and engineers are trying to grow large diamond wafers. One method to do so is chemical vapor deposition (CVD) where solid carbon is deposited from carbon containing gases such as methane or ethylene. By controlling the growth conditions, it is possible to produce defect free diamonds of limited size. An example of a high quality diamond grown by this technique is shown in Fig. 3.2c. Currently this technique is producing diamonds for jewelry and research is ongoing to scale the technology up to wafer size diamond growth. It is only with such large scale growth that diamond will make any technological impact beyond its current industrial uses in the machining industry.

Fullerenes:

More exotic forms of carbon are the low dimensional forms known as the fullerenes which consist of the 0 dimensional C_{60} molecule and its 1 dimensional derivative, carbon nanotubes. A single walled carbon nanotube is a single layer of graphite, referred to as graphene, rolled into a cylindrical tube with a ~ 1 nm diameter (Fig. 3.2h). Carbon nanotubes can be metals or semiconductors and have mechanical properties similar to diamond. They attracted a lot of attention from the research community and dominated the scientific headlines during the 1990s and early 2000. This interest in nanotubes was partly responsible for the resurgent interest in graphene as a potentially important and interesting material for electrical and mechanical applications.

Graphene and Graphite:

Graphene and Graphite are the two dimensional sp2 hybridized forms of carbon found in pencil lead (Fig. 3.2e). Graphite is a layered material formed by stacks

of graphene sheets separated by 0.3 nm and held together by weak van der Waals forces (3.2d) (Kelly 1981). The weak interaction between the sheets allows them to slide relatively easily across one another. This gives pencils their writing ability and graphite its lubricating properties, however the nature of this interaction between layers is not entirely understood. It has been known for decades that the presence of water reduces the frictional force considerably (Savage 1948; Pertsin and Grunze 2006). Another frictional effect believed to be important is the registry of the lattice between the layers. A mismatch in this registry is believed to give graphite the property of superlubricity where the frictional force is reduced considerably (Dienwiebel, Verhoeven et al. 2004). Mechanical experiments based on few layer graphene may help to elucidate some of these mechanisms clearly (Zheng, Jiang et al. 2008).

A single 2-D sheet of graphene is a hexagonal structure with each atom forming 3 bonds with each of its nearest neighbors (Fig. 3.2g). These are known as the σ bonds oriented towards these neighboring atoms and formed from 3 of the valence electrons. These covalent carbon-carbon bonds are nearly equivalent to the bonds holding diamond together giving graphene similar mechanical and thermal properties as diamond. The fourth valence electron does not participate in covalent bonding. It is in the $2p_z$ state oriented perpendicular to the sheet of graphite and forms a conducting π band. The remarkable electronic properties of carbon nanotubes are a direct consequence of the peculiar band structure of graphene, a zero bandgap semiconductor with 2 linearly dispersing bands that touch at the corners of the first Brillouin zone (Wallace 1947). Bulk graphite has been studied for decades (Kelly 1981) but until recently there were no experiments on graphene. This was due to the difficulty in separating and isolating single layers of graphene for study.

3.3 Graphene Fabrication

The most common method of graphene fabrication is exfoliation which finds its roots with a technique that has been around for centuries – writing with a graphite pencil. By writing with a pencil you create many graphene sheets spread over your paper. Unfortunately this method is uncontrollable and you are typically left with many sheets of varying thicknesses. If you want to study a single graphene sheet you need to locate it. The problem amounts to trying to find a needle in a haystack. A way around this problem was solved by Andre Geim's group in Manchester (Novoselov, Geim et al. 2004). By gently rubbing or pressing a freshly cleaved graphite crystal on an oxidized silicon wafer graphene flakes with the correct thickness of oxide, single atomic layers are visible under an optical microscope due to thin film interference effects (Novoselov, Jiang et al. 2005; Blake, Hill et al. 2007). This technique simplifies the process of finding single graphene sheets but obviously limits this fabrication scheme to devices for research purposes. For the case of suspended graphene sheets as discussed in this thesis, this process may take ~ 1 hour to find relatively thin ~ 1-5 nm thick suspended graphene devices but could take several days or weeks to find a suitable single suspended layer.

There are recent attempts to improve the quality and yield of exfoliation techniques. These include stamping methods which use silicon pillars to transfer graphene flakes and electrostatic voltage assisted exfoliation which uses electrostatic forces to controllably separate graphene from bulk crystals (Liang, Fu et al. 2007; Sidorov, Yazdanpanah et al. 2007). These are very recent developments and only time will tell whether they yield significant improvement over standard exfoliation.

Another common graphene fabrication technique is to disperse graphene from solution. This technique was used in Chapter 4 to fabricate few layer graphene quantum dots (Bunch, Yaish et al. 2005). In this method graphite flakes are sonicated

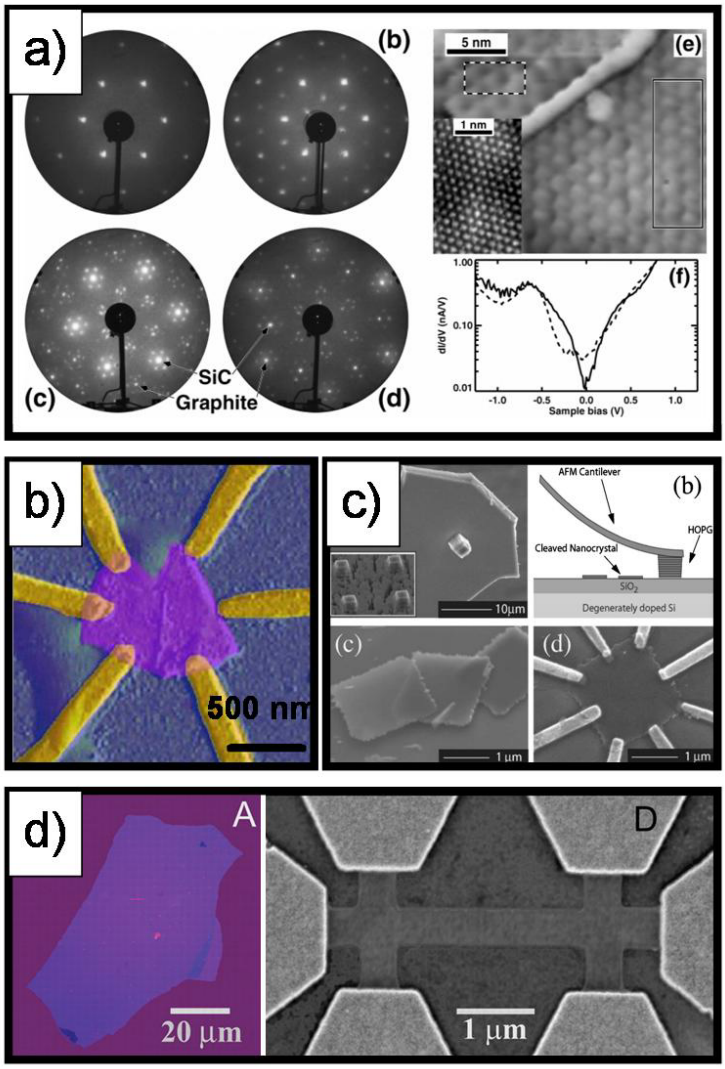

Figure 3.3 a) Growing few layer graphene on SiC. (figure from (Berger, Song et al. 2004). b) AFM image of a few layer graphene quantum dot fabricated by dispersion from solution. (figure adapted from (Bunch, Yaish et al. 2005). c) Nanopencil used to extract few layer graphene flakes from HOPG. Figure from (Zhang, Small et al. 2005). Optical image of a few-layer graphene sheet. Figures from (Novoselov, Geim et al. 2004).

in a solution and then dispersed onto a wafer. An AFM is used to locate individual sheets making this technique very time consuming relative to the optical detection scheme. Long sonication times are needed to break the graphite down and this typically results in small flakes. Recently a similar technique was used to fabricate graphene ribbons with nm-scale widths (Li, Wang et al. 2008). One of the difficulties in dispersing graphene from solution is separating the layers without breaking them. A way around this is to intercalate the graphite and dissolve it in a solvent. When the intercalant dissolves it separates the graphene sheets. This technique was shown to work effectively for graphene oxide**.** However, the success of similar techniques on graphene is limited due to the chemistry required to keep individual graphene sheets from aggregating in solution.

The technique which currently seems to have the greatest potential for mass production is the direct growth of graphene. Typically this is accomplished by heating a SiC wafer which results in the partial graphitization of the upper layer (Berger, Song et al. 2004). However, controlling the number of layers as well as the grain sizes is difficult with this technique limiting the mobilities achieved so far with this form of graphene (Berger, Song et al. 2006). Furthermore, isolating single sheets is problematic and additional lithography is required to pattern electrostatic gates on top of the graphene. Making suspended mechanical structures from grown graphene has yet to be demonstrated.

Chemical vapor deposition (CVD) and molecular beam epitaxy (MBE) are two other potential routes to graphene growth. Carbon nanotubes and diamond are successfully grown using CVD and the preferred method of growth for high quality GaAs/AlGaAs heterostructures is MBE. For the time being, exfoliation remains the preferred method for most of the experimental research groups around the world. However as in diamond, wide spread applicability of graphene is limited by the crude

and time consuming methods currently used to fabricate and isolate single graphene sheets. The research community is currently in need of a reliable and reproducible graphene fabrication method if graphene is ever to move beyond being a laboratory curiosity.

3.4 Electrical Properties of Graphene

Most of the experimental research on graphene focuses on the electronic properties. The most notable feature about the early work on graphene transistors was the ability to continuously tune the charge carriers from holes to electrons. An example of the gate dependence in single layer graphene is shown in Fig. 3.4a. This effect is most pronounced in the thinnest samples whereas samples from multiple layers show much weaker gate dependence due to screening of the electric field by the other layers.

At low temperatures and high magnetic fields, the exceptional mobility of graphene allows for the observation of the quantum hall effect for both electrons and holes (Fig. 3.4b)(Novoselov, Geim et al. 2005; Zhang, Tan et al. 2005). Due to its unique band structure, the graphene quantum hall effect exhibits a subtle difference from the conventional quantum Hall effect in that plateaus occur at half integers of $4e^2/h$ rather than the typical $4e^2/h$.

For more practical applications one would like to utilize the strong gate dependence of graphene for either sensing or transistor applications. Unfortunately, graphene has no band gap and correspondingly resistivity changes are small. Therefore, a graphene transistor by its very nature is plagued by a low on/off ratio. However one way around this limitation, is to carve graphene into narrow ribbons. By shrinking the ribbon the momentum of charge carriers in the transverse direction becomes quantized which results in the opening of a band gap. This band gap is

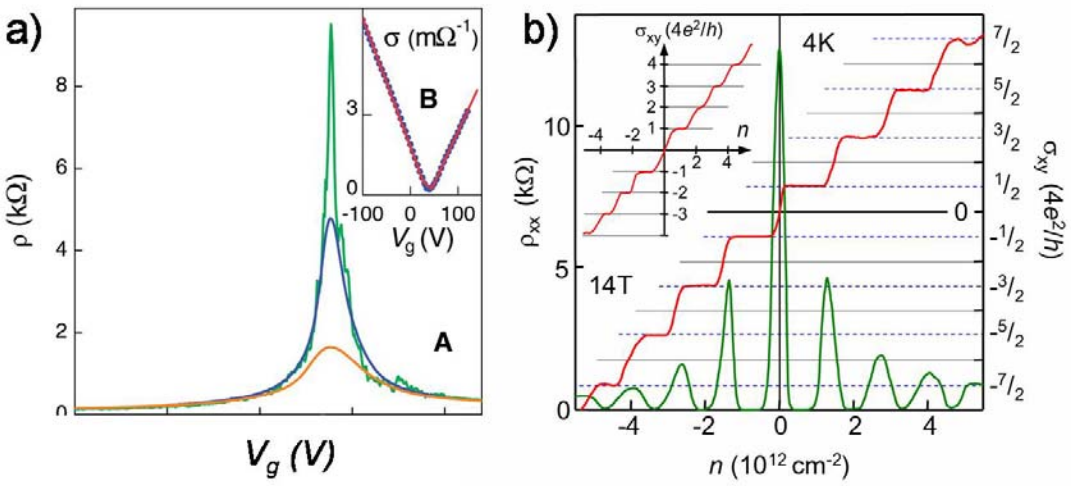

Figure 3.4 a) The resistivity of a single layer of graphene vs. gate voltage. b) The Quantum Hall Effect in single layer graphene. Figures taken from (Novoselov, Geim et al. 2005)

proportional to the width of the ribbon. This effect is pronounced in carbon nanotubes where a nanotube has a band gap proportional to its diameter. The opening of a band gap in graphene ribbons has recently been observed in wide ribbon devices lithographically patterned from large graphene flakes (Han, Ozyilmaz et al. 2007) and in narrow chemically synthesized graphene ribbons (Li, Wang et al. 2008).

3.5 Mechanical Properties of Graphite and Graphene

Graphite is unique in that the elastic constants in the direction perpendicular are vastly different than the elastic constants along the basal plane. This was known for quite some time and was experimentally measured during the 1960s and 1970s. Due to the resurgent interest in graphene and few layer graphene structures, it is worthwhile to revisit this history of graphite. A detailed discussion of the mechanical properties of graphite is given in (Kelly 1981). I will briefly summarize the main conclusions here.

The following set of six equations can be used to describe the stress and strain of a hexagonal lattice such as graphite where the x and y axis are along the basal plane (Kelly 1981).

$$e_{xx} = S_{11}\, T_{xx} + S_{12}\, T_{xy} + S_{13}\, T_{zz}$$

$$e_{yy} = S_{12}\, T_{xx} + S_{11}\, T_{yy} + S_{13}\, T_{zz}$$

$$e_{zz} = S_{13}\, T_{xx} + S_{13}\, T_{yy} + S_{33}\, T_{zz}$$

$$e_{zx} = S_{44}\, T_{zx}$$

$$e_{zy} = S_{44}\, T_{zy}$$

$$e_{xy} = \tfrac{1}{2}(S_{11} - S_{12})T_{xy}$$

where e is the strain, T is the stress, and S is the compliance.

The inverse of these six equations are:

$$T_{xx} = C_{11}\, e_{xx} + C_{12}\, e_{xy} + C_{13}\, e_{zz}$$

$$T_{yy} = C_{12}\, e_{xx} + C_{11}\, e_{yy} + C_{13}\, e_{zz}$$

$$T_{zz} = C_{13}\, e_{xx} + C_{13}\, e_{yy} + C_{33}\, e_{zz}$$

$$T_{zx} = C_{44}\, e_{zx}$$

$$T_{zy} = C_{44}\, e_{zy}$$

$$T_{xy} = \tfrac{1}{2}(C_{11} - C_{12}) e_{xy}$$

where C is the elastic modulus. Both C and S can be experimentally measured using different techniques. Acoustic wave propagation or ultrasonic testing gives C while flexural vibrations and static stress-strain curves are determined by S. It is therefore useful to have equations that relate the two constants. Solving these equations one gets the following relations between S and C:

$$C_{44} = (S_{44})^{-1}$$

$$(C_{11} - C_{12}) = (S_{11} - S_{12})^{-1}$$

$$C_{13}/\mathrm{X} = -S_{13}$$

$$C_{33}/\mathrm{X} = S_{11} + S_{12}$$

$$(C_{11} + C_{12})/\mathrm{X} = S_{33}$$

where $\mathrm{X} = C_{33}\,(C_{11} + C_{12}) - 2\,(C_{13})^2 = [S_{33}\,(S_{11} + S_{12}) - 2\,(S_{13})^2]^{-1}$. The Young's modulus parallel and perpendicular to the basal plane is $1/S_{11}$ and $1/S_{33}$, respectively. The shear modulus parallel to the basal planes is $G = 1/S_{44} = C_{44}$.

The first careful attempts to determine the mechanical elastic constants measured the resonance frequency of cantilevers of natural graphite flakes. Cantilevers with length, L = 0.4 cm – 1.0 cm and thicknesses t = of 0.01 cm – 0.05 cm were cut from natural graphite flakes. For vibrations dominated by shear, the resonance frequency is determined solely by the shear modulus G:

$$f = \frac{1}{4L}\sqrt{\frac{G}{\rho_0}} \qquad (3.1)$$

where ρ_0 is the density while for vibrations dominated by bending, the resonant frequency is dictated by $E = 1/S_{11}$:

$$f = 0.162 \frac{t}{L^2} \sqrt{\frac{E}{\rho_0}} \tag{3.2}$$

By examining the length dependence, Baker and Kelly determined that vibrations in as-received graphite samples were dominated by shear with a modulus, $G = 0.1$ GPa while irradiated crystals were dominated by bending with $E = 0.6$ TPa (Kelly 1981). This value of G is considerably lower than the value determined by specific heat data and attributed to dislocations in the basal plane which reduce the "true" value of G in the nonirradiated samples.

A more thorough study was conducted by a group at Union Carbide (Blakslee, Proctor et al. 1970). Utilizing ultrasonic pulses, sonic resonance, and static test methods the elastic constants were determined to be:

$C_{11} = 1.06 \pm 0.02$ TPa	$S_{11} = 0.98 \pm 0.03$ TPa^{-1}
$C_{12} = 180 \pm 10$ GPa	$S_{12} = -0.16 \pm 0.06$ TPa^{-1}
$C_{13} = 15 \pm 5$ GPa	$S_{13} = -0.33 \pm 0.08$ TPa^{-1}
$C_{33} = 36.5$ GPa	$S_{33} = 2.3 \pm 0.2$ TPa^{-1}
$C_{44} = 0.18 - 0.35$ GPa	
$E = 1/S_{11} = 1.02 \pm 0.03$ TPa	
$C_{12}/C_{11} = 0.17 \pm 0.01$	$-S_{12}/S_{11} = 0.16 \pm 0.06$

The spread in values of C_{44} is due to irradiated and nonirradiated samples exposed to fast neutrons with irradiated samples giving the higher value. This is consistent with what was observed in the above resonance frequency measurements where irradiation increased C_{44} by reducing basal plane dislocations. This higher value is believed to be the "true" value as it also matches specific heat data.

The Poisson's ratio along the basal plane of graphite is defined as $\upsilon = -S_{12}/S_{11}$. The Union Carbide group experimentally measured the ratio $C_{12}/C_{11} = 0.17$. They then used the above expression which relates C and S to assume that C_{12}/C_{11} must be less than or equal to υ. From this, they get a Poisson's ratio along the basal plane of graphite to be $\upsilon = 0.16 \pm 0.06$.

The experimental mechanical properties of graphene are largely unexplored and the time is ripe to revisit some of the old assumptions about bulk graphite to determine how the elastic constants scale down to the atomic thicknesses. By working with single atomic layers or few atomic layers some of the uncertainties involved in working with large single crystals such as dislocations and defects are avoided. Chapter 5 and 6 will present some of the first attempts to measure the mechanical properties of single and few layer graphene.

3.6 Cornell NEMS Band

Cornell has a long tradition of making small musical instruments out of vibrating nanomaterials. The first and probably most well known example is the silicon nanoguitar from Harold Craighead's group in 1997. This was followed by a nanotube guitar from Paul McEuen's group in 2004 (Sazonova, Yaish et al. 2004). This guitar was formed by a vibrating nanotube which has a diameter of ~ 1nm. This pushes the fundamental limits on how small a vibrating guitar string can be made. However, the band has two guitars but no percussion. Imagine Led Zeppelin with no John Bonham, Rush without Neal Peart, Toto less Jeff Porcaro, or Metallica minus Lars Ulrich. For that reason, we created the world's thinnest drum fabricated from graphene - a suspended single layer of atoms – and therefore added a critical piece towards completing the Cornell NEMS band (Fig. 3.5). We leave it to the next generation of Cornell NEMS enthusiast to fabricate a lead vocalist.

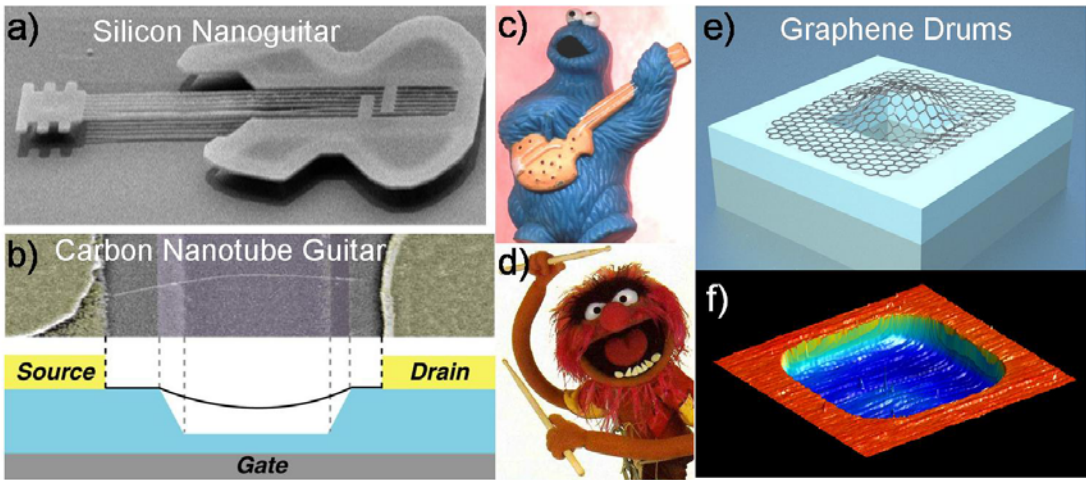

Figure 3.5 a) Silicon nanoguitar from Harold Craighead's group. b) Suspended carbon nanotube guitar (Sazonova, Yaish et al. 2004) c) Cookie Monster playing guitar. Sesame Street. d) Monster muppet playing drums. Image from http://www.wordmagazine.co.uk/. e) Schematic of a graphene drum. f) AFM image of a single layer graphene drum. Images from (Bunch, Verbridge et al. 2008)

CHAPTER 4

COULOMB OSCILLATIONS AND HALL EFFECT IN QUASI-2D GRAPHITE QUANTUM DOTS

4.1 Introduction

One exciting possibility for graphene is the creation of quantum dots: micron scale, nanometer-thick graphene sheets on an insulating substrate with patterned metallic contacts. Quantum dots have previously been made from GaAs heterostructures (Kouwenhoven, Marcus et al. 1997)small metal grains (Ralph, Black et al. 1997), carbon nanotubes (Bockrath, Cobden et al. 1997; Tans, Devoret et al. 1997; Buitelaar, Bachtold et al. 2002), single molecules (Liang, Shores et al. 2002; Park, Pasupathy et al. 2003), and many other materials, but graphite's layered structure and unusual electronic spectrum make it a promising new material for quantum dot studies. Devices with low resistance contacts allow the basic transport parameters of the material to be determined, while those with high contact resistances ($R_c \geq h/2e^2 = 13$ kΩ) are in the Coulomb blockade regime, where the addition and excitation spectrum of electrons is measured. Experiments described in this chapter demonstrate two methods to wire up mesoscopic graphite pieces. Devices with low contact resistances at room temperature ('open dots') maintain their small resistance to low temperatures, and four-probe measurements are made to extract the Hall and longitudinal resistivity of the graphite. Those with high contact resistances at room temperature ('closed dots') show Coulomb blockade oscillations at low temperatures.

4.2 Device Fabrication

The devices are fabricated as follows. Natural graphite flakes (Asbury Carbons Grade 3061) are sonicated in Dichlorobenzene solution for approximately 5 minutes. A drop of the solution is placed onto a degenerately doped Si wafer with a 200 nm thermally grown oxide. The chip is then rinsed with isopropyl alcohol and dried with nitrogen. This leaves a dispersion of graphite pieces ranging in thickness from several hundred nanometers to as small as a few nanometers (See Fig. 4.1). We use two separate methods to wire up the graphite pieces. In the "designed electrode" method, an AFM is employed to locate thin pieces with respect to predefined alignment marks and then electron beam lithography is used to define multiple (two to six) electrodes to the piece (Figure 4.1b). After lithography, 50 nm of Pd is evaporated followed by liftoff. The resulting quasi-2D graphite quantum dots have typical lateral dimensions of approximately 1 μm and vary in thickness from a few to tens of nanometers.

In the "random electrode" method, graphite is dispersed as described above and a series of electrodes with a separation of 1-2 μm are defined by photolithography and evaporating 5 nm of Cr and 50 nm Au (Fig. 4.1d and 4.1e). The resistance of each pair of electrodes is measured to determine if a graphite piece was contacted. It has the advantage of being quick but lacks the control and flexibility of the designed electrode method.

4.3 Device Characterization

The devices were measured at room temperature in a field effect geometry with a bias voltage of 10 mV applied between source and drain electrodes. The back gate voltage V_g was varied from 10 V to -10 V at room temperature. As shown in Fig. 4.2, the two-point resistance of most of the devices was between 2 and 10 kΩ, with a

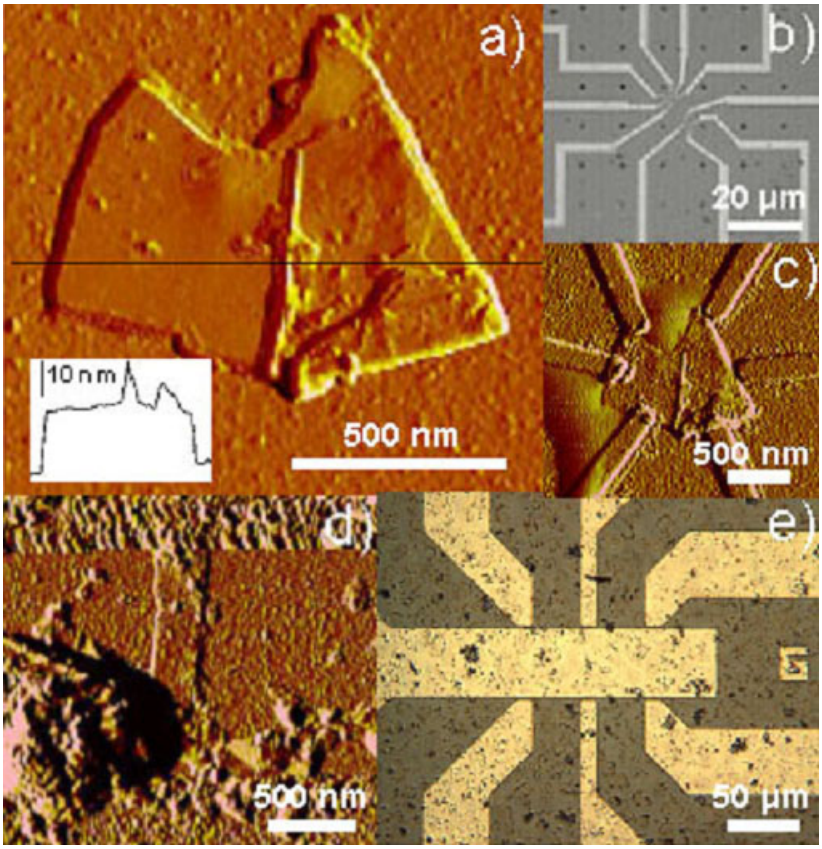

Figure 4.1 (a) AFM image of a graphite piece with a height of 18 nm dispersed onto a SiO_2/Si wafer. (inset) Line trace showing the height. (b) Optical image of electrodes fabricated by electron beam lithography. When a desired graphite piece is located in AFM, its position with respect to the predefined alignment marks visible in the image is determined. Electron beam lithography and liftoff is then used to define the electrodes. (c) AFM image of 6 electrodes defined by electron beam lithography contacting an 18 nm thick graphite dot (designed electrode). (d) AFM image of two electrodes contacting a 5 nm thick graphite dot (random electrode). (e) Optical image of a set of electrodes defined by photolithography over randomly dispersed graphite (random electrode).

few > 100 kΩ. The conductance was relatively independent of V_g, but some samples showed a few percent decrease in the conductance with positive V_g.

Low temperature measurements on the devices were performed at 1.5 K in an Oxford variable temperature insert (VTI) cryostat or 100 mK in an Oxford dilution refrigerator. The devices with low resistances at room temperature (open dots) displayed only a small increase in their resistance upon cooling, as seen in Fig. 4.2. In such devices with multiple contacts, we performed longitudinal and Hall resistance measurements to extract the carrier density, sign of the carriers, and resistivity. Fig. 4.3 shows data from a 5 nm tall dot, corresponding to approximately 15 stacked graphene sheets, measured at ~ 100 mK using standard AC lock-in techniques. Similar results were obtained at 4 K and 1.5 K. The Hall resistance R_{xy} is approximately linear, and the longitudinal resistance R_{xx} shows weak fluctuations as a function of magnetic field with little change in its average value.

4.4 Data Analysis

To analyze these results, we make the simplifying assumption that the entire graphite piece is a uniform conductor with a single density and in-plane mobility. This is appropriate if the electrodes make contact to all the graphene layers and the doping in the crystal is uniform. (Neither of these assumptions has been independently verified). From the standard equation for the Hall resistance $R_H = B/ne$, the slope of the line in Fig. 3 corresponds to a density of 9.2 x 10^{12} cm^{-2}. The sign of the Hall voltage indicates that the dominant charge carriers are holes. A similar measurement on a 2nd device with a height of 18 nm shown in Fig. 1a and 1c gives a hole density of 1.3 x 10^{13} cm^{-2}. Assuming that all sheets are contacted and the charge is relatively uniformly distributed among the sheets, we approximate a density of n_1 = 2 x 10^{11} cm^{-2} for a single graphene sheet in the 18 nm thick device and n_1 = 6 x 10^{11} cm^{-2} for the 5

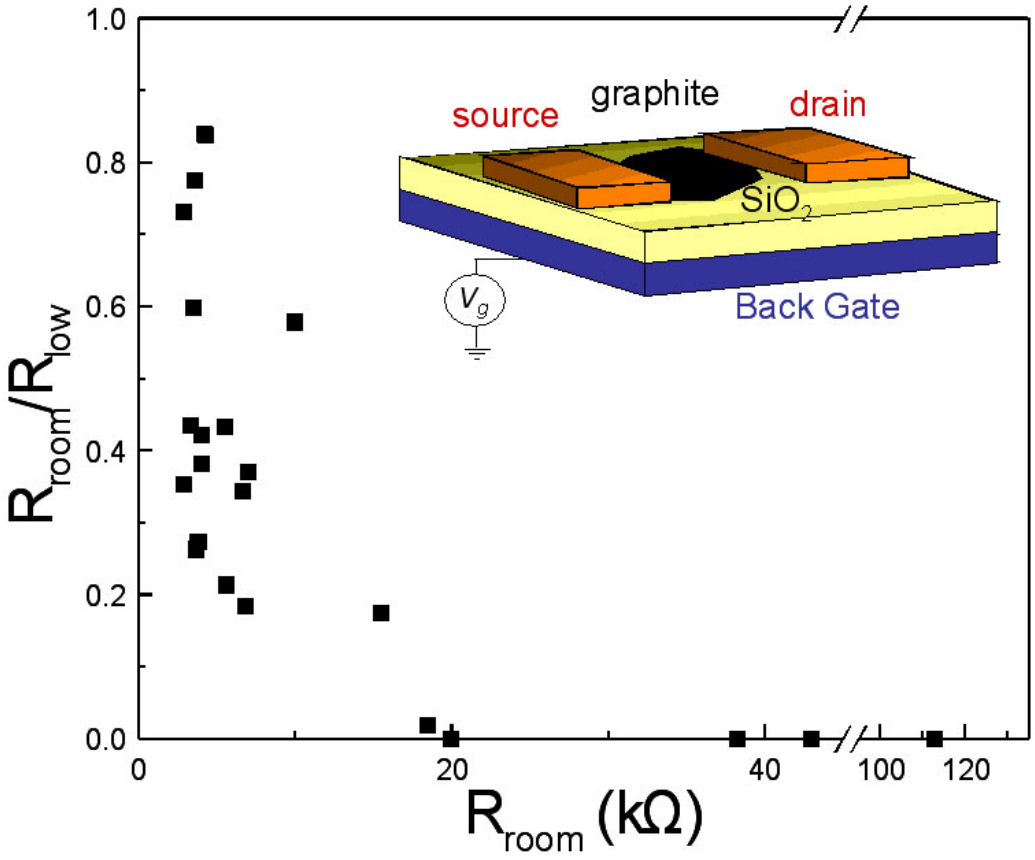

Figure 4.2 A scatter plot of the ratio of the low (T ~ 100 mK) to room temperature 2-point resistance versus the room temperature 2-point resistance for all the devices for which there is low temperature data. (inset) Schematic of the device layout. The graphite is in a field effect transistor geometry with a 200 nm gate oxide. Source and drain electrodes are patterned on top

nm tall device. This density is larger than what has previously been found in bulk graphite samples (Du, Tsai et al.; Soule 1958; Tokumoto, Jobiliong et al. 2004) and indicates a significant amount of hole doping in this device. The origin of this doping is unknown.

After accounting for the geometrical factors, we infer the resistance per square, $R_{\square}$, of the entire sample and the resistance per square of a single graphene layer, $R_{1\square}$. For the 5 nm thick device at 100 mK, we have $R_{\square}$ = 3.4 kΩ and $R_{1\square}$ = 51 kΩ. Using the equation $\mu = 1/neR_{\square}$, we get a mobility of μ = 200 cm^2/V-s. A similar analysis for the sample with a thickness of 18 nm shown in Fig. 1a and 1c at 1.5 K yields $R_{\square}$ = 260 Ω, $R_{1\square}$ = 14 kΩ, and μ = 1900 cm^2/V-s. The inferred mobilities are significantly lower than in bulk purified natural graphite flakes, which range from 1.5-130 x 10^4 cm^2/V-s (Soule 1958).

We can use a gate to vary the carrier density in the graphite quantum dot. We assume the capacitance to the gate is that of a parallel plate capacitor; $C_g = \varepsilon_o \varepsilon A/d$, where d = 200 nm is the thickness of the SiO_2, ε_o is the permittivity of free space, ε is the dielectric constant of SiO_2, and A is the area of the device. This gives a capacitance per area of C'_g = 1.8 x 10^{-8} F/cm^2 implying that 10 V applied to the back gate results in a change of density of 1 x 10^{12} holes/cm^2. This is only a small fraction of the total density in even the thinnest samples studied. Nevertheless, it is consistent with a small decrease in conductance observed in many samples at room temperature; the holes are slightly depleted by the gate. At low temperatures, any such changes are obscured by reproducible fluctuations in the conductance as a function of V_g.

4.5 Coulomb Blockade

Devices with room temperature 2-point resistances greater than 20 kΩ (closed dots) show Coulomb blockade at low temperatures. Data from a device fabricated

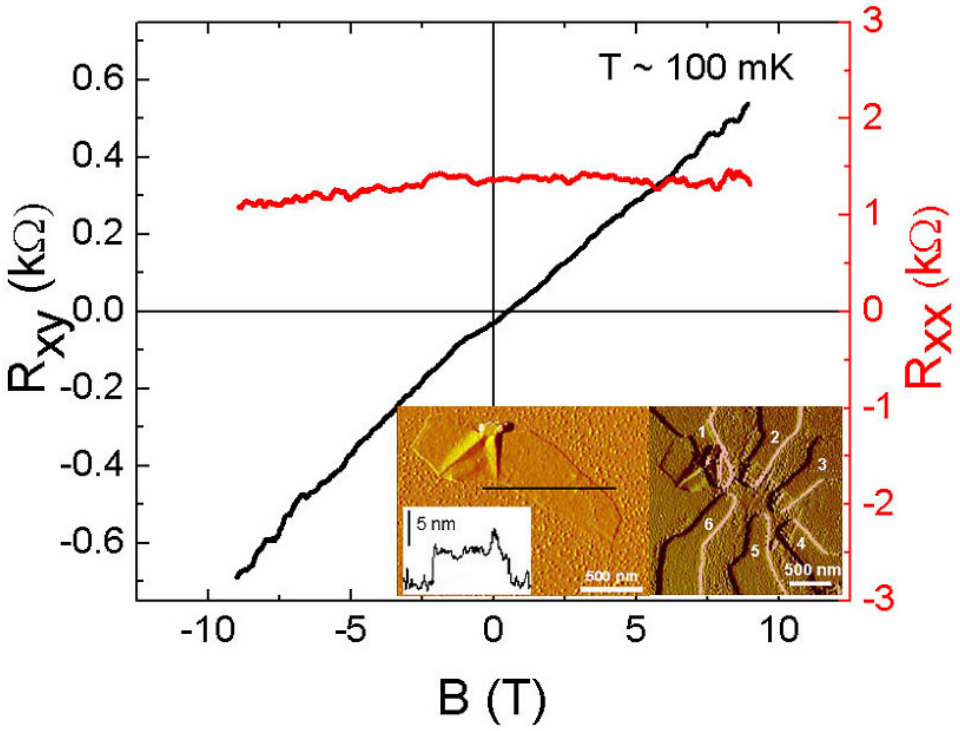

Figure 4.3 Longitudinal and Hall resistance measured as a function of magnetic field at 100 mK for the 5 nm thick graphite dot shown in the insets. The Hall resistance, R_{xy}, was determined using standard lock-in techniques by applying a 43 nA excitation current between electrodes 2 and 6 and measuring the voltage drop between electrodes 1 and 4. The longitudinal resistance, R_{xx}, was determined by measuring the voltage drop between electrodes 5 and 6 while an excitation current of 10 nA was passed between electrodes 1 and 4. The slope of R_{xy} versus B (black line) corresponds to a total density of 9.2 x 10^{12} cm^{-2}. The longitudinal resistance (red line) shows only weak fluctuations as a function of B. (inset a) AFM image of a graphite piece with a height of 5 nm and its corresponding line trace. (inset b) The graphite piece shown in inset (a) with electrodes patterned on top using the designed electrode method.

using the random electrode method is shown in Fig. 4.4. At T = 100 mK, the conductance exhibits well defined Coulomb blockade oscillations with a period in gate voltage of ΔV_g = 1.5 mV. A plot of dI/dV_{sd} *vs* V_g and V_{sd} is shown in Fig. 4.4. The maximum voltage that could be applied and still be in the blockade regime is ΔV_{sd} = 0.06 mV.

A device made by the designed electrode method is shown in Fig. 4.5. The thickness of the device is 6 nm, corresponding to 18 sheets. The Coulomb blockade oscillations have a period of ΔV_g = 11 mV and a maximum blockade voltage of ΔV_{sd} = 0.3 mV. A third device fabricated by the random electrode method shown in Fig. 4.1d has a height of 5 nm and shows Coulomb oscillations with a period in gate voltage of ΔV_g = 1.3 mV.

To describe these results, we use the semiclassical theory of the Coulomb blockade (Beenakker 1991). The period of the Coulomb oscillations in gate voltage is given by: $\Delta V_g = e/C_g$, and using the previous expression for C_g, we can approximate the area of the graphite quantum dot. For the device in Fig. 4.5 with ΔV_g = 11 mV, the expected area of dot is A = 0.08 μm^2. The measured total area of the graphite piece shown is 0.12 μm^2 while the area between the electrodes is 0.05 μm^2. This demonstrates that nearly the entire graphite piece is serving as a single quantum dot and it likely extends beyond the electrodes. For the device shown in Fig. 1d, the measured gate voltage period is ΔV_g = 1.3 mV which corresponds to a quantum dot with A = 0.70 μm^2. The area between the electrodes is 0.45 μm^2 again implying that the dot extends into the graphite piece lying under the electrodes.

The charging energy for the dot is determined by its total capacitance C and is equal to the maximum blockade voltage observed: $e/C = \Delta V_{sd}$. Notably, for our graphite quantum dots, the ratio of the charging energy to the gate voltage period is small: α =

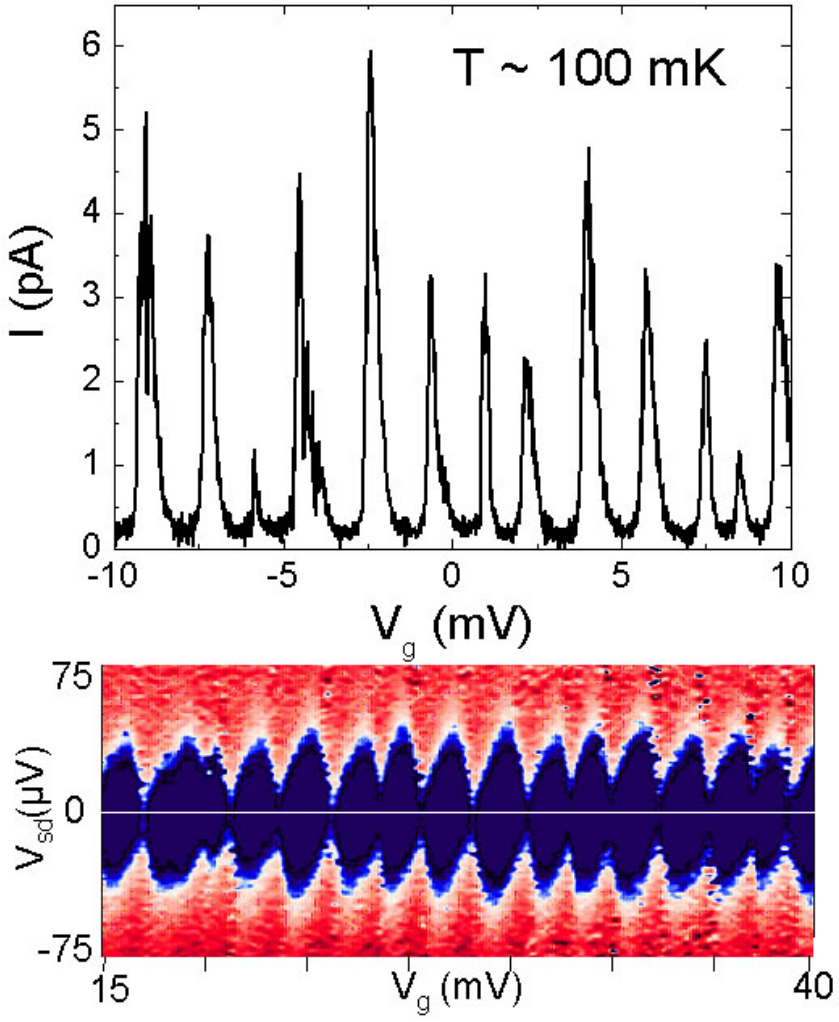

Figure 4.4 (a) Current as a function of gate voltage with V_{sd} = 10 μV at T ~ 100 mK for a device fabricated by the random electrode method. Coulomb oscillations are observed with a period in gate voltage of ΔV_g = 1.5 mV. (b) The differential conductance dI/dV_{sd} plotted as a color scale versus V_{sd} and V_g. Blue signifies low conductance and red high conductance. The charging energy of the quantum dot is equal to the maximum height of the diamonds: ΔV_{sd} = 0.06 mV. The center-to-center spacing between the diamonds is the Coulomb oscillation period ΔV_g = 1.5 mV.

$(e/C)/\Delta V_g = C_g/(C_s + C_d + C_g) << 1$, where C_s and C_d are the capacitances to the source and drain electrodes. The devices shown in Fig. 4.4 and Fig. 4.5 have $\alpha = 1/25$ and 1/40 respectively. Such small values imply that the graphite pieces have a much greater capacitive coupling to the source and drain electrodes than to the gate.

We can estimate the source and drain capacitance per unit area $C_{s,d}'$ using the measured charging energies and the area of the electrodes over the graphite. For the device shown in Fig. 4.5, this yields a capacitance per unit area of $C_{s,d}' = 2 \times 10^{-6}$ F/cm^2. Using the parallel plate capacitor equation, $C_{s,d}' = \varepsilon_o \varepsilon_r / d$ yields $d/\varepsilon_r = 0.5$ nm. This is consistent with a very thin tunnel barrier between the electrode and the graphite. The origin and nature of this barrier is unknown. Since it is only present in the few samples that show Coulomb blockade oscillations (closed dots), it is likely the result of a contamination layer between the metal and the graphite.

4.6 Magnetic Field Dependence

We also examined the magnetic field dependence of the Coulomb blockade oscillations (Fig. 4.5). The closed dot at B = 0 T has well defined oscillations. As the magnetic field is increased, the peaks evolve in a complicated fashion. Most notably, the oscillations no longer go to zero suggesting that the dot becomes more open. The open dot shows complex fluctuations in the peak positions as a function of magnetic field. Other devices showed similar transitions from closed to more open dots along with changes in the peak positions as a function of field. The origin of these effects is currently unknown.

4.7 Conclusions

In conclusion, we fabricated and measured quasi 2-D graphite quantum dots. In devices with good contacts (open dots), we performed resistivity measurements and

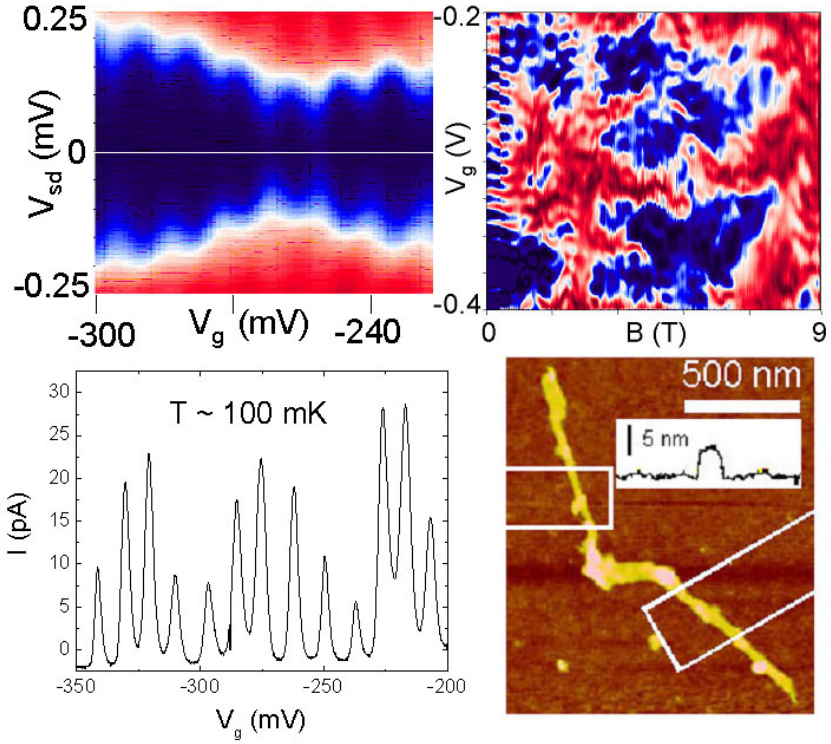

Figure 4.5 (a) The differential conductance dI/dV_{sd} plotted as a color scale versus V_{sd} and V_g for the device shown in (d) at T ~ 100 mK. The charging energy is ΔV_{sd} = 0.3 mV and the gate voltage period is ΔV_g = 11 mV. (b) Current as a function of gate voltage with V_{sd} = 10 μV at T ~ 100 mK for the device shown in (d). Coulomb blockade oscillations are seen with a period of ΔV_g = 11 mV. (c) Current as a function of gate voltage versus magnetic field with V_{sd} = 10 μV at T ~ 100 mK for the device shown in (d). (d) AFM image of a device fabricated using the designed electrode method. The white rectangular outlines show the position and size of the electrodes that were evaporated on the device. The total area of the graphite piece is 0.12 μm^2 and the area under the source and drain electrodes is 0.013 μm^2 and 0.015 μm^2, respectively. The area of the graphite piece between the source and drain electrodes is 0.05 μm^2. (inset) Line trace showing the 6 nm height of the graphite.

extracted carrier densities of 2-6 x 10^{11} holes per sheet and mobilities of 200-1900 cm^2/V-s. In the case of tunnel contacts (closed dots), we observed Coulomb charging phenomena and inferred the gate and source-drain capacitances. Future studies can investigate the nature and role of interlayer coupling between the sheets, explore the single particle energy level spectrum, and the effects of a magnetic field. Studies on devices with a variety of thicknesses and improved control over the contacts will help address these issues. It should be noted that graphene's massless band dispersion relation results in a different density of states which gives $\Delta E \sim v_f h/2D$ for a square dot of length D where $v_f \sim 10^6$ m/s is the Fermi velocity (Ponomarenko, Schedin et al. 2008). For example, the quantum dot in Fig. 4.5 has $D \sim 200$ nm which gives $\Delta E \sim 10$ meV. This is about 30x the charging energy. Recent work by Andre Geim's group explored this regime for graphene quantum dots with $D < 100$ nm fabricated from single layers of graphene (Ponomarenko, Schedin et al. 2008).

CHAPTER 5

ELECTROMECHANICAL RESONATORS FROM GRAPHENE SHEETS

5.1 Introduction

The miniaturization of electromechanical devices promises to be revolutionary in the coming decades as the miniaturization of electronic devices was in the previous ones. Devices ranging from nanoscale resonators, switches, and valves have applications in tasks as diverse as information processing, molecular manipulation, and sensing. The prototypical nanoelectromechanical system (NEMS) is a nanoscale resonator, a beam of material that vibrates in response to an applied external force (Craighead 2000; Ekinci and Roukes 2005). The ultimate limit would be a resonator one atom thick, but this puts severe constraints on the material. It should be robust, stiff, and stable as a single layer of atoms.

Graphite consists of stacked layers of graphene sheets separated by 0.3 nm and held together by weak van der Waals forces (Kelly 1981). It has extremely high strength, stiffness, and thermal conductivity along the basal plane. In addition, graphite can be exfoliated onto an insulating substrate, producing micron-sized graphene sheets with thicknesses down to a single atomic layer (Bunch, Yaish et al. 2005; Novoselov, Geim et al. 2005; Novoselov, Jiang et al. 2005; Zhang, Tan et al. 2005; Wilson 2006). Thus far, research on these thin graphene sheets has focused primarily on their electronic properties. We demonstrate a method of suspending single and multilayer graphene sheets over trenches and show such sheets can be mechanically actuated. This work also makes a detailed study of the mechanical properties of these graphene resonators including resonance frequency, spring constant, built in tension, and quality factor.

5.2 Device Fabrication

Suspended graphene sheets are fabricated using a peeling process similar to that reported previously in which a freshly cleaved piece of Kish graphite (Toshiba Ceramics) is rubbed onto a silicon wafer with 260 - 330 nm (280 nm ideal) of thermally grown SiO_2. (Novoselov, Geim et al. 2005; Novoselov, Jiang et al. 2005; Zhang, Tan et al. 2005). In our case, the graphene sheets are mechanically exfoliated over predefined trenches etched into a silicon oxide surface (Fig. 5.1). Trenches with a depth of 260 - 500 nm and widths and lengths of 0.5 – 10 μm are defined on the SiO_2 by dry RF plasma etching. Electrodes are defined by photolithography and consist of 5 nm of Cr and 30 nm Au. The graphene sheets peel off on the edges of the large trenches and electrodes and are suspended over nearby small trenches. The result is a micron-scale doubly clamped beam or cantilever clamped to the silicon oxide surface via van der Waals attraction (Fig. 5.1A, 5.1D).

5.3 Device Characterization – AFM and Raman

A non-contact mode AFM was used to quantitatively measure the thickness of the sheets on the substrate next to the trench, as shown in the inset in Fig. 5.1D. All non-contact mode AFM images are taken using a Dimension 3100 operating in ambient conditions using silicon cantilevers with resonance frequencies of 250 – 350 kHz.

However, for sheets thinner than 2-3 nm, such measurements are unreliable for determining the actual thickness (Ferrari, Meyer et al. 2006; Gupta, Chen et al. 2006; Graf, Molitor et al. 2007). For these we used spatially resolved Raman spectroscopy to determine the number of layers (Fig. 1E) (Ferrari, Meyer et al. 2006; Gupta, Chen et al. 2006; Graf, Molitor et al. 2007). Using a Renishaw InVia Raman microscope, light

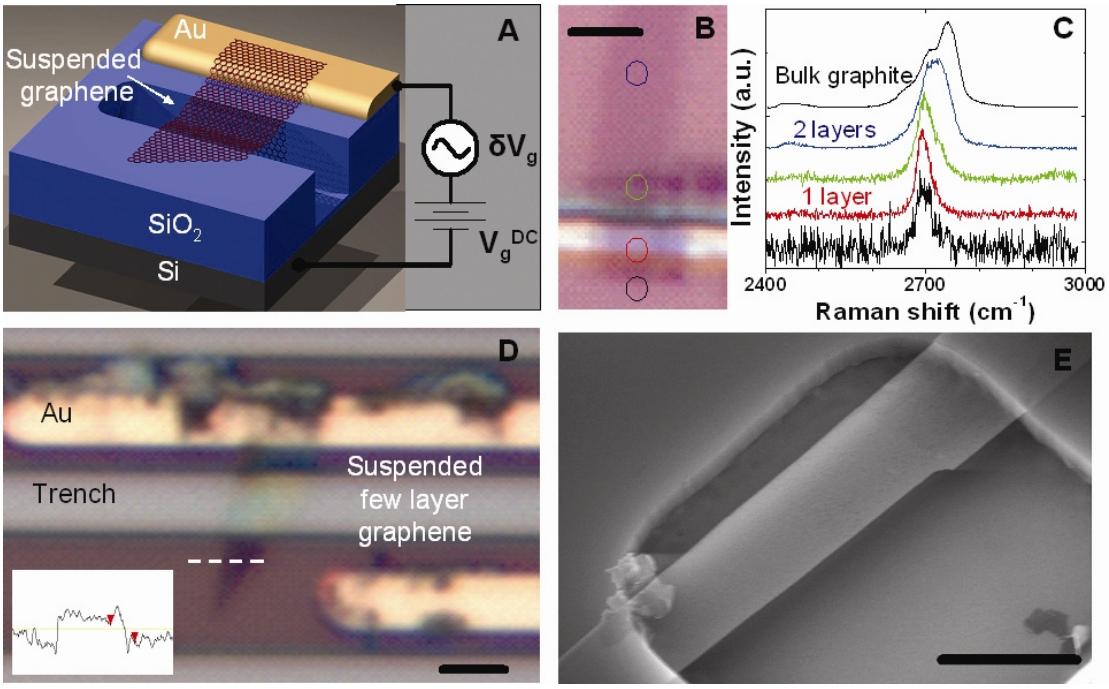

Figure 5.1 (A) Schematic of a suspended graphene resonator. (B) An optical image of a double layer graphene sheet that becomes a single suspended layer over the trench. Scale bar = 2 μm. Each colored circle corresponds to a point where a Raman spectrum was measured. (C) Raman signal from a scan on the graphene piece. Each colored scan is data taken at each of the matching colored circles. The top scan is used as a reference and corresponds to the Raman shift of bulk graphite. (D) An optical image of few (~ 4) layer graphene suspended over a trench and contacting a gold electrode. Scale bar = 1 μm (inset). A line scan from tapping mode AFM corresponding to the dashed line in the optical image. It shows a step height of 1.5 nm. (E) A scanning electron microcope image of a few (~ 2) layer graphene resonator. Scale bar = 1 μm.

with a wavelength of 488 nm is focused on the resonator using a 50x objective and each Raman trace is taken with a 1 - 5 second integration time. The sample sits on a piezoelectric stage which is scanned to take a Raman spectrum at specific points along the graphene sheet. The graphene sheet in Fig. 5.1B has an AFM-determined height of 0.9 nm. By comparison with previous results (Ferrari, Meyer et al. 2006; Gupta, Chen et al. 2006; Graf, Molitor et al. 2007), the shape of the Raman peak near 2700 cm^{-1} suggests the sheet is two layers thick over the area lying on the SiO_2 substrate (Fig. 5.1E), while the section suspended over the trench is a single graphene layer.

5.4 Resonance Measurements

All resonator measurements are performed at room temperature and a pressure of $< 10^{-6}$ torr unless otherwise indicated. The resonators are actuated using either electrical (Fig. 5.1A) or optical modulation (Fig. 5.2). In the case of electrical modulation, a time-varying radio frequency (RF) voltage δV_g at frequency f is superimposed on top of a constant voltage and applied to the graphene sheet. This is accomplished by combining a time varying RF voltage from the RF output of an Agilent E4402B Spectrum Analyzer and a DC voltage from a Yukogawa 7651 DC source. The result is an electrostatic force between the suspended graphite sheet and the substrate:

$$F_{el} \approx \frac{1}{2} C_g^{'} \left(V_g^{DC} \right)^2 + C_g^{'} V_g^{DC} \delta V_g \qquad (5.1)$$

where C_g' is the derivative of the gate capacitance with respect to the distance to the gate, and V_g^{DC} and δV_g are, respectively, the DC and time varying RF voltages applied to the gate (Sazonova, Yaish et al. 2004). For optical actuation, the intensity of a diode laser focused on the sheet is modulated at frequency, f, causing a periodic

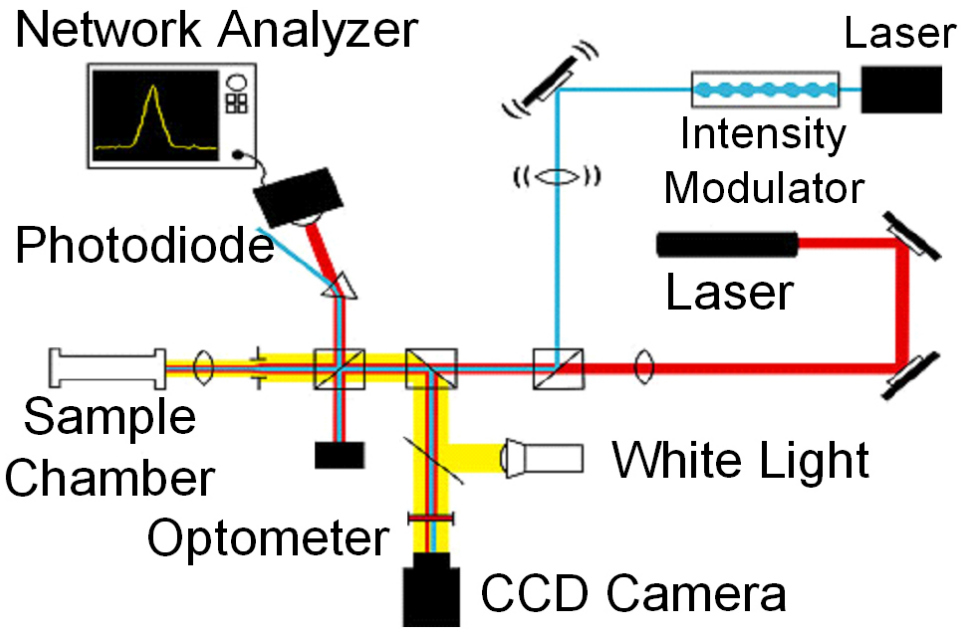

Figure 5.2 Schematic of the experimental setup used to actuate and detect vibrations. (Adapted from Rob Reichenbach)

contraction/expansion of the layer that leads to motion. A 432 nm diode laser whose intensity is modulated at a frequency defined by the network analyzer is used (Fig. 5.2). In both cases, the motion is detected by monitoring the reflected light intensity from a second laser using a fast photodiode. The suspended graphene sheet and the silicon back plane form an interferometer through which vibrations are detected by looking at variations in the intensity of the reflected light from a second 632.8 nm He-Ne laser focused on the resonators (Ilic, Krylov et al. 2005).

5.5 Resonance Spectrum

Figure 5.3A shows the measured amplitude versus frequency for a 15 nm thick sheet suspended over a 5 μm trench. Multiple resonances are observed, the most prominent one at the lowest frequency. We associate this dominant peak with the fundamental vibrational mode; its detected intensity is largest as the motion is in-phase across the entire suspended section. We will limit our discussion primarily to this fundamental mode. A fit to a Lorentzian yields a resonance frequency f_o = 42 MHz and a quality factor Q = 210. Figure 5.3B shows similar results for the single layer graphene resonator from Fig. 5.1B; f_o = 70.5 MHz and Q = 78. Figure 5.4 shows the results of measurements of 33 resonators with thicknesses varying from a single atomic layer to sheets 75 nm thick. The frequencies f_o of the fundamental modes vary from 1 MHz to 166 MHz with quality factors, Q of 20 – 850.

For mechanical resonators under tension T, the fundamental resonance mode f_0 is given by:

$$f_0 = \sqrt{\left(A\sqrt{\frac{E}{\rho}}\frac{t}{L^2} \right)^2 + \frac{0.57A^2S}{\rho L^2 t}} \qquad (5.2)$$

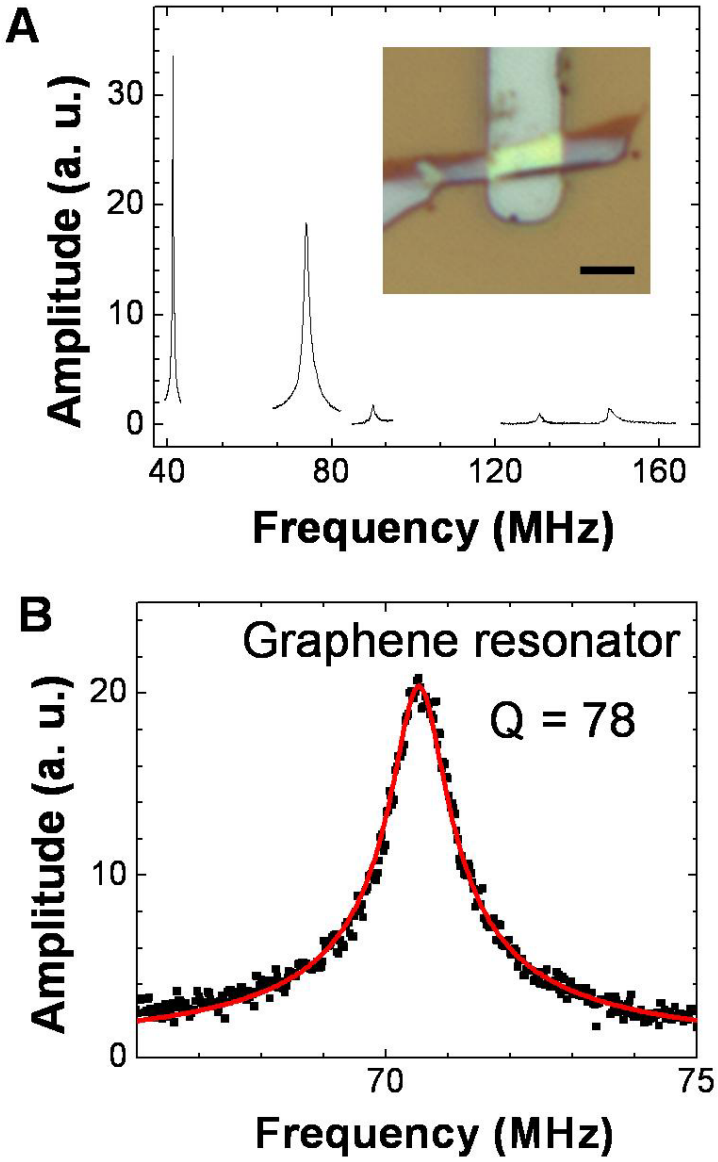

Figure 5.3 (A) Amplitude versus frequency for a 15 nm thick multilayer graphene resonator taken with optical drive. (inset) An optical image of the resonator. Scale bar = 5 μm (B) Amplitude versus frequency taken with optical drive for the fundamental mode of the single layer graphene resonator shown in Fig. 5.1(B). A Lorentzian fit of the data is shown in red.

where E is the Young's modulus, S is the tension per width, ρ is the mass density, t and L, are the thickness and length of the suspended graphene sheet, and A = 1.03 for doubly-clamped beams and 0.162 for cantilevers (Timoshenko, Young et al. 1974). In the limit of small tension, Eq. 5.2 predicts that the resonance frequency f_o scales as t/L^2. Figure 5.4 shows the resonance frequency of the fundamental mode for resonators with t > 7 nm as a function of t/L^2 plotted as solid squares. Also plotted is the theoretical prediction, Eq. 5.2, in the limit of zero tension, for both cantilevers and beams, where we have used the known values for bulk graphite ρ = 2200 kg/m^3 and E = 1.0 TPa (Kelly 1981). This is a valid comparison considering the extensive theoretical and experimental work which shows the basal plane of graphite to have a similar value for E as graphene and carbon nanotubes (Kelly 1981; Qian, Wagner et al. 2002). To account for possible errors in E, we plot dashed lines which correspond to values of E = 0.5 TPa and 2 TPa. The data follow the predictions reasonably accurately, indicating that thicker resonators are in the bending-dominated limit with a modulus E characteristic of the bulk material. This is among the highest modulus resonator to date, greater than 53 – 170 GPa in 12 – 300 nm thick Si cantilevers and similar to single walled carbon nanotubes and diamond NEMS (Sekaric, Parpia et al. 2002; Li, Ono et al. 2003; Sazonova, Yaish et al. 2004). In contrast to ultra thin Si cantilevers, the graphene resonators show no degradation in Young's modulus with decreasing thickness (Li, Ono et al. 2003).

The resonance frequency versus t/L^2 for the resonators with t < 7 nm are shown as hollow squares in Fig. 5.4. The frequencies of these thinner resonators show more scatter with the majority having resonance frequencies significantly higher than predicted by bending alone. A likely explanation for this is that many of the resonators are under tension, which increases f_o.

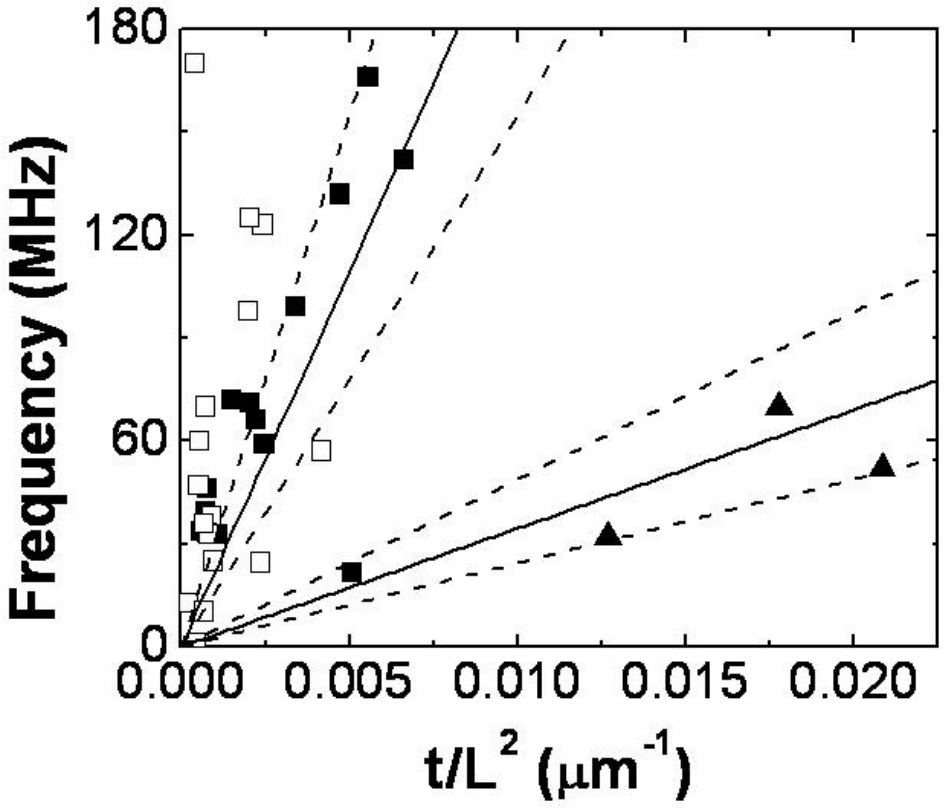

Figure 5.4 (A) A plot showing the frequency of the fundamental mode of all the doubly clamped beams and cantilevers versus t/L^2. The cantilevers are shown as solid triangles (▲). The doubly clamped beams with $t > 7$ nm are shown as solid squares (■) while doubly clamped beams with $t < 7$ nm are shown as hollow squares (□). All thicknesses determined by AFM. The solid line is the theoretical prediction with no tension and $E = 1$ TPa. The dashed lines correspond to $E = 0.5$ TPa and *2* TPa.

5.6 Tension

The single layer graphene resonator shown in Fig. 5.1B illustrates the importance of tension in the thinnest resonators. It has a fundamental frequency f_o = 70.5 MHz, much higher than the 5.4 MHz frequency expected for a tension-free beam with t = 0.3 nm, L = 1.1 μm, and w=1.93 μm. From Eq. 1, this implies that the graphene resonator has a built in tension of Sw = 13 nN. Using the expression $\Delta L/L = Sw/(EA)$, this corresponds to a strain of 2.2 x 10^{-3} %.

The tension in resonators with t < 7 nm was inferred to be 10^{-8} to 10^{-6} N. This is reasonable considering the large van der Waals attraction between the graphene and silicon oxide. Our group has strained carbon nanotubes lying on an oxide surface up to 2 percent, and the van der Waals force remains sufficient to hold the nanotube in place. The Lieber and Park group at Harvard have reported that the van der Waals force is sufficiently strong to hold strains as high as 10 percent for a nanotube on oxide (Bozovic, Bockrath et al. 2003).

So far we are unable to control the initial tension for the resonator. The tension could result from the fabrication process, where the friction between the graphite and the oxide surface during mechanical exfoliation stretches the graphene sheets across the trench. Another possibility is a self tensioning mechanism due to strong van der Waals' interaction between the graphene and the sidewalls of the trench. This is investigated in more detail in Chapter 6.

5.7 Young's Modulus

The Young's modulus remains a useful concept for atomic scale devices provided the right effective thickness is used (Qian, Wagner et al. 2002). There is extensive theoretical work on the mechanical properties of carbon nanotubes which are rolled up graphene sheets, and a Young's modulus for these nanostructures is

commonly used. However, there is a significant variation in the literature of both the accepted and measured values of the Young's modulus (Qian, Wagner et al. 2002). Determining inferred tension from the Young's modulus is misleading for thick resonators, because any error in the Young's modulus results in a large error in the inferred tension. However, it still is accurate to deduce the tension in the thinner resonators since many of these are in a high tension limit.

5.8 Tuning the Resonance Frequency

Data for electrical drive on resonance for the 1.5 nm thick graphene sheet in Fig. 5.1D are shown in Fig. 5.3. The amplitude and frequency of the fundamental mode as well as the higher mode increase linearly with V_g^{DC} at a fixed δV_g as expected from equation (5.1) (Fig. 5.3 C). Also shown is a plot of the resonance frequency vs. V_g^{DC} at a fixed δV_g for both modes (Fig. 5.3 D). In this case, the higher mode increases in frequency with V_g^{DC} while the fundamental mode is unchanged. Most of the modes measured in different resonators exhibited either no tuning or positive tuning in which the frequency increased with V_g^{DC}. A few of the resonators displayed negative tuning where the frequency decreased with increasing V_g^{DC}. The fundamental mode for the resonator in Fig. 5.8 displayed such negative tuning (Fig. 5.6 B). Resonators with frequencies lower than expected (presumably with slack) such as the one in Fig 5.8, decrease in frequency with capacitive force. Resonators with tension (the majority) either show no tuning or an increase in frequency with capacitive force. The different kinds of tuning have previously been observed in other NEMS devices and attributed to spring constant softening due to the electrostatic attraction to the gate, increasing tension from stretching, and a transition from bending to catenary regime (Sazonova, Yaish et al. 2004; Kozinsky, Postma et al. 2006).

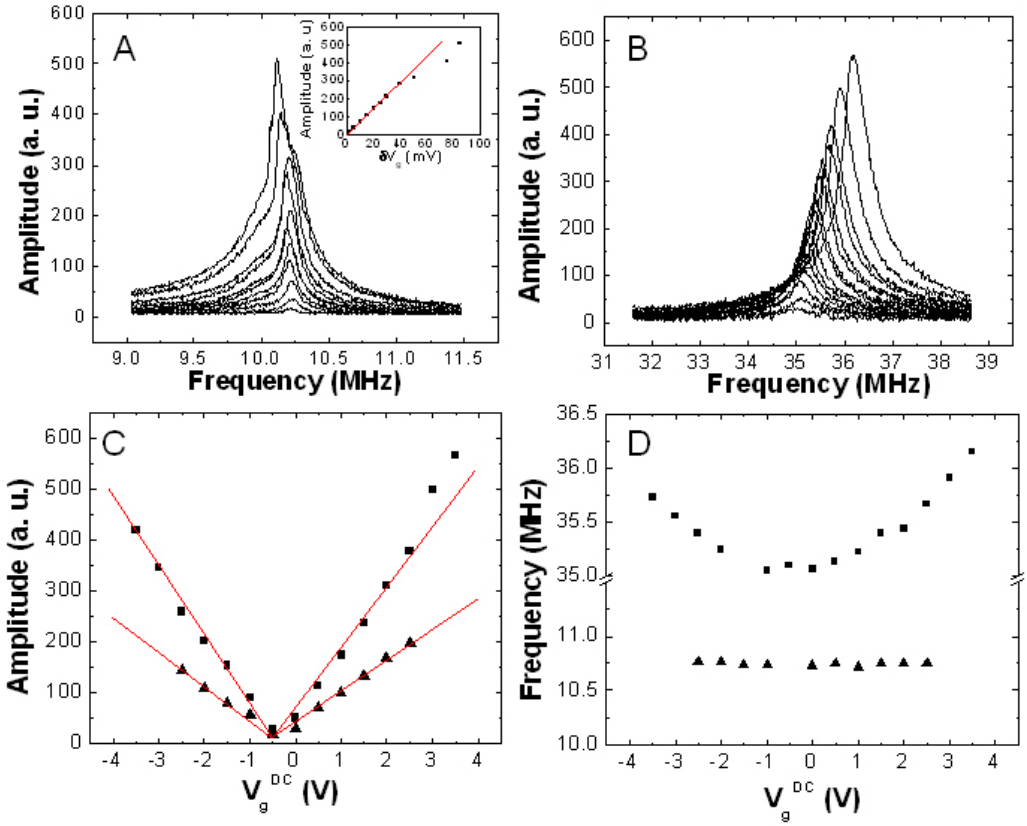

Figure 5.5 (A) Amplitude versus frequency for the fundamental mode from the resonator shown in Figure 1(D) taken using electrical drive with $V_g^{DC} = 2$ V and increasing δV_g. (inset) The amplitude on resonance as a function of δV_g. (B) Amplitude versus frequency of a higher mode from the resonator shown in Figure 1(B) taken using electrical drive with $\delta V_g = 15$ mV and increasing V_g^{DC}. (C) Amplitude of oscillation versus V_g^{DC} at $\delta V_g = 15$ mV for both the 10 MHz mode (▲) and 35 MHz mode (■). (D) Frequency versus V_g^{DC} at $\delta V_g =$ 15 mV for both the 10 MHz mode (▲) and 35 MHz mode (■).

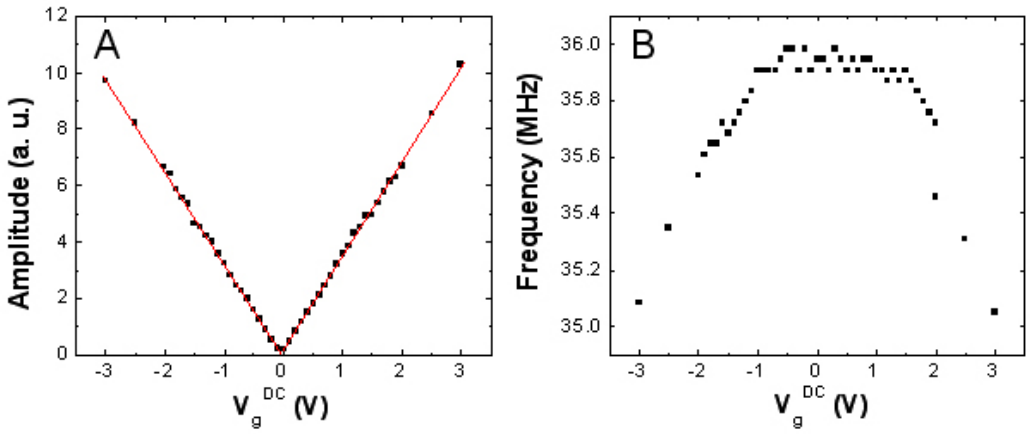

Figure 5.6 (A) Amplitude of oscillation versus V_g^{DC} at δV_g = 50 mV for the fundamental mode shown in Fig. 5.8A. (B) The frequency at maximum amplitude versus V_g^{DC} at δV_g = 50 mV for the fundamental mode shown in Fig. 5.8A.

5.9 Quality Factor

An important measure of any resonator is the normalized width of the resonance peak characterized by the quality factor $Q = f_0/\Delta f$. A high Q is essential for most applications, as it increases the sensitivity of the resonator to external perturbation. A plot of the Q versus the thickness for all the graphene resonators (Fig. 5.7) shows that there is no clear dependence of Q on thickness. This contrasts with results on thicker NEMS resonators fabricated from silicon (Yasumura, Stowe et al. 2000). The quality factors at room temperature are lower than diamond NEMS (2500 – 3000) of similar volume and significantly lower than high stress Si_3N_4 nanostrings (200,000), yet similar to those reported in single walled carbon nanotubes (50-100) (Sekaric, Parpia et al. 2002; Sazonova, Yaish et al. 2004; Verbridge, Parpia et al. 2006). Preliminary studies on a 20 nm thick resonator found a dramatic increase in Q with decreasing temperature (Q = 100 at 300 K to Q = 1800 at 50 K). This suggests that high Q operation of graphene resonators should be possible at low temperatures.

There was no striking dependence of Q on thickness, frequency, or mode number in our graphene resonators. Upon cooling, the Q increased for most of the devices, but this was accompanied by noise in the frequency position of the resonance frequency peak, making a systematic study difficult.

No clear dependence of quality factor on resonator thickness was observed. This suggests that the dominant dissipation mechanism is different than that of standard silicon NEMS. Since the structure and quality factor of graphene resonators is similar to carbon nanotube resonators, it is possible that the dissipation mechanism is similar. However, there is currently no clear understanding of the dissipation mechanism in carbon nanotube resonators. An extrinsic mechanism such as clamping loss or fluctuating charge noise may dominate dissipation in graphene resonators.

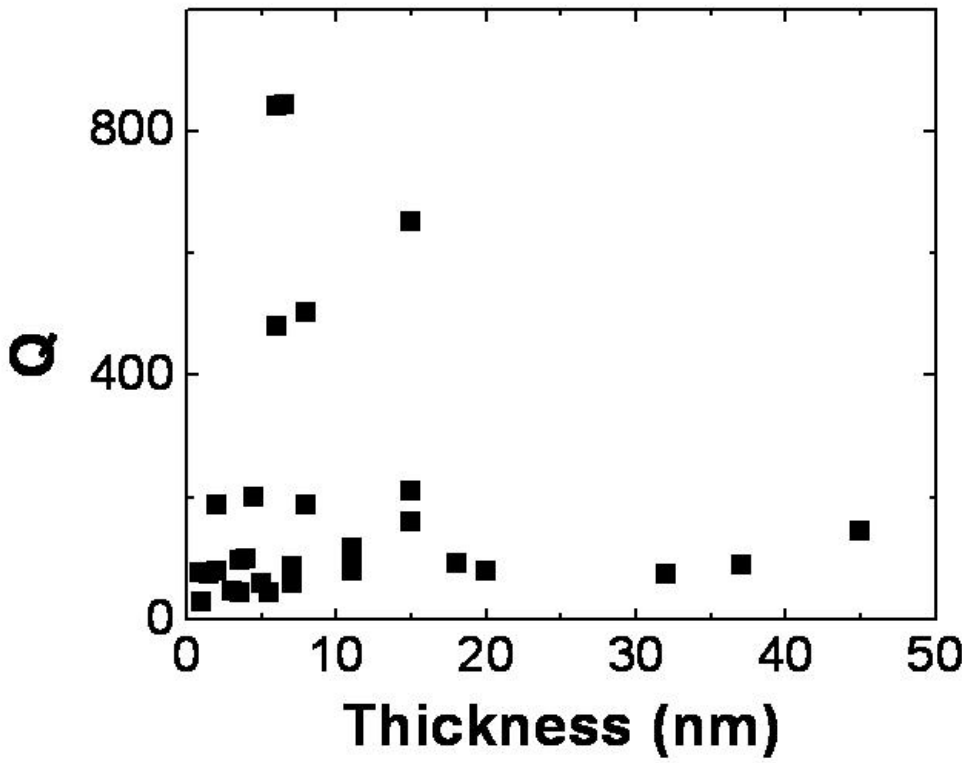

Figure 5.7 The quality factor of the fundamental mode vs. thickness for all resonators measured.

5.10 Vibration Amplitude

Even when a resonator is not being driven, it will still vibrate due to thermal excitation by an rms amount $x_{th} = [k_B T/\kappa_{eff}]^{1/2}$, where $\kappa_{eff} = m_{eff}\omega_0^2 = 0.735Lwt\rho\omega_0^2$ is the effective spring constant of the mode (Ekinci and Roukes 2005). An example is shown in Fig. 5.8A, where a 5 nm thick resonator with f_0 = 35.8 MHz and κ_{eff} = 0.7 N/m has a room temperature thermal rms motion of x_{th} = 76 pm. For resonators where the thermal vibrations could be measured, we use this thermal rms motion to scale the measured photodetector voltage with resonator displacement. To detect thermal vibrations, both large thermal amplitude (low spring constant) and large reflectivity (high optical signal) from the graphene is required. This was only the case for a few of the resonators studied.

Figure 5.8B shows such a rescaled plot of the displacement amplitude versus RF drive voltage. The resonator is linear up to displacements of 6 nm, or on the order of its thickness, where nonlinearities associated with additional tension are known to set in (Ekinci and Roukes 2005). This nonlinearity is characterized as a deviation from a linear increase in amplitude with driving force and accompanied by a decrease in Q (Fig. 5.8B).

5.11 Thermal Noise Spectrum

After determining the resonance frequency of a particular resonator we turn off the drive and measure the fluctuations. The voltage noise power spectrum $S_v^f = V^2/B$, where V is the voltage output of the photodiode and B is the resolution bandwidth. S_V^f has a contribution from a constant background electrical noise in the system, $S^f_{electrical}$, and a contribution from the thermal mechanical oscillation peak, S_x^f. $S^f_{electrical}$ and S_x^f are incoherent noise sources so their contributions to the voltage power add linearly

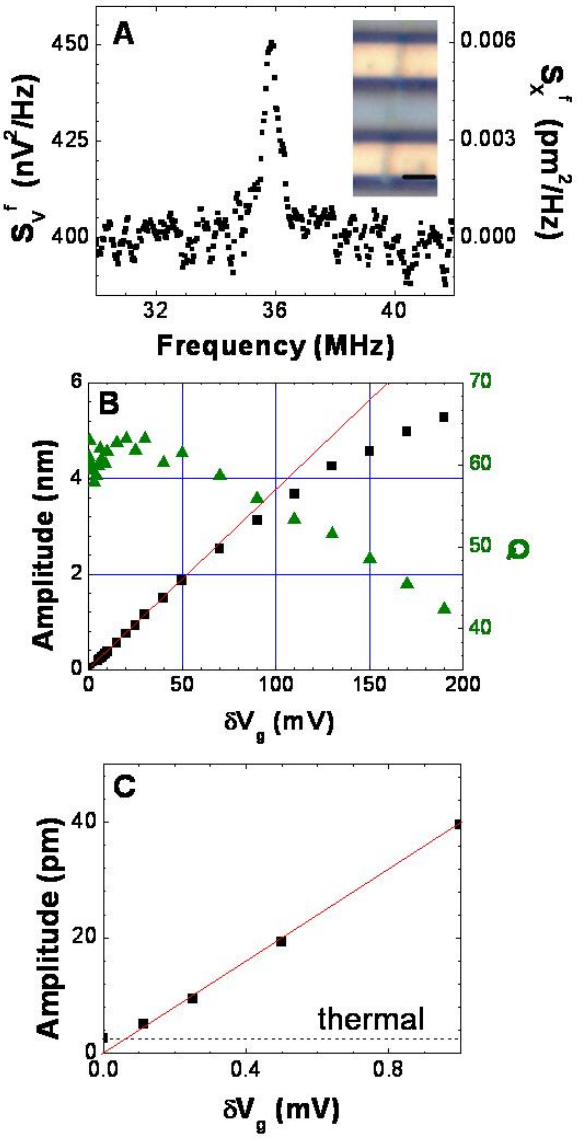

Figure 5.8 (A) Noise power density versus frequency taken at a resolution bandwidth of 1 kHz. (inset) An optical image of the resonator. The resonator has dimensions t = 5 nm, L = 2.7 μm, and w = 630 nm. Scale bar = 2 μm. (B) Amplitude of resonance and quality factor versus δV_g for V_g^{DC} = 2 V. (C) Expanded view of (B) for small δV_g.

such that $S_v^f = S^f_{electrical} + \alpha S_x^f$, where α is a constant scaling factor relating resonator displacement with changes in the measured photodetector voltage.

The thermal oscillation of a resonator is expected to have a spectral density given by:

$$S_x^f = \frac{2k_B T f_0^3}{\pi \kappa_{\text{eff}} Q} \text{ x } \frac{1}{(f_0^2 - f^2)^2 + (f\, f_0/Q)^2} \tag{5.3}$$

where the total thermal motion of a resonance peak must obey the equipartion theorem.

$$x_{th}^2 = \int_0^\infty S_x^f \, df = \frac{k_B T}{\kappa_{eff}} \tag{5.4}$$

Fitting the voltage power spectral density S_v^f to the theoretical distribution S_x^f, we determine the scaling factor α.

The amplitude of a driven resonance, x_{driven}, is related to the measured voltage signal, $V_{driven,}$ by:

$$x^2_{driven} = (V^2_{driven} - V^2_{background})/\alpha \tag{5.5}$$

Once again, $V_{background}$ is the constant offset due to the background electrical noise. It is important to note that the scaling factor is dependent on the device measured as well as the precise optical conditions such as laser focus and spot location. Any changes to these parameters require a recalibration of the scaling factor.

5.12 Sensitivity

Two applications of nanomechanical resonators are ultralow mass detection

and ultrasensitive force detection. The low effective mass coupled with high surface area makes graphene resonators ideal candidates for mass sensing. The minimum detectable mass for a resonator is:

$$\delta M \approx 2m_{eff}\sqrt{\frac{\Delta f}{Q\omega}}10^{-DR/20} \tag{5.6}$$

where the dynamic range, *DR*, is the decibel measure of the ratio between the amplitude of onset of non-linearity to the noise floor and Δf is the measurement bandwidth (Ekinci, Yang et al. 2004). For the resonator shown in Fig. 5.8, the dynamic range is ~ 60 dB, giving a room temperature mass sensitivity of ~ 0.2 zeptograms/$Hz^{1/2}$**.** This is a few times better in sensitivity to current state of the art room temperature NEMS (Ilic, Craighead et al. 2004). Even though the mass is much lower than standard NEMS due to the small thickness of graphene, the quality factor at room temperature is lower by a similar amount. Nevertheless this mass sensitivity is smaller than a single Au atom (0.3 zeptograms) making single atom mass sensing at room temperature possible. In addition, mass sensing with graphene NEMS would be greatly enhanced by improving the quality factor.

The ultimate limit on the force sensitivity is set by the thermal fluctuations in the resonator:

$$F_{\min} = \sqrt{\frac{4\kappa_{eff}k_bTB}{Q\omega_0}} \tag{5.7}$$

For the resonator in Fig. 5.8A, this results in a force sensitivity of 0.9 $fN/Hz^{1/2}$. Using Eq. 1, this corresponds to a charge sensitivity of $dQ^f = dF^f\, d/V_{DC} = 8x10^{-4}\, e/Hz^{1/2}$. This is a remarkable sensitivity demonstrated at room temperature; at low temperatures with the onset of higher quality factors it could rival those of RF SET electrometers

(1x10^{-5} e/Hz^{½}) (Schoelkopf, Wahlgren et al. 1998; LaHaye, Buu et al. 2004). The high Young's modulus, extremely low mass, and large surface area make these resonators ideally suited for use as mass, force, and charge sensors (Cleland and Roukes 1998; Kenny 2001; Burg and Manalis 2003; Knobel and Cleland 2003; Lavrik and Datskos 2003; Ekinci, Huang et al. 2004; Ilic, Craighead et al. 2004).

5.13 Conclusions

In this chapter, we created mechanical resonators form graphene sheets. Our thinnest resonator consisted of only a single atomic layer of atoms. This is the thinnest object imaginable. Using a simple drive and detection system we were able to measure the fundamental resonance frequency of these suspended atomic layers and this allowed us to characterize the quality factor, Young's modulus, tension, and ultimate sensitivities of these devices. However, the application of graphene NEMS extends beyond just mechanical resonators. This robust, conducting, membrane can act as a nanoscale supporting structure or atomically thin membrane separating two disparate environments. Chapter 6 examines this for the case of gases.

CHAPTER 6

IMPERMEABLE ATOMIC MEMBRANES FROM GRAPHENE SHEETS

6.1 Introduction

Membranes are fundamental components of a wide variety of physical, chemical, and biological systems, used in everything from cellular compartmentalization to mechanical pressure sensing. They divide space into two regions, each capable of possessing different physical or chemical properties. A simple example is the stretched surface of a balloon, where a pressure difference across the balloon is balanced by the surface tension in the membrane. Graphene, a single layer of graphite, is the ultimate limit: a chemically stable and electrically conducting membrane one atom in thickness(Bunch, van der Zande et al. 2007; Geim and Novoselov 2007; Meyer, Geim et al. 2007). An interesting question is whether such an atomic membrane can be impermeable to atoms, molecules and ions. In this chapter, we address this question for gases. We show that these membranes are impermeable and can support pressure differences larger than one atmosphere. We use such pressure differences to tune the mechanical resonance frequency by ~100 MHz. This allows us to measure the mass and elastic constants of graphene membranes. We demonstrate that atomic layers of graphene have stiffness similar to bulk graphite ($E \sim$ 1 TPa). These results show that single atomic sheets can be integrated with microfabricated structures to create a new class of atomic scale membrane-based devices.

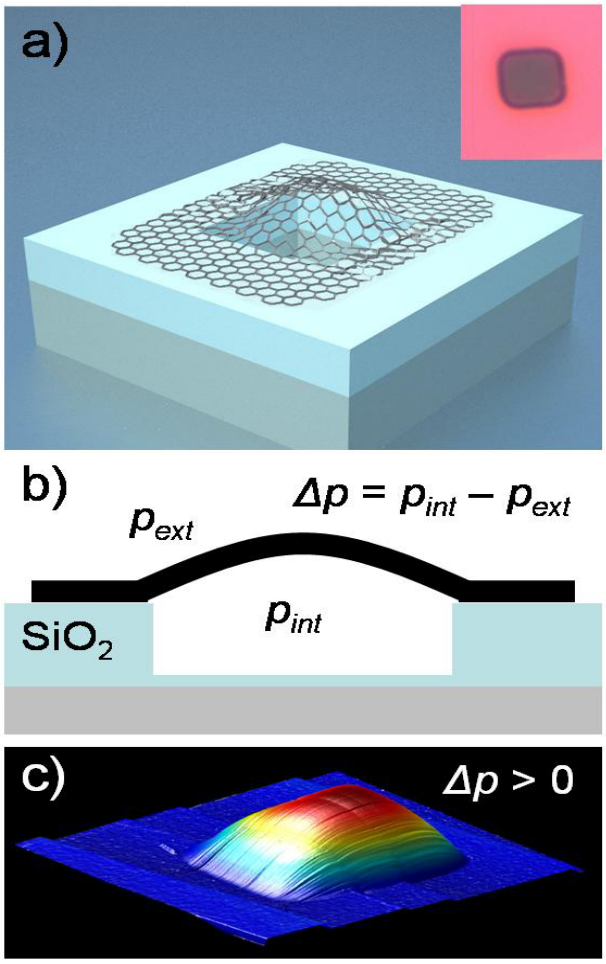

Figure 6.1 (a) Schematic of a graphene sealed microchamber. (Inset) Optical image of a single atomic layer graphene drumhead on 440 nm of SiO_2. The dimensions of the microchamber are 4.75 μm x 4.75 μm x 380 nm. (b) Side view schematic of the graphene sealed microchamber. (c) Tapping mode atomic force microscope (AFM) image of a ~ 9 nm thick many layer graphene drumhead with $\Delta p > 0$. The dimensions of the square microchamber are 4.75 μm x 4.75 μm. The upward deflection at the center of the membrane is $z = 90$ nm.

6.2 Device Fabrication

A schematic of the device geometry used here—a graphene-sealed microchamber—is shown in Fig. 6.1a. Graphene sheets are suspended over predefined wells in silicon oxide using mechanical exfoliation. First, a series of squares with areas of 1 to 100 μm^2 are defined by photolithography on an oxidized silicon wafer with a silicon oxide thickness of 285 nm or 440 nm. Reactive ion etching is then used to etch the squares to a depth of 250 nm to 3 μm leaving a series of wells on the wafer. Mechanical exfoliation of Kish graphite using Scotch tape is then used to deposit suspended graphene sheets over the wells.

Each graphene membrane is clamped on all sides by the van der Waals force between the graphene and SiO_2, creating a ~ $(\mu m)^3$ volume of confined gas. The inset of Fig. 1a shows an optical image of a single layer graphene sheet forming a sealed square drumhead with a width $W = 4.75$ μm on each side. Raman spectroscopy was used to confirm that this graphene sheet was a single layer in thickness(Ferrari, Meyer et al. 2006; Gupta, Chen et al. 2006; Graf, Molitor et al. 2007). Chambers with graphene thickness from 1 to ~ 75 layers were studied.

6.3 Pressure Differences

After initial fabrication, the pressure inside the microchamber, p_{int}, is atmospheric pressure (101 kPa). If the pressure external to the chamber, p_{ext}, is changed, we found that p_{int} will equilibrate to p_{ext} on a time scale that ranges from minutes to days, depending on the gas species and the temperature. On shorter time scales than this equilibration time, a significant pressure difference $\Delta p = p_{int} - p_{ext}$ can exist across the membrane, causing it to stretch like the surface of a balloon (Fig. 6.1b). Examples are shown for $\Delta p > 0$ in Fig. 6.1c and $\Delta p < 0$ in Fig. 6.2a.

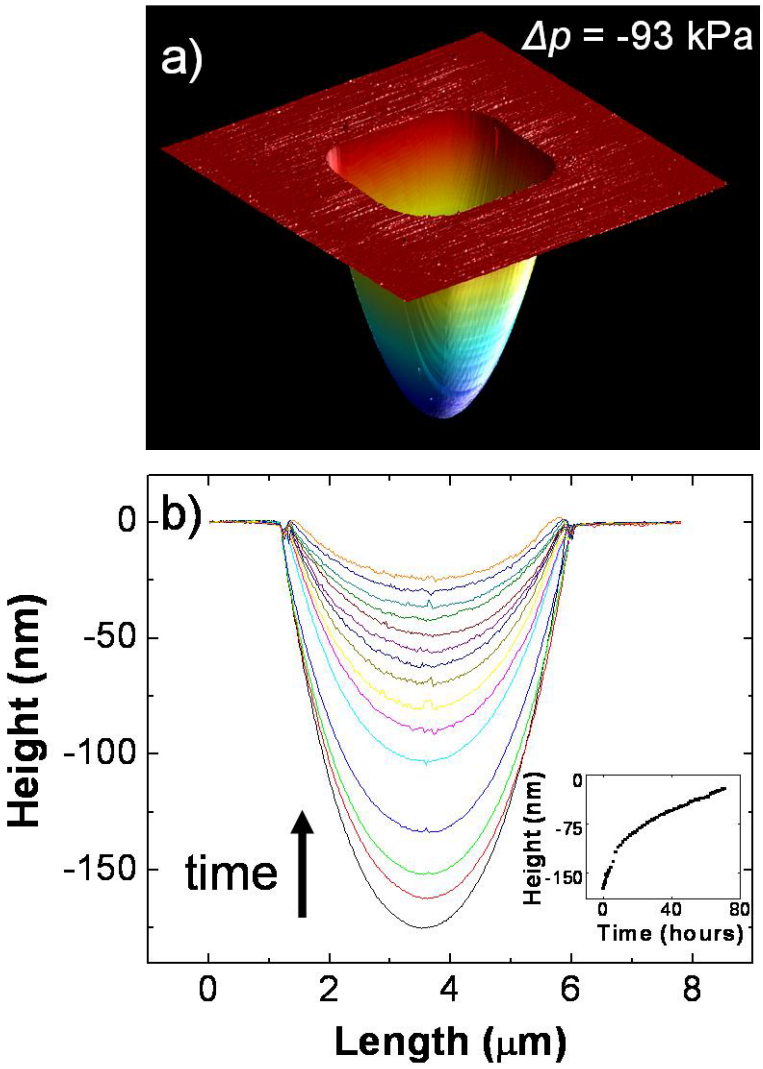

Figure 6.2 (a) AFM image of the graphene sealed microchamber of Fig. 6.1a with Δp = -93 kPa across it. The minimum dip in the z direction is 175 nm. (b) AFM line traces taken through the center of the graphene membrane of (a). The images were taken continuously over a span of 71.3 hours and in ambient conditions. (Inset) The deflection at the center of the graphene membrane vs. time. The first deflection measurement (z = 175 nm) is taken 40 minutes after removing the microchamber from vacuum.

To create a positive pressure difference, $\Delta p > 0$, as shown in Fig. 6.1c, we place a sample in a pressure chamber with p_{ext} = 690 kPa N_2 gas for 3 hours. After removing it, a tapping mode atomic force microscope (AFM) image at ambient external pressure (Fig. 6.1c) shows that the membrane bulges upwards. Similarly, we can create a lower pressure in the chamber, $\Delta p < 0$, by storing the device under vacuum and then returning it to atmospheric pressure. The graphene-sealed microchamber from Fig. 6.1a (inset) is placed in a pressure of ~ 0.1 Pa for 4 days and then imaged in ambient conditions by AFM (Fig. 6.2a). The graphene membrane is now deflected downward indicating $p_{int} < p_{ext}$.

6.4 Leak Rate

Over time, the internal and external pressures equilibrate. Figure 6.2b shows a series of AFM line traces through the center of the graphene membrane taken over a period of three days. The deflection z at the center of the membrane is initially z_o = 175 nm and decreases slowly over time, indicating a slow air leak from the microchamber. The time scale for decay is approximately 24 hours. We characterize the equilibration process by monitoring the pressure change and using the ideal gas law to convert this to a leak rate:

$$\frac{dN}{dt} = \frac{V}{k_B T}\frac{dp_{in}}{dt} \tag{6.1}$$

where N is the number of atoms or molecules in the chamber. Figure 6.3 shows results for several different membranes of various thicknesses and for different gases. Air and argon show similar leak rates, while helium is 2 orders of magnitude faster. The helium leak rates ranged from 10^5 atoms/s to ~10^6 atoms/s with no noticeable dependence on thickness from 1 – 75 atomic layers. All the data was taken in a similar

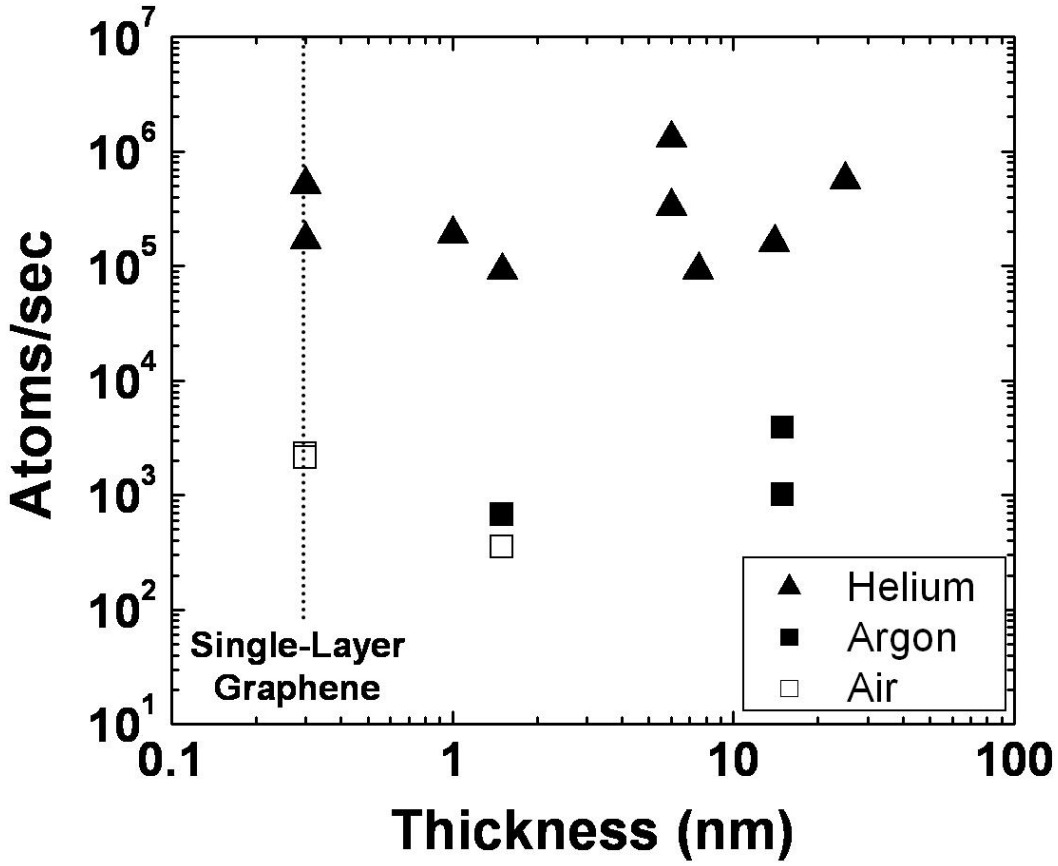

Figure 6.3 Scatter plot of the gas leak rates vs. thickness for all the devices measured. Helium rates are shown as solid triangles (▲), argon rates are shown as solid squares (■) and air rates are shown as hollow squares (□).

manner where approximately the same pressure difference was applied across the membrane (see A.2).

The lack of dependence of the leak rate on the membrane thickness indicates that the leak is not through the graphene sheets, or though defects in these sheets. This suggests it is either through the glass walls of the microchamber or through the graphene-SiO_2 sealed interface. The former can be estimated from the known properties of He diffusion through glass(Perkins and Begeal 1971). Using Fick's law of diffusion and typical dimensions for our microchambers we estimate a rate of ~ 1-5 $\times 10^6$ atoms/sec. This is close to the range of values measured (Fig. 6.3).

Using this measured leak rate, we estimate an upper bound for the average transmission probability of a He atom impinging on a graphene surface as:

$$\frac{dN}{dt}\frac{2d}{Nv} < 10^{-11} \qquad (6.2)$$

where d is the depth of the microchamber, and v is the velocity of He atoms. In all likelihood, the true permeability is orders of magnitude lower than the bound given above. Simple estimates based on WKB tunneling of He atoms through a perfect graphene barrier (~ 8.7 eV barrier height, 0.3 nm thickness) and through a "window" mechanism whereby temporary bond breaking lowers the barrier height to ~ 3.5 eV, give a tunneling probability at room temperature many orders of magnitude smaller than we observe (see A.3)(Hrusak, Bohme et al. 1992; Saunders, Jimenez-Vazquez et al. 1993; Murry and Scuseria 1994). If we approximate Helium atoms as point particles, classical effusion through single atom lattice vacancies in the graphene membrane occurs in ~ 1 sec and therefore much faster than the rates we measure (see A.4). We therefore conclude that the graphene layer is essentially perfect and for all intents and purposes impermeable to all standard gases, including He.

6.5 Elastic Constants

The impermeability of the graphene membrane allows us to use pressure differences to apply a large, well-defined force that is uniformly distributed across the entire surface of the membrane. This ability to create controlled strain in the membrane has many uses. First, we can measure the elastic properties of the graphene sheet. A well-known and reliable method used to study the elastic properties of films is the bulge test technique(Vlassak and Nix 1992). The deflection of a thin film is measured as a uniform pressure is applied across it. This surface tension, S, is the sum of two components: $S = S_0 + S_p$ where S_0 is the initial tension per unit length along the boundary and S_p is the pressure-induced tension. Tension is directly related to the strain, ε, as

$$S = \frac{Et}{(1-\upsilon)}\varepsilon \tag{6.3}$$

where E is the Young's modulus, t is the thickness, and υ is Poisson's ratio. For the geometry of a square membrane, the pressure difference as a function of deflection can be expressed as(Vlassak and Nix 1992):

$$\Delta p = \frac{4z}{W^2}\left(c_1 S_o + \frac{4c_2 Etz^2}{W^2(1-\upsilon)}\right) \tag{6.4}$$

where $c_1 = 3.393$ and $c_2 = (0.8+0.062\upsilon)^{-3}$.

Using the deflection and pressure difference in Fig. 6.2b and accounting for initial slack in the membrane as discussed later in the text, we determine the elastic constants of graphene to be $Et/(1-\upsilon) = 390 \pm 20$ N/m (see A.1 and A.5). The accepted values for the experimental and theoretical elastic constants of bulk graphite and

graphene—both 400 N/m(Blakslee, Proctor et al. 1970; Kelly 1981; Huang, Wu et al. 2006)—are within the experimental error of our measurement. This is an important result in nanomechanics considering the vast literature examining the relevance of using elastic constants for bulk materials to describe atomic scale structures (Yakobson, Brabec et al. 1996; Huang, Wu et al. 2006).

6.6 Surface Tension

The surface tension in the pressurized membrane can be readily obtained from the Young-Laplace equation, $\Delta p = S(1/R_x + 1/R_y)$ where $R_{x(y)}$ is the radius of curvature of the surface along the $x(y)$ direction. The shape of the bulged membrane with Δp = -93 kPa in Fig. 1d directly gives $R_{x(y)}$. At the point of maximum deflection it is $R_x = R_y$ = 21 μm which amounts to a surface tension S = 1 N/m**.** This is 14 times the surface tension of water, but corresponds to a small strain in the graphene of 0.26 %. The atomically thin sealed chambers reported here can support pressures up to a few atmospheres. Beyond this, we observe that the graphene slips on the surface. Improved clamping could increase allowable pressure differentials dramatically.

This pressure induced-strain in the membrane can also be used to control the resonance frequency of the suspended graphene. This is shown in Fig. 6.4a for a monolayer device prepared with a small gas pressure p_{int} in the chamber. Figure 6.4b shows results on a 1.5 nm thick membrane. The vibrations of the membrane are actuated and measured optically, as previously reported(Bunch, van der Zande et al. 2007). The frequency changes dramatically with external pressure, exhibiting a sharp minimum at a specific pressure and growing on either side. Sufficiently far from the minimum frequency, f_0, the frequency scales as $f^2 \propto \Delta p$ (Fig. 6.4b).

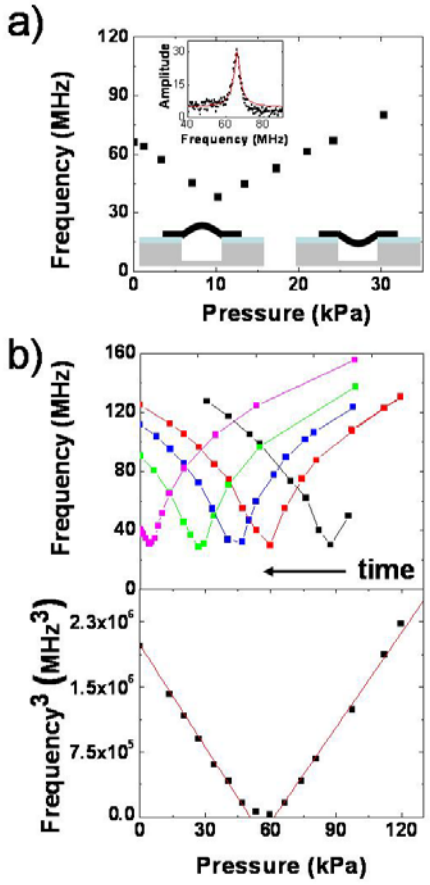

Figure 6.4 (a) Resonance frequency vs. external pressure for the single-layer graphene sealed microchamber shown in Fig. 6.1a. (Upper inset) Resonance frequency curve taken at p_{ext} = 27 Pa with a resonance frequency of f = 66 MHz and Q = 25. (Lower insets) Schematic of the configuration of the microchamber at various applied pressures. The graphene is puffed upwards or downwards depending on Δp. (b) (upper) Resonance frequency vs. p_{ext} for a 1.5 nm-thick few layer graphene sealed microchamber. Each curve was taken at a different time over a span of 207 hours, and the device was left in p_{ext} ~ 0.1 mPa in between each measurement. (lower) (Resonance frequency)^3 vs. p_{ext} for the red scan in Fig. 4b. A linear fit to the data is shown in red.

This behavior follows from the pressure induced changes in the tension *S* in the membrane. Neglecting the bending rigidity, the fundamental frequency of a square membrane under uniform tension is given by:

$$f = \sqrt{\frac{S_0 + S_p}{2mW^2}} \tag{6.5}$$

where *m* is the mass per unit area(Timoshenko, Young et al. 1974). Sufficiently far from f_0, equations (6.4) and (6.5) can be combined with the approximation:

$$S \approx \frac{\Delta p W^2}{16z} \tag{6.6}$$

to get the following expression:

$$f^3 = \Delta p \sqrt{\frac{c_2 Et}{2048 m^3 W^4 (1-\upsilon)}} \tag{6.7}$$

This gives the functional form observed in Fig. 6.4b with the prefactor consisting of the elastic constants of the membrane and the mass. Using *Et/(1-υ)* determined previously, we fit (6.7) to the data of Fig. 6.4a and 6.4b to determine the mass per area of the membranes. We find $m = 9.6 \pm 0.6 \times 10^{-7}$ kg/m^2 for the monolayer of Fig. 6.4a. This is 30 % higher than the theoretical value for a single layer of graphene of 7.4×10^{-7} kg/m^2. One possibility for this extra mass is adsorbates which would significantly shift the mass of a single atom membrane. The 1.5 nm-thick few-layer membrane of Fig. 6.4b has a $m = 3.1 \pm 0.2 \times 10^{-6}$ kg/m^2. This corresponds to ~ 4 atomic layers in thickness. Previous attempts to deduce the mass from resonance measurements of doubly clamped beams were obscured by the large initial tension in the resonators(Bunch, van der Zande et al. 2007). Exploiting the impermeability of

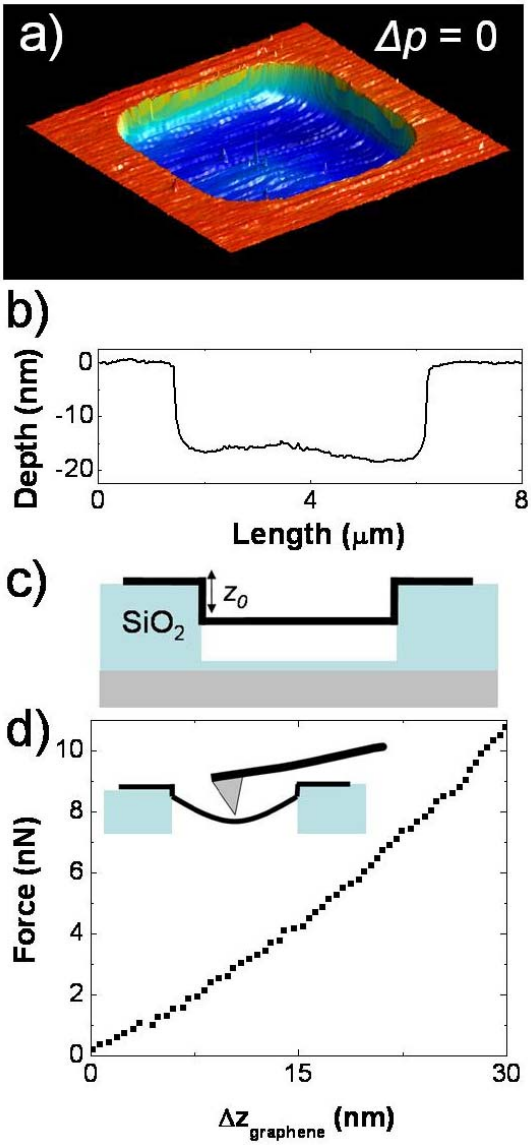

Figure 6.5 (a) Tapping mode AFM image of the single-layer graphene sealed microchamber shown in Fig. 6.1a with $\Delta p = 0$. (b) Line cut through the center of the graphene membrane in (a). (c) Schematic of the graphene membrane at $\Delta p = 0$ with an initial deflection z_0 due to self-tensioning. (d) Force-distance curve taken at the center of the graphene membrane in (a) at $\Delta p = 0$. The spring constant of the cantilever used is $k_{tip} = 0.67$ N/m.

graphene membranes to controllably tune the resonance frequency gives us the mass of the suspended graphene membrane regardless of this initial tension. To our knowledge, this is the first direct measurement of the mass of graphene.

The minimum frequency, f_0, corresponds to $S_p = 0$, i.e. $p_{int} = p_{ext}$. The monolayer graphene membrane in Fig. 6.4a has $f_0 = 38$ MHz when $\Delta p = 0$. This frequency is significantly higher than expected for a graphene square plate under zero tension (0.3 MHz) suggesting that at $\Delta p = 0$, the resonance frequency is dominated by S_0 and not the bending rigidity. Using the experimentally measured mass of the monolayer membrane above we deduce an $S_0 \sim 0.06$ N/m. This is similar to what was previously observed in doubly-clamped graphene beams fabricated by the same method (see Chapter 5) (Bunch, van der Zande et al. 2007).

6.7 Self-Tensioning

The origin of this tension is clear from Fig. 6.5a which shows a tapping-mode AFM image of the suspended monolayer graphene membrane of Fig. 6.2a with $\Delta p = 0$. The image shows the graphene membrane to have a ~ 17 nm dip along the edges of the suspended regions where the graphene meets the SiO_2 sidewalls (Fig. 6.5b). This results from the strong van der Waals interaction between the edge of the graphene membrane and the SiO_2 sidewalls (Fig. 6.5c), which previously has been estimated to be $U \sim 0.1$ J/m^2 (Ruoff, Tersoff et al. 1993; Hertel, Walkup et al. 1998). This attraction yields a surface tension $S_0 = U \sim 0.1$ N/m which is close to the value extracted from the resonance measurement.

The tension in the membrane can also be probed by pushing on the membrane with a calibrated AFM tip (Frank, Tanenbaum et al. 2007). This force-deflection curve gives a direct measure of the spring constant $k_{graphene} = 0.2$ N/m of the graphene membrane, as shown in Figure 6.5d. Neglecting the bending rigidity, the tension can

be obtained using $S \approx (k_{graphene}/2\pi)\ ln\ (R/r)$, where R is the radius of the membrane and r is the radius of the AFM tip (Tanizawa and Yamamoto 2004). Assuming $r \sim 50$ nm, this gives $S \sim 0.1$ N/m, close to both the theoretical value and the value measured using the resonance frequency technique above. These results show that self-tensioning in these thin graphene sheets dominates over the bending rigidity, and this tension will smooth corrugations that may occur in tension-free graphene membranes(Meyer, Geim et al. 2007).

6.8 Conclusions

We envision many applications for these graphene sealed microchambers. They can act as compliant membrane sensors which probe pressures in small volumes and explore pressure changes associated with chemical reactions, phase transitions, and photon detection(Jiang, Markutsya et al. 2004; Mueggenburg, Lin et al. 2007). In addition to these spectroscopic studies, graphene drumheads offer the opportunity to probe the permeability of gases through atomic vacancies in single layers of atoms(Hashimoto, Suenaga et al. 2004) and defects patterned in the graphene membrane can act as selective barriers for ultrafiltration(Rose, Debray et al. 2006; Striemer, Gaborski et al. 2007). The tensioned suspended graphene membranes also provide a platform for STM imaging of both graphene(Ishigami, Chen et al. 2007; Rutter, Crain et al. 2007; Stolyarova, Rim et al. 2007) and graphene-fluid interfaces and offer a unique separation barrier between 2 distinct phases of matter that is only one atom thick.

CHAPTER 7

CONCLUSIONS

7.1 Summary

This thesis explored the electrical and mechanical properties of a new unique two dimensional atomic crystal - graphene. Chapters 1-3 included an overview of the basic concepts relevant to the experimental results presented in Chapters 4-6. Chapter 1 began by discussing the mechanical and electrical properties of nanoscale systems. Chapter 2 provided an introduction to the field of nanoelectromechanical systems. This was followed by Chapter 3, which introduced graphene with a discussion of its electrical and mechanical properties and a brief overview of the current understanding of this new material.

The experimental section began in Chapter 4. We performed low temperature electrical transport measurements on gated, few-layer graphene quantum dots. In devices with low contact resistances, we used longitudinal and Hall resistances to extract a carrier density of 2-6 x 10^{11} holes per sheet and a mobility of 200-1900 cm^2/V-s. In devices with high resistance contacts, we observed Coulomb blockade phenomena and inferred the charging energies and capacitive couplings. These experiments demonstrated that electrons in mesoscopic graphite pieces are delocalized over nearly the whole graphite piece down to low temperatures.

An experimental study of the mechanical properties of suspended graphene began in Chapter 5. Nanoelectromechanical systems were fabricated from single and multilayer graphene sheets by mechanically exfoliating thin sheets from graphite over trenches in SiO_2. Vibrations with fundamental resonant frequencies in the MHz range were actuated either optically or electrically and detected optically by interferometry.

We demonstrated room temperature charge sensitivities down to $8x10^{-4}$ $e/Hz^{½}$. The thinnest resonator consists of a single suspended layer of atoms and represents the ultimate limit of two dimensional nanoelectromechanical systems.

Chapter 6 extended this work on mechanical resonators from graphene sheets to graphene membranes which are clamped on all sides and seal a small volume of gas in a microchamber. In this work, we demonstrated that a graphene membrane is impermeable to gases down to the ultimate limit in thickness of only one atomic layer. It can withstand a pressure difference greater than 1 atmosphere and we used such a pressure difference to determine the mass of the membrane and extract the elastic constants. We found that a single sheet of graphene is impermeable to helium gas atoms and therefore free of any significant vacancy over micron size areas. We also determined the elastic constants of a single layer of graphene to be similar to bulk graphite. This addresses a longstanding question in nanomechanics as to the relevance of using bulk elastic constants to atomic scale systems. Graphene represents the thinnest membrane possible, and by establishing a pressure difference across this membrane we created the world's thinnest balloon.

7.2 Future Outlook

There are still many new and interesting problems to address with suspended graphene NEMS. An intriguing and potentially revolutionary application for suspended atomically thin graphene sheets which remains largely unexplored is as an ultrathin membrane with atomic scale pores. Ideal membranes which act as selective barriers should be as thin as possible to increase flux and reduced blockage, mechanically robust to prevent breakage, and have well defined pores to increase selectivity. Graphene represents the thinnest membrane possible (one layer of atoms) with the smallest pore sizes attainable (single atomic vacancies), and unprecedented

mechanical stability. Fabricating controlled atomic scale pores in these graphene membrane represents a significant technological achievement which may find use in a wide range of applications in defense (biological and chemical detection), biotechnology (ion and molecular separation), energy (batteries and fuel cells), and the environment (desalination and decontamination).

These graphene membranes with atomic scale pores can be used to probe both gas and ionic transport. Due to the small volume of gas trapped in graphene sealed microchambers, gas effusion through atomic pores is extremely sensitive to the pore size (See A.4). Using the resonant frequency of the membrane the energetic of this small volume of trapped gas can be probed as well. Photon absorption, chemical reactions, and phase transitions can be examined with high time and energy resolution. Ionic transport through a voltage gated graphene membrane can be used to understand the electrostatics of ionic double layers and integrating graphene membranes with biological membranes and ion channels could yield new insights on how these biological systems function as well as new applications in biotechnology.

There are also many unanswered questions on the nanomechanics of graphene sheets. By performing the bulge test on rectangular and square membranes one will be able to experimentally measure Poisson's ratio which has never been done for a single graphene sheet and may give different results depending on the number of stacked graphene sheets. A bulge test performed on few layer graphene sheets will also yield interesting information about the shear modulus of graphene sheets. Studying how these layers slide with respect to one another in varying environments would allow researchers to elucidate the exact mechanism and strength of this interlayer interaction. Finally, there are a bunch of neat opportunities to study folds, wrinkles, and crumpling of graphene sheets – something that can be termed graphene origami. This thesis just touched the surface of what is possible with this new and exciting

material, and hopefully new avenues open up as scientists and engineers continue to explore this unique new material.

APPENDIX

A.1 Slack and Self Tensioning in Graphene Membranes at Δp = 0

Figure 6.5 shows an AFM image of a graphene membrane with $\Delta p = 0$. Since the cantilever-surface interaction is expected to be different for AFM measurements over the relatively-pliable suspended and the rigid SiO_2-supported graphene, the depth of the membrane z_0, at $\Delta p = 0$ must be determined via force and amplitude calibrations of the cantilever over each surface (Whittaker, Minot et al. 2006). A representative calibration measurement is shown in Fig. A.1. Both the amplitude (upper) and deflection (lower) of the AFM tip is measured while approaching the surface.

Over the SiO_2-supported surface, the difference between the actual surface position and the position given by the image in Fig. 6.4a can be determined by subtracting the height at which the AFM tip begins to bend due to unbroken contact with the surface (A) from the height at which the amplitude setpoint intersects with the amplitude response curve (B) (Fig. A.1). The surface is determined to be 30 nm below the amplitude set point position.

Since suspended graphene is more pliable than supported graphene, the onset of the AFM cantilever's deflection of Fig. A.1 is more gradual, and thus cannot be readily used to determine the equilibrium height of the suspended graphene. Instead, we note that when in unbroken-contact with the graphene surface, any deviations of the AFM tip from the equilibrium (lowest-strain) depth of the membrane will result in an increase in the membrane tension as the tip either pulls up or pushes down on the membrane. This increase in tension on either side of the equilibrium position will cause a decrease in cantilever response amplitude, resulting in a peak in the cantilever-amplitude response at the equilibrium position, similar to what has been observed for

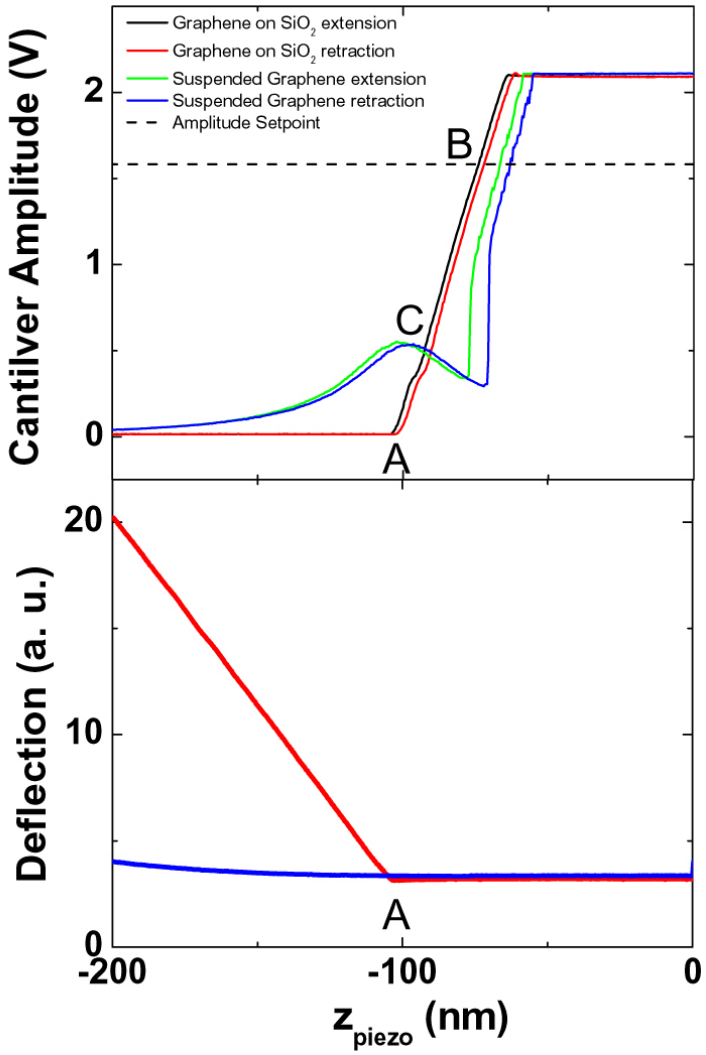

Figure A.1 (upper) Driven oscillation amplitude of the tapping mode AFM cantilever with resonance frequency = 349 kHz vs. piezo extension as tip is brought into contact with the surface. Black and red are extension and retraction curves over the supported graphene on SiO_2 surface. Green and blue are extension and retraction curves over the suspended graphene membrane. (lower) The deflection of the cantilever vs. piezo extension. The upper and lower traces were taken simultaneously.

suspended carbon nanotubes(Whittaker, Minot et al. 2006). This occurs at ~100 nm, or 34 nm below the amplitude setpoint position (C).

Comparing these setpoint-to-surface depths for suspended and supported graphene, we find that the equilibrium depth of the suspended membrane is 17 + (34 – 30) = 21 nm below the SiO_2-supported surface where 17 nm is the distance measured in Fig. 6.4a. Repeating these measurements across the center of the membrane yields an average equilibrium membrane-depth depth z_0 = 17 ± 1 nm + (6 ± 2 nm) = 23 ± 3 nm.

A.2 Measuring the Gas Leak Rates

The gas leak rate in Chapter 6 is measured by monitoring p_{int} vs. time. For the case of the leak rate of air, the microchamber begins with p_{int} ~ 100 kPa Air. This is verified by a scan of frequency vs. p_{ext}. A similar scan is performed once every few hours to monitor p_{int} while the device is left at p_{ext} ~ 0.1 mPa between each measurement (Fig. 6.4b). The leak rate of argon is measured in a similar manner except the microchamber begins with a p_{int} ~ 0 kPa argon and ~ 10 kPa air. The microchamber is left in p_{ext} ~ 100 kPa argon between measurements to allow argon to diffuse into the microchamber. This diffusion is monitored by finding the minimum pressure in a scan of frequency vs. p_{ext}.

To measure the helium leak rate we apply a Δp ~ 40 – 50 kPa He and monitor the resonance frequency as helium diffuses into the microchamber. It will diffuse until the partial pressure of helium is the same inside and outside the microchamber. From the slope of the line we extract a helium leak rate for the devices using equation (6.1) (Fig. A.2). Leak rates from square membranes with sides varying from 2.5 to 4.8 μm were measured with no noticeable dependence of the leak rate on area.

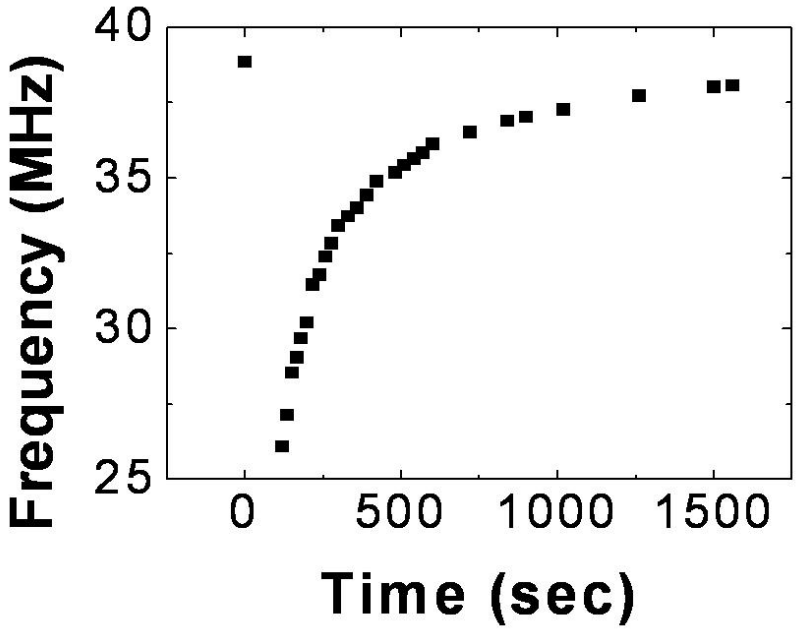

Figure A.2 Resonance frequency vs. time for a single layer graphene sealed nanochamber exposed to 357 torr external pressure of He. The internal pressure of the nanochamber is initially at 500 torr of Air. At time t = 0 sec, 357 torr external pressure of He is applied to the nanochamber. The resonant frequency is measured every few seconds until the frequency approaches its initial value.

A.3 Tunneling of He Atoms across a Graphene Sheet

The probability of a particle with a mass *m*, tunneling across a finite potential barrier with a height *V*, and distance *x*, is given by:

$$p = e^{\frac{-2x\sqrt{2m(V-E)}}{\hbar}} \qquad \text{(A.1)}$$

Simple estimates based on tunneling of He atoms through a perfect graphene barrier at room temperature (~ 8.7 eV barrier height, 0.3 nm thickness) give a tunneling probability ~250 orders of magnitude smaller than the experimental limit given above (Hrusak, Bohme et al. 1992; Murry and Scuseria 1994). Furthermore, measurements of He entering C_{60} through the "window" mechanism whereby temporary bond breaking lowers the barrier height to ~ 3.5 eV, which still gives a tunneling probability ~150 orders of magnitude smaller than we observe in Chapter 6 (Saunders, Jimenez-Vazquez et al. 1993; Murry and Scuseria 1994).

A.4 Classical Effusion through Single Atom Lattice Vacancies

For the case of classical effusion through a small hole, the number of molecules is given by:

$$n = n_0 e^{-\frac{A}{V}\sqrt{\frac{k_b T}{2\pi m}}t} \qquad \text{(A.2)}$$

where n_0 is the initial number of molecules, A is the area of the hole, V is the volume of the container, k_b is Boltzman's constant, T is temperature, t is time, and m is the atomic mass of the gas (Reif 1965). For a defect area of 1 nm^2, effusion of gas would take place in much less than one second. Even a one atom defect would leak in less

than one second.

The reason for such fast effusion is the volume of the container for the graphene sealed microchambers is so small (typically ~ 1 μm^3). The number of molecules in the microchamber depends on the ratio A/V, and a defect with an area of 1 nm^2 in a 1 μm^3 box yields an area/volume ratio of 1 m^{-1}. If this was scaled up to macroscopic dimensions, it is equivalent to a 1 m^3 box with a defect of area = 1 m^2. This suggests that any leak rate out of nanochambers is extremely sensitive to the defect area and therefore an accurate measure of that area. This makes detection of small changes in defect area by adsorbed molecules highly sensitive. One should note that such a detection scheme is impossible with thicker silicon NEMS since their compliance seriously diminishes when the lateral dimensions approach 1 μm. By using atomic scale thickness resonators, we can overcome these inherent limitations in Si MEMS technology. Previous attempts to fabricate compliant micron size membranes have focused on nanoparticle arrays and inorganic membranes(Jiang, Markutsya et al. 2004; Mueggenburg, Lin et al. 2007). Our graphene membranes are 30X-100X thinner and have a single crystal structure making them much more robust.

A.5 Extrapolating Deflections and Pressure Differences

To determine the elastic constants of graphene using equation (6.3), we extrapolate the deflection in Fig. 6.1e (inset) to z = 181 nm to account for a 40-minute sample-load time, assume an initial pressure difference across the membrane, Δp = 93 kPa, and a negligible initial tension. The latter two assumptions are verified using resonance measurements. The actual deflection used in equation (6.3) is obtained by subtracting the extrapolated deflection z = 181 nm from the initial deflection $z_0 = 23 \pm 3$ nm at $\Delta p = 0$. This initial deflection is determined from the AFM image in Fig. 6.4a and AFM force-distance curves Fig. A.1.

A.6 Experimental Setup for Optical Drive and Detection

The experimental setup used to actuate and detect vibrations has previously been discussed in detail by Keith Aubin in his PhD thesis (Aubin 2005). I will follow his description closely. We will follow the red detection laser's path (Fig A.1). The polarized laser light is directed around the table by 2 mirrors (B and C). One of these mirrors (C) is on a magnetic mount. This is to allow for an easy substitution of other detection lasers (a tunable 1 W Ti:Sapphire laser is an example). The beam then goes through a pinhole (D) that is used for alignment purposes. This is followed by a circular variable neutral density filter (E) which is used to control the intensity of the laser. The beam then goes through a beam expander which consists of 2 lenses with differing focal lengths f_1 and f_2. The first of these lenses (F) is an objective mounted on a 2 axis stage. The 2nd lens (G) is fixed. To make an effective Keplerian beam expander from 2 lenses must be aligned such that their focal lengths match. The expanded beam is made large enough to backfill the final objective (Z). This expanded polarized beam passes through a polarized beam splitter (H) which allows all the light to pass through. The function of this beam splitter is to direct the image of the sample and red laser into the camera (I) to align the red laser spot onto the resonator. The detection laser then passes through a removable linear polarizer (J) which is used only used during alignment and then removed. The polarizer is aligned 45^{o} with respect to the detection laser. It is needed to change the polarization of reflected light from the chamber so that it is directed into the camera by the polarized beam splitter (H). The beam then enters an unpolarized beam splitter (R) where 50% of the light is directed into a power meter (T). A removable filter (S) is used to selectively filter the blue or red light to measure the power. The remaining 50% of the red light passes (R) combined with the blue drive laser. The blue laser (K) is modulated by a spectrum

analyzer (EE). The blue light passes through a pinhole (L) and a beam expander (M) and (N) which cleans the beam. This expanded beam is directed around a mirror (O) into a filter wheel (P) that is used to tune the intensity. It then is deflected by another mirror (Q) which directs the light into the unpolarized beam splitter (R). At this point, 50% of the light goes into the power meter and 50% combines with the red detection laser and heads towards the sample chamber. Both the drive and detection laser beams pass through a ¼ wave plate (V) which circularly polarizes the beam. The beam passes a microscope slide that is used to reflect white light from a source (Y) focused with (X). The beam enters an objective (Z) which focuses the spot down to a diffraction limited spot onto the sample housed in a vacuum chamber (AA) which sits on a motorized xyz stage. The vacuum chamber is connected to a turbo pump (GG) and has a T valve connecting a vacuum gauge (FF) and a gas input (HH) consisting of a manual leak valve for leaking air or other gases.

The reflected light is then collected down the same approach path. It first passes through the lens (Z) and the microscope slide (W). It then goes through the ¼ wave plate (V). The circularly polarized returning light now becomes linearly polarized in a direction perpendicular to the direction of the incoming beam. When this linearly polarized light is incident on the polarized beam splitter, nearly 100% of the reflected light is passed through. This light is passed through a filter (BB) which filters out the blue drive laser. The light is finally focused by a lens (CC) onto a high speed photodetector (DD) where the signal is collected by the spectrum analyzer (DD).

When the blue drive laser is not needed as in the case of electrostatic drive and optical detection, the unpolarized beam splitter (R) can be removed. This will send 100% of the red detection laser incident onto the sample. The data from the spectrum analyzer is collected by a Lab View program which has the capability to fit the

resonance peak to a Lorentzian and determine the quality factor from this fit.

a. Helium Neon Laser. Polarized 632.8 nm JDS uniphase model 1145 P.

b. Mirror

c. Mirror on a magnetic mount.

d. Pinhole

e. Circular Variable Neutral Density Filter

f. Lens LP1 Newport (beam expander component)

g. Lens P100A Newport (beam expander component)

h. Polarized beam splitter

i. Camera on a 3 axis stage connected to a digital camera and color monitor. Lens is a Navitar 1-60191.

j. Removable polarizer.

k. Blue Diode Laser - Picoquant MDL 300 405 nm.

l. Pinhole

m. Lens Newport 4100 G (beam expander component)

n. Lens Newport P100A (beam expander component)

o. Mirror on movable mount U100-G Newport.

p. Circular Variable Neutral Density Filter Newport model 946

q. Mirror on movable mount U100-G

r. Non polarizing beam splitter mounted on an easily removable stand

s. Filter

t. Power meter

u. Polarizing beam splitter

v. ¼ wave plate

w. Microscope slide

x. Lens

y. White light source

z. Lens – objective

aa. Sample chamber mounted on a motorized stage with xyz translation

bb. Blue light filter

cc. Lens

dd. Photodetector - Visible 1 GHz low noise from New Focus. Mounted on a 3 axis translation stage - NRC model 430 Newport 360-90

ee. Agilent E 4402 B ESA_E series Spectrum Analyzer 9kHz – 3GHz

ff. Vacuum Guage

gg. Turbo Pump

hh. Input for gases.

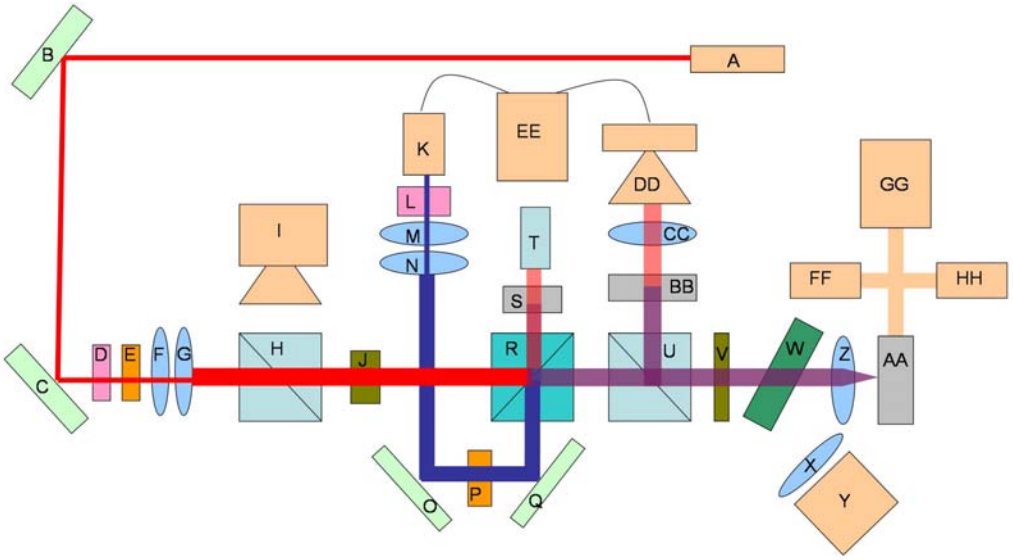

Figure A.3 Schematic of the experimental setup used to drive and detect resonance

REFERENCES

Aubin, K. L. (2005). Radio Frequency Nano/Microelectromechanical Resonators: Thermal and Nonlinear Dynamics Studies. Applied and Engineering Physics. Ithaca, NY, Cornell University**:** 115.

Beenakker, C. W. J. (1991). "Theory of Coulomb-Blockade Oscillations in the Conductance of a Quantum Dot." Physical Review B **44**(4): 1646-1656.

Begley, M. R. and T. J. Mackin (2004). "Spherical indentation of freestanding circular thin films in the membrane regime." Journal of the Mechanics and Physics of Solids **52**(9): 2005-2023.

Berger, C., Z. Song, et al. (2006). "Electronic Confinement and Coherence in Patterned Epitaxial Graphene." Science **312**(5777): 1191-1196.

Berger, C., Z. M. Song, et al. (2004). "Ultrathin epitaxial graphite: 2D electron gas properties and a route toward graphene-based nanoelectronics." Journal of Physical Chemistry B **108**(52): 19912-19916.

Blake, P., E. W. Hill, et al. (2007). "Making graphene visible." Applied Physics Letters **91**(6): 063124.

Blakslee, O. L., D. G. Proctor, et al. (1970). "Elastic Constants of Compression-Annealed Pyrolytic Graphite." Journal of Applied Physics **41**(8): 3373-3382.

Bockrath, M., D. H. Cobden, et al. (1997). "Single-electron transport in ropes of carbon nanotubes." Science **275**(5308): 1922-1925.

Bokaian, A. (1990). "Natural frequencies of beams under tensile axial loads " Journal of Sound and Vibration **142**(3): 481-498.

Bolotin, K. I., K. J. Sikes, et al. (2008). "Ultrahigh electron mobility in suspended graphene ": arXiv:0802.2389.

Bozovic, D., M. Bockrath, et al. (2003). "Plastic deformations in mechanically

strained single-walled carbon nanotubes." Physical Review B **67**(3).

Buitelaar, M. R., A. Bachtold, et al. (2002). "Multiwall carbon nanotubes as quantum dots." Physical Review Letters **88**(15): 156801.

Bunch, J. S., A. M. van der Zande, et al. (2007). "Electromechanical Resonators from Graphene Sheets." Science **315**(5811): 490-493.

Bunch, J. S., S. S. Verbridge, et al. (2008). "Impermeable Atomic Membranes from Graphene Sheets." Submitted

Bunch, J. S., Y. Yaish, et al. (2005). "Coulomb oscillations and Hall effect in quasi-2D graphite quantum dots." Nano Letters **5**(2): 287-290.

Burg, T. P. and S. R. Manalis (2003). "Suspended microchannel resonators for biomolecular detection." Applied Physics Letters **83**(13): 2698-2700.

Campbell, D. J. and M. K. Querns (2002). "Illustrating Poisson's Ratios with Paper Cutouts." J. Chem. Educ. **79**: 76.

Cleland, A. N. and M. L. Roukes (1998). "A nanometre-scale mechanical electrometer." Nature **392**(6672): 160-162.

Craighead, H. G. (2000). "Nanoelectromechanical systems." Science **290**(5496): 1532-1535.

Dienwiebel, M., G. S. Verhoeven, et al. (2004). "Superlubricity of Graphite." Physical Review Letters **92**(12): 126101.

Dingle, R., H. L. Stormer, et al. (1978). "Electron mobilities in modulation-doped semiconductor heterojunction superlattices." Applied Physics Letters **33**(7): 665-667.

Du, X., S.-W. Tsai, et al. "Unconventional Magnetotransport in Graphite." arXiv:cond-mat/0404725.

Ekinci, K. L., X. M. H. Huang, et al. (2004). "Ultrasensitive nanoelectromechanical mass detection." Applied Physics Letters **84**(22): 4469-4471.

Ekinci, K. L. and M. L. Roukes (2005). "Nanoelectromechanical systems." Review of Scientific Instruments **76**(6): 061101

Ekinci, K. L., Y. T. Yang, et al. (2004). "Ultimate limits to inertial mass sensing based upon nanoelectromechanical systems." Journal of Applied Physics **95**(5): 2682-2689.

Ferrari, A. C., J. C. Meyer, et al. (2006). "Raman Spectrum of Graphene and Graphene Layers." Physical Review Letters **97**(18): 187401.

Frank, I. W., D. M. Tanenbaum, et al. (2007). Mechanical properties of suspended graphene sheets, AVS.

Geim, A. K. and K. S. Novoselov (2007). "The rise of graphene." Nat Mater **6**(3): 183-191.

Graf, D., F. Molitor, et al. (2007). "Spatially Resolved Raman Spectroscopy of Single- and Few-Layer Graphene." Nano Lett. **7**(2): 238-242.

Gupta, A., G. Chen, et al. (2006). "Raman Scattering from High-Frequency Phonons in Supported n-Graphene Layer Films." Nano Lett.

Han, M., Y. , B. Ozyilmaz, et al. (2007). "Energy Band-Gap Engineering of Graphene Nanoribbons." Physical Review Letters **98**(20): 206805.

Hanson, R., L. P. Kouwenhoven, et al. (2007). "Spins in few-electron quantum dots." Reviews of Modern Physics **79**(4): 1217.

Hashimoto, A., K. Suenaga, et al. (2004). "Direct evidence for atomic defects in graphene layers." Nature **430**(7002): 870-873.

Hertel, T., R. E. Walkup, et al. (1998). "Deformation of carbon nanotubes by surface van der Waals forces." Physical Review B **58**(20): 13870-13873.

Hrusak, J., D. K. Bohme, et al. (1992). "Ab initio MO calculation on the energy barrier for the penetration of a benzene ring by a helium atom. Model studies for the formation of endohedral He@C60+[square root] complexes by high-

energy bimolecular reactions." Chemical Physics Letters **193**(1-3): 97-100.

Huang, Y., J. Wu, et al. (2006). "Thickness of graphene and single-wall carbon nanotubes." Physical Review B (Condensed Matter and Materials Physics) **74**(24): 245413-9.

Ilic, B., H. G. Craighead, et al. (2004). "Attogram detection using nanoelectromechanical oscillators." Journal of Applied Physics **95**(7): 3694-3703.

Ilic, B., S. Krylov, et al. (2005). "Optical excitation of nanoelectromechanical oscillators." Applied Physics Letters **86**(19): 193114.

Ishigami, M., J. H. Chen, et al. (2007). "Atomic Structure of Graphene on SiO2." Nano Lett. **7**(6): 1643-1648.

Jay, S. M., A. Z. Christian, et al. (2003). "Examination of Bulge Test for Determining Residual Stress, Young's Modulus, and Poisson's Ratio of 3C-SiC Thin Films." Journal of Aerospace Engineering **16**(2): 46-54.

Jiang, C., S. Markutsya, et al. (2004). "Freely suspended nanocomposite membranes as highly sensitive sensors." Nat Mater **3**(10): 721-728.

Karabacak, D. M. (2008). Resonant Operation of Nanoelectromechanial Systems in Fluidic Environments. Mechanical Engineering. Boston, MA, Boston University**:** 170.

Kelly, B. T. (1981). Physics of graphite. London; Englewood, N.J., Applied Science.

Kenny, T. (2001). "Nanometer-scale force sensing with MEMS devices." Sensors Journal, IEEE **1**(2): 148-157.

Klitzing, K. v., G. Dorda, et al. (1980). "New Method for High-Accuracy Determination of the Fine-Structure Constant Based on Quantized Hall Resistance." Physical Review Letters **45**(6): 494.

Knobel, R. G. and A. N. Cleland (2003). "Nanometre-scale displacement sensing

using a single electron transistor." Nature **424**(6946): 291-293.

Kouwenhoven, L. P., C. M. Marcus, et al. (1997). Electron transport in quantum dots. Mesoscopic Electron Transport. L. L. Sohn, L. P. Kouwenhoven and G. Schoen. New York and London, Plenum**:** 105-214.

Kozinsky, I., H. W. C. Postma, et al. (2006). "Tuning nonlinearity, dynamic range, and frequency of nanomechanical resonators." Applied Physics Letters **88**(25): 253101.

LaHaye, M. D., O. Buu, et al. (2004). "Approaching the quantum limit of a nanomechanical resonator." Science **304**: 74-77.

Lavrik, N. V. and P. G. Datskos (2003). "Femtogram mass detection using photothermally actuated nanomechanical resonators." Applied Physics Letters **82**(16): 2697-2699.

Li, X., X. Wang, et al. (2008). "Chemically Derived, Ultrasmooth Graphene Nanoribbon Semiconductors." Science **319**(5867): 1229-1232.

Li, X. X., T. Ono, et al. (2003). "Ultrathin single-crystalline-silicon cantilever resonators: Fabrication technology and significant specimen size effect on Young's modulus." Applied Physics Letters **83**(15): 3081-3083.

Liang, W. J., M. P. Shores, et al. (2002). "Kondo resonance in a single-molecule transistor." Nature **417**(6890): 725-729.

Liang, X., Z. Fu, et al. (2007). "Graphene Transistors Fabricated via Transfer-Printing In Device Active-Areas on Large Wafer." Nano Lett. **7**(12): 3840-3844.

Meyer, J. C., A. K. Geim, et al. (2007). "The structure of suspended graphene sheets." Nature **446**(7131): 60-63.

Mueggenburg, K. E., X.-M. Lin, et al. (2007). "Elastic membranes of close-packed nanoparticle arrays." Nat Mater **6**(9): 656-660.

Murry, R. L. and G. E. Scuseria (1994). "Theoretical Evidence for a C60 "Window"

Mechanism." Science **263**(5148): 791-793.

Nix, W. D. (2005). "Lecture Notes for "Mechanical Properties of Thin Films"."

Novoselov, K. S., A. K. Geim, et al. (2005). "Two-dimensional gas of massless Dirac fermions in graphene." Nature **438**(7065): 197-200.

Novoselov, K. S., A. K. Geim, et al. (2004). "Electric Field Effect in Atomically Thin Carbon Films." Science **306**(5696): 666-669.

Novoselov, K. S., D. Jiang, et al. (2005). "Two-dimensional atomic crystals." Proceedings of the National Academy of Sciences of the United States of America **102**(30): 10451-10453.

Park, J. W., A. N. Pasupathy, et al. (2003). "Wiring up single molecules." Thin Solid Films **438**: 457-461.

Perkins, W. G. and D. R. Begeal (1971). "Diffusion and Permeation of He, Ne, Ar, Kr, and D[sub 2] through Silicon Oxide Thin Films." The Journal of Chemical Physics **54**(4): 1683-1694.

Pertsin, A. and M. Grunze (2006). "Water as a lubricant for graphite: A computer simulation study." The Journal of Chemical Physics **125**(11): 114707.

Petersen, K. E. (1982). "Silicon as a mechanical material

" Proceedings of the IEEE **70**(5): 420-457.

Ponomarenko, L. A., F. Schedin, et al. (2008). "Chaotic Dirac Billiard in Graphene Quantum Dots." Science **320**(5874): 356-358.

Poot, M. and H. S. J. van der Zant (2008). "Nanomechanical properties of few-layer graphene membranes." Applied Physics Letters **92**(6).

Qian, D., G. J. Wagner, et al. (2002). "Mechanics of carbon nanotubes." Applied Mechanics Reviews **55**(6): 495-533.

Ralph, D. C., C. T. Black, et al. (1997). "Gate-voltage studies of discrete electronic states in aluminum nanoparticles." Physical Review Letters **78**(21): 4087-4090.

Reif, F. (1965). Fundamentals of Statistical and Thermal Physics. New York, NY, McGraw-Hill Book Company.

Rose, F., A. Debray, et al. (2006). "Suspended HOPG nanosheets for HOPG nanoresonator engineering and new carbon nanostructure synthesis." Nanotechnology(20): 5192.

Ruoff, R. S., J. Tersoff, et al. (1993). "Radial deformation of carbon nanotubes by van der Waals forces." Nature **364**(6437): 514-516.

Rutter, G. M., J. N. Crain, et al. (2007). "Scattering and Interference in Epitaxial Graphene." Science **317**(5835): 219-222.

Saito, R., G. Dresselhaus, et al. (1998). Physical Properties of Carbon Nanotubes. London, England, Imperial College Press.

Saunders, M., H. A. Jimenez-Vazquez, et al. (1993). "Stable Compounds of Helium and Neon: He@C60 and Ne@C60." Science **259**(5100): 1428-1430.

Savage, R. H. (1948). "Graphite Lubrication." Journal of Applied Physics **19**(1): 1-10.

Sazonova, V. (2006). A Tunable Carbon Nanotube Resonator. Physics. Ithaca, Cornell University**:** 209.

Sazonova, V., Y. Yaish, et al. (2004). "A tunable carbon nanotube electromechanical oscillator." Nature **431**(7006): 284-287.

Schoelkopf, R. J., P. Wahlgren, et al. (1998). "The Radio-Frequency Single-Electron Transistor (RF-SET): A Fast and Ultrasensitive Electrometer." Science **280**(5367): 1238-1242.

Sekaric, L., J. M. Parpia, et al. (2002). "Nanomechanical resonant structures in nanocrystalline diamond." Applied Physics Letters **81**(23): 4455-4457.

Senturia, S. D. (2001). Microsystem Design. New York, NY, Springer Science+Business Media, LLC.

Shagam, M. Y. (2006). Nanomechanical Displacement Detection Using Fiber Optic

Interferometry. Mechanical Engineering. Boston, Boston University**:** 95.

Sidorov, A. N., M. M. Yazdanpanah, et al. (2007). "Electrostatic deposition of graphene." Nanotechnology(13): 135301.

Singh, J. (1993). Physics of Semiconductors and their Heterostructures. New York, NY., McGraw-Hill.

Soule, D. E. (1958). "Magnetic Field Dependence of the Hall Effect and Magnetoresistance in Graphite Single Crystals." Physical Review **112**(3): 698-707.

Staff (2008). Yole Ranks Top 30 MEMS Suppliers; Sees Rapid Growth in Consumer, Medical. Semiconductor International.

Stolyarova, E., K. T. Rim, et al. (2007). "High-resolution scanning tunneling microscopy imaging of mesoscopic graphene sheets on an insulating surface." Proceedings of the National Academy of Sciences **104**(22): 9209-9212.

Stormer, H. L. (1999). "Nobel Lecture: The fractional quantum Hall effect." Reviews of Modern Physics **71**(4): 875.

Striemer, C. C., T. R. Gaborski, et al. (2007). "Charge- and size-based separation of macromolecules using ultrathin silicon membranes." Nature **445**(7129): 749-753.

Tanizawa, K. and K. Yamamoto (2004). "Measuring Apparatus of Membrane Tension and Its Characteristics." National Committee for Theoretical and Applied Mechanics, Science Council of Japan **53**: 75-82.

Tans, S. J., M. H. Devoret, et al. (1997). "Individual single-wall carbon nanotubes as quantum wires." Nature **386**(6624): 474-477.

Timoshenko, S. (1934). Theory of Elasticity. New York, McGraw-Hill Book Company, Inc.

Timoshenko, S., D. H. Young, et al. (1974). Vibration Problems in Engineering. New

York, John Wiley and Sons, Inc.

Tokumoto, T., E. Jobiliong, et al. (2004). "Electric and thermoelectric transport probes of metal-insulator and two-band magnetotransport behavior in graphite." Solid State Communications **129**(9): 599-604.

Verbridge, S. S., J. M. Parpia, et al. (2006). "High quality factor resonance at room temperature with nanostrings under high tensile stress." Journal of Applied Physics **99**(12): 124304.

Vlassak, J. J. and W. D. Nix (1992). "A new bulge test technique for the determination of Young's modulus and Poisson's ratio." Journal of Materials Research **7**(12): 3242-3249.

Wallace, P. R. (1947). "The Band Theory of Graphite." Physical Review **71**(9): 622-634.

Whittaker, J. D., E. D. Minot, et al. (2006). "Measurement of the Adhesion Force between Carbon Nanotubes and a Silicon Dioxide Substrate." Nano Lett. **6**(5): 953-957.

Wilson, M. (2006). "Electrons in atomically thin carbon sheets behave like massless particles." Physics Today **59**(1): 21-23.

Yakobson, B. I., C. J. Brabec, et al. (1996). "Nanomechanics of carbon tubes: Instabilities beyond linear response." Physical Review Letters **76**(14): 2511-2514.

Yasumura, K. Y., T. D. Stowe, et al. (2000). "Quality factors in micron- and submicron-thick cantilevers." Microelectromechanical Systems, Journal of **9**(1): 117-125.

Zhang, Y., J. Small, P. , et al. (2005). "Fabrication and electric-field-dependent transport measurements of mesoscopic graphite devices." Applied Physics Letters **86**(7): 073104.

Zhang, Y. B., Y. W. Tan, et al. (2005). "Experimental observation of the quantum Hall effect and Berry's phase in graphene." Nature **438**(7065): 201-204.

Zheng, Q., B. Jiang, et al. (2008). "Self-Retracting Motion of Graphite Microflakes." Physical Review Letters **100**(6): 067205.